MORPHO-SEDIMENTARY DYNAMICS OF A MEGATIDAL, MIXED SAND-GRAVEL BEACH

by

Tristan Guest

Submitted in partial fulfillment of the requirements
for the degree of Doctor of Philosophy

at

Dalhousie University
Halifax, Nova Scotia
April 2020

to the dog who is wagged by her tail

TABLE OF CONTENTS

LIST OF TABLES

LIST OF FIGURES

ABSTRACT

Sediment dynamics on mixed sand-gravel (MSG) beaches have received much less attention in the literature than on sandy beaches. The steep slopes characteristic of MSG beaches result in an energetic shorebreak, accompanied by ballistic transport of gravel- and cobble-sized grains. The associated risks of damage to *in situ* instrumentation have contributed to the relative scarcity of observational data. A central goal of this thesis is to contribute new knowledge and understanding of morphodynamic responses to wave forcing on MSG beaches through the use of innovative, inexpensive sensing systems not exposed to the rigours of the shorebreak. The studies were carried out at Advocate Beach, Nova Scotia, a 1:10 slope megatidal MSG beach at the head of the Bay of Fundy. The principal results are presented in four chapters. First, the vertical structure of surface gravity wave-induced pore pressure in the intertidal zone is investigated using a coherent array of buried pressure sensors. A key finding is that the phase of the pore pressure lags the pressure at the sediment surface. This phase lag is shown to be due to the presence of bubbles within the sediment column, which has implications for using buried pressure sensors for surface gravity wave measurement in the intertidal zone on MSG beaches. Second, video observations are used to characterise beach cusp morphodynamics at high temporal resolution. The timescale of cusp evolution is shown to be $O(10)$ minutes. Importantly, the cusps exhibit pronounced bay/horn size segregation, indicating strong feedback between the hydrodynamics and cusp formation on MSG beaches. In the third main chapter, correlations between bed level and the surficial mean grain size are investigated using GPS and photographic surveys of the intertidal beach. Finally, the coevolution of bed level and grain size is investigated in the swash zone using an array of collocated acoustic range sensors and cameras, and Lagrangian tracking of painted cobbles is utilised to study grain size segregation at the swash scale. The results are discussed in the context of a morpho-sedimentary dynamics framework, emphasising the intrinsic interrelationships between morphology, flow, and the broad surficial grain size distribution.

List of Abbreviations and Symbols Used

Abbreviation	Description
CT	cross-shore survey transect
DG	densely sampled survey grid
DGS	digital grain size/sizing
FOV	field of view
HWL	high water line
LT1	longshore survey transect 1
LT2	longshore survey transect 2
MHW	mean high water
MSD	morpho-sedimentary dynamics
MSG	mixed sand-gravel
NTP	Network Time Protocol
PT	pressure transducer
PTP	Precision Time Protocol
RMS	root mean square
RMSE	root mean square error
RTK GPS	real time kinematic global positioning system
SIGMA	variance-type time exposure image
TIMEX	time exposure (image)
UTC	Coordinated Universal Time
YD	yearday

Notation	Description
$O(\cdot)$	order of magnitude
$\overline{(\cdot)}$	spatial mean
$\langle\cdot\rangle$	temporal mean
$\cdot'$	observation associated with previous time step (Ch. 6 only)

Roman symbol	Description	Units
A_y	cross-shore beach cusp amplitude	m
D	sediment grain diameter	mm
D_{50}	median sediment grain diameter	mm
f	frequency	Hz
g	gravitational acceleration	m s^{-2}
G	shear modulus	Pa
h	water depth	m
H_0	deep water wave height	m
H_s	significant wave height	m
i, j	longshore, cross-shore coordinate indices	-
$\tilde{k}$	radian wavenumber	m^{-1}
$\tilde{k}'$	*Yamamoto et al.* (1978) vertical wavenumber	m^{-1}
$\tilde{k}''$	*Yamamoto et al.* (1978) vertical wavenumber	m^{-1}
k_c	hydraulic conductivity	m s^{-1}
L_0	deep water wave length	m
m	*Yamamoto et al.* (1978) weighting parameter	-
n	porosity	-
p	oscillatory component of pore water pressure	Pa
p_0	oscillatory component of water pressure at bed surface	Pa
P	absolute pore water pressure	Pa
P_a	atmospheric pressure	Pa
r	Pearson correlation coefficient	-
$\hat{r}$	temporal correlation coefficient	-
R^2	wave reflection parameter	-
S	saturation (fractional pore water volume)	-
S_{pp}	pressure spectral density	Pa^2 Hz^{-1}
T_p	peak wave period	s
x, y, z	Eulerian coordinates	m
X, Y	observed properties	-

Greek symbol	Description	Units
α	statistical significance level	-
β	bulk compressibility of water	Pa
β'	effective compressibility of fluid (water-air)	Pa
β_a	bulk compressibility of air	Pa
β_s	beach slope	$^\circ$
γ	unit weight of pore fluid	kg m^{-2} s^{-2}
λ_c	beach cusp wavelength (longshore scale)	m
ν	Poisson's ratio	-
ω	radian frequency	s^{-1}
ω'	*Yamamoto et al.* (1978) intermediate parameter	-
ω''	*Yamamoto et al.* (1978) intermediate parameter	-
ρ	density of water	kg m^{-3}
σ_p	standard deviation of pressure-derived sea-surf. height	m
θ	phase lag of oscillatory component of pore-pressure	$^\circ$

ACKNOWLEDGEMENTS

I am very grateful to have been able to spend these past years considering interesting science questions, and to have been exposed to such wonderful and powerful techniques and tools for approaching them. I am a more enthusiastic and effective problem solver than when I began, and that alone makes the experience worthwhile.

There are many people who helped make my run at academia possible and enjoyable. First and foremost, I acknowledge my graduate supervisor, Alex Hay, who took me in as a wayward math major, put a shovel in my hands, and sent me off to dig the first of many holes in Advocate Beach. I have great admiration for Alex's commitment to quality science, and to exactness in meaning through language. Alex, you have spared the world another 'woolly' writer (to whatever extent I have absorbed your lessons, at least).

I acknowledge my advisory committee: David Barclay, Tony Bowen, and Mike Dowd. I hold the three of them in very high regard, and I am thankful for their productive and encouraging guidance. Insightful comments from Tony Bowen led to improvements in the thesis, as well as to shifts in my perspectives of field oceanography, models, and processes at the shoreline.

Thanks to Richard Cheel for helping me cut my teeth both at the Matlab prompt and at the soldering station. His mentorship – particularly in the early days of my graduate studies – was invaluable, as was his assistance in carrying out the field work described in this thesis. The benefits of Richard's presence when one needs to retrieve something heavy from the seafloor cannot be overstated. Thanks, also, to the rest of the Hay Lab, past and present, for support, discussions, feedback, and friendship. Jenna Hare in particular has my thanks for always being willing to chat, and for her contributions to the camaraderie shared by the students of our department. I am sure that I am not alone in thinking this.

Thanks to the oceanography skate crew: Kevin, Matt, Ian, and (honorary member) Riley for many nourishing lunchtime sessions. Those sunny days at the bowl stand out as a true highlight of my graduate student experience.

Of course, I am grateful to my family and friends for their support and inspiration, which came in many forms: from my grandmother, Patricia, who brightened my Tuesdays with our phone calls, and who made sure I was eating enough through frequent lunches and

snack deliveries; from my parents, who have been genuinely interested since the beginning, and who helped in absolutely any way they could fathom; from my brother, by being a model of commitment to the things that one loves; and from the rest of the gang for shared meals, post-work ales, river runs, bike rides, and other shenanigans of all kinds.

My partner Laura has been a pillar of support in the daily grind of the past five years. She has witnessed the ebb and flow of my enthusiasm, and listened with patience and understanding as I summarised each snag, conundrum, solution, and bit of excitement that the days presented. It has been truly helpful. Thank you, Laura.

Finally, thanks to E. N. Lorenz for giving language and direction to a field of mathematics that inspired me long ago to pursue study in the mathematical and physical sciences, and whose work I have been led back to at many intervals in the course of my education. Perhaps I would be somewhere else were it not for the flick of his pen sixty years ago.

CHAPTER 1

INTRODUCTION

1.1 Morpho-Sedimentary Dynamics

Beaches are dynamic and morphologically diverse regions of the coastal zone. In the process of energy dissipation at a shoreline, the mechanical energy associated with wave- and tide-induced currents is transformed into heat through turbulent dissipation, for example, following wave breaking, or transferred to the bed facilitating sediment transport. The resulting system is highly nonlinear, and like many damped, forced systems exhibits complex dynamics. Complexity in this sense may be *deterministic* (e.g., *Lorenz*, 1963), wherein nonlinear interactions between system elements are represented by relatively simple systems of deterministic equations, but with sensitive dependence on initial conditions leading to complex outcomes, or *stochastic*, wherein complexity arises through the cumulative impacts of numerous process-response mechanisms, or through multiple controls on process-response relationships operating over ranges of spatial and temporal scales (*Phillips*, 1992). Many, or perhaps even most, geomorphic systems and landforms are forced and dissipative by nature, giving rise to complex dynamics and signatures of self-organising behaviour. Beaches are no exception: external forcing (e.g., wave- or tide-induced currents) elicits responses from fundamental system elements (e.g., grains of sand), which further influence the system state through internal dynamics and feedbacks (e.g., critical thresholds such as angles of repose), with outcomes ranging from the emergence of patterned bed states with striking regularity, as in the case of beach cusps (e.g., *Werner and Fink*, 1993; *Coco et al.*, 2000), to the characteristic shape of a beach as a whole (i.e., its profile: *Dean*, 1991; *Turner*, 1995).

Positive and negative feedbacks arise through asymmetries between the characteristic

response times of morphology and hydrodynamics: change is induced though spatial and temporal variability in the hydrodynamics, which give spatial and temporal structure to erosion and deposition processes through gradients in sediment transport. Changes in the morphology, which occur over longer timescales, feedback on the flow by altering velocity, and therefore transport, gradients, in processes that may be constructive (positive feedbacks, self-organisation) or destructive (negative feedbacks, self-regulation). This process of morphological adjustment through mutual associations between form and flow, facilitated by sediment transport, is the essence of the morphodynamic model from *Wright and Thom* (1977), which emphasises the intrinsic interdependence of fluid dynamic and morphodynamic processes, such that cause and effect are not readily apparent.

The vast majority of beach research has been concerned with the morphodynamics of beaches composed of sand. On beaches where grain sizes are large, or where a broad range of grain sizes exists, texturing of the bed and changes in the hydraulic properties exert an added control on the hydrodynamics through increased roughness effects at the bed-fluid interface and changes in the vertical flow properties through the bed as a porous medium. The inclusion of textural feedbacks in the morphological evolution of the beach through flow-morphology interactions renders a morphodynamic model incapable of completely describing the system's dynamics. In their gravel beach review paper, *Buscombe and Masselink* (2006) acknowledged this shortcoming, and urged the adopting of a 'morpho-sedimentary dynamics' framework for the future study of coarse-grained beaches. *Buscombe and Masselink* (see also *Carter and Orford*, 1993) define morpho-sedimentary dynamics (MSD) as: "the mutual association and feedbacks in operation between flows (hydrodynamics and hydraulics), and forms (morphological architectures and textural mosaics), mediated through selective sediment transport mechanisms acting upon the mechanical, hydrodynamic and hydraulic properties of sediments."

Linkages between morphology and the grain size distribution have been noted in the literature for beaches of all types, most notably characterising features like high tide berms and beach cusps, where topographic highs typically correspond to coarser sediments, as well as the beach step – a discontinuity in beach slope that corresponds to the region of bore collapse at the seaward edge of the swash zone – which is generally observed to be composed of coarser material. The association between morphology and grain size can be particularly striking on mixed sand-gravel (MSG) beaches, where sedimentary structures

which are well-organised in terms of grain size are often observed in addition to, or in conjunction with, morphological structures. *Buscombe and Masselink* (2006) noted that textural patterning on coarse or mixed-grained beaches may serve, through their effects on the flow velocity gradients near the bed, as surrogates to the morphological bedforms of sand beaches, in other words, that the two types of feature are to some extent 'hydraulically equivalent'.

Gravel beaches are a common feature of the world's coastlines, particularly in the mid- to high-latitudes where active terrestrial weathering or glaciation in the recent geologic past have provided ample source material. MSG beaches form a subset of gravel beaches (see *Jennings and Shulmeister*, 2002) which have recently received increased attention in the literature. The hydraulically rough and permeable nature of coarse sediments provides an efficient mechanism for wave energy dissipation at the shoreline, thus providing a natural and sustainable form of coastal defence (*Van Wellen et al.*, 2000; *Almeida et al.*, 2014). In the face of rising sea levels, the increasing demand for coastal stabilisation and erosion prevention has led to the use of gravel and sand-gravel mixtures as soft-engineering solutions, through replenishing vulnerable or eroding coastlines with imported material. MSG beaches in particular have seen a considerable increase in interest, since the imported material used in replenishment schemes increasingly consists of mixed-sized sediments dredged from offshore (*Mason and Coates*, 2001). However, sediment transport processes on MSG beaches are not well studied in comparison to sandy beaches, and the need for further research to support engineering designs, re-nourishment projects, and modelling efforts, is stressed in the current literature.

On mixed-sediment beaches, the additional degrees of freedom associated with spatial and temporal grain size heterogeneity, and the propensity for mixed sediments to self organise into assemblages of like-sized grains, make characterising the response of the bed to forcing more difficult; in addition to the space- and time-varying influences of hydrodynamics and morphological feedbacks, the characteristics of grain mobilisation and deposition are also influenced by the 'background' grain size distribution. For example, the likelihood of a coarse particle being deposited is decreased where the background material is relatively fine (the ease of rolling the particle causing it to be 'rejected' by the substrate) and increased where a like-sized substrate 'accepts' the particle due to grain interlocking. Similarly, larger particles serve as roughness elements, more susceptible to lift and drag

forces, but capable of 'sheltering' neighbouring grains (*Buscombe and Masselink*, 2006). Processes of self-organisation leading to spatial and temporal heterogeneity of the grain size distribution also have implications for the hydraulic properties of the sediment (e.g., *Horn*, 2006). The relative influence of the percolation of water through the beach surface on sediment transport, particularly in the swash zone, must also be assumed to vary in time and space.

The interactions between sediment size-fractions during transport are nontrivial, and along with hydraulic effects, impose a significant challenge for the prediction of MSG beach sediment transport. A sound observational basis is required in order to parameterise the dynamics in a predictive framework, including a phenomenological understanding of the influence of variations in the grain-size distribution on transport and morphology. Acknowledging the shortcomings of state-of-the-art sediment-water flow descriptions, *Buscombe and Masselink* (2006) note: "A sensible and pragmatic approach would be to first document field observations and phenomena, then work 'backwards' into the underlying physics."

The paucity of measurements of hydrodynamics and sediment transport on MSG beaches is due in large part to difficulties in obtaining observations *in situ*. The steeper slopes characteristic of gravel and mixed beaches lead to narrow, energetic shore breaks capable of entraining gravel- and cobble-sized grains. The utility of sensors commonly employed in sandy beach settings is therefore limited. Remote observation methods making use of, e.g., video (*Holman and Stanley*, 2007), aero-acoustic sensing (*Turner et al.*, 2008), terrestrial lidar (*van Gaalen et al.*, 2011), and digital imagery (*Buscombe*, 2013), as well as instrument burial (e.g., *Raubenheimer et al.*, 1998; *Michallet et al.*, 2009) provide alternatives. Also rare in the literature are observations of grain size dynamics sufficient to undertake meaningful investigations of morpho-sedimentary processes in the swash zone. Until recently, such observations were not obtainable in a non-intrusive manner. The increasing usage of digital grain sizing methods which are capable of producing estimates of grain size distributions from optical imagery is promising for the study of morpho-sedimentary dynamics.

In this thesis, field data are emphasised, with observations of hydro/morphodynamics, grain size, and sediment dynamics from the intertidal zone of a mixed sand-gravel beach. The study site is Advocate Beach: a steep mixed sand-gravel beach with a tide range often

in excess of 10 m. The swash zone is a notoriously difficult region to obtain observations due to the presence of often energetic, aerated flows. The presence of a large tide range has several benefits in this regard: (1) the intertidal zone can be accessed each low tide to install, retrieve, or service *in situ* instrumentation; (2) the force applied per unit area of the beach surface is reduced; and similarly, (3) the time resolution of observations, e.g., before and after, with regard to the passage of the swash zone, can be improved. In effect, these benefits result in an improved signal to noise ratio, since morpho-sedimentary signatures are spread over a large intertidal beach face, allowing a finer-scale look at transport processes in space and time. Though the presence of a large tide range, coupled with generally well-mixed beach sediment composition and fetch-limited forcing, is not representative of MSG beaches in general, the benefits of an improved signal to noise ratio on understanding small-scale transport processes make Advocate Beach a worthwhile study site.

1.2 Research Objectives and Thesis Outline

The purpose of this thesis is to contribute knowledge and understanding of morpho-sedimentary, hydrodynamic, and hydraulic processes on mixed sand-gravel beaches over sub-tidal timescales, while exploring remote and *in situ* methods for obtaining field observations at energetic mixed sand-gravel beach sites. This is achieved with an emphasis on field observations, through a series of studies at Advocate Beach, Nova Scotia, Canada. The objectives, with associated questions, are as follows:

1. Characterise the depth dependence of the phase lag and attenuation of oscillatory pore water pressures induced by surface gravity waves.
    - Can the pore-pressure amplitude and phase be predicted using a poro-elastic bed response model?
    - Is the use of pressure sensors buried in the intertidal beach a viable means of accurately inferring surface wave height and phase in the surf and swash zones, where deploying *in situ* instrumentation is otherwise logistically challenging?
2. Investigate the morpho- and hydrodynamic processes associated with mixed sand-gravel beach cusp evolution.

- How do mixed sand-gravel cusps fit into the existing cusp literature?
- What characterises the timescale of cusp evolution at Advocate Beach?
- What effect does large tidal range have on the timing of cusp events?
- What is the role of the beach surface grain size distribution in cusp morphological evolution?

3. Investigate grain size dynamics and linkages to swash zone morphologic change.

    - Are there observable signatures of correlation between bed level change and the grain size distribution?
    - Can Lagrangian tracking of gravel and cobble size-fractions help us characterise sorting processes in the swash zone?

The remainder of the thesis is organised as follows. In Chapter 2, some relevant background information is provided, including a general description of mixed sand-gravel beaches and their defining characteristics; a brief review of the beach cusp literature and theories for their formation; and an overview of the factors contributing to mixed sand-gravel sediment transport. A description of the study site is presented in Chapter 3, including summaries of two field campaigns, conducted in October-November of 2015 and October of 2018. The presentation of morpho-sedimentary and hydrodynamical data collected during the Advocate Beach field campaigns is presented in Chapters 4 through 7. In Chapter 4, pressure data are used to assess the viability of using buried pressure sensors to accurately infer surface wave height and phase in the surf and swash zones, where deploying *in situ* instrumentation is otherwise logistically challenging. Chapter 5 presents video-based observations of beach cusp dynamics. Chapters 6 and 7 present coincident observations of bed level and mean grain size at the beach surface: at the scale of the intertidal zone, using GPS and image-based survey data (Chapter 6), and in the swash zone, using acoustic bed level sensors and digital imagery (Chapter 7). In Chapter 8, the key findings of the thesis are summarised, followed by some implications of the findings and a future work outlook.

Chapters 4 and 5 have been published as peer-reviewed articles (*Guest and Hay*, 2017, 2019) in the *Journal of Geophysical Reseach: Oceans* and *Marine Geology*, respectively. The text and figures of each chapter have not been altered from the published versions,

except where necessary for reference or navigation within the thesis. As lead author of the articles, I was responsible for the development and implementation of the analysis methods and the interpretation of the results. I also developed the figures, and wrote the corresponding manuscripts. Alex Hay, co-author of both articles, provided guidance in the research, and contributed to the editing of the manuscripts. I shared responsibility with Alex Hay and Richard Cheel (lab technician) for the experimental design.

Chapters 6 and 7 represent manuscripts in preparation for publication. As such, they emulate the article format of the previous two chapters, i.e., in layout and relative self-containment.

CHAPTER 2

BACKGROUND

In this section, a brief description of mixed sand-gravel (MSG) beaches is given, along with an outline of the recent MSG beach literature. Next, a review of the beach cusp literature is presented, with particular emphasis on mechanisms, timescales, and the role of grain-size segregation. Finally, leading order factors influencing sediment transport on MSG beaches are described.

2.1 Mixed Sand-Gravel Beaches

Gravel beaches can be separated into three distinct morpho-sedimentary types, as outlined in the field-based classification scheme by *Jennings and Shulmeister* (2002): (1) pure gravel; (2) composite gravel, characterised by a steep gravel berm fronted by a sandy low-angle intertidal terrace; and (3) mixed sand-gravel, having moderate to steep slopes and well-mixed sediments both across-shore and vertically within the sediment column. Mixed sand-gravel beaches are common in the mid- to high-latitudes, where past glaciation or significant terrestrial weathering has provided an abundant source of coarse sediment. Typical grain sizes on MSG beaches vary from coarse sand to cobbles (*Mason and Coates*, 2001).

Mixed sand-gravel beaches have features in common with both pure sand and gravel beaches: Like sand beaches, they are characterised by lower hydraulic conductivities – i.e., the rate at which water can pass through the pore spaces of the medium, having units of distance per unit time – than pure gravel. Similar to gravel beaches, MSG beaches are generally steep-sloped, and therefore are typically characterised by narrow surf zones leading to energetic shore breaks and morphodynamics dominated by processes

in the swash zone – the region of the beach intermittently covered and exposed by water following wave breaking. Despite any similarities, MSG beaches have been noted to be morphologically distinct from, and more complex than, both pure sand and gravel beaches (*Kirk*, 1980). In particular, the grain size dynamics of MSG beaches in response to variations in forcing are not well understood, and have in some cases been observed to be in fundamental opposition to the responses expected on sand beaches, as in the case of the fining of beach surficial sediments in response to energetic waves, observed by *Nordstrom and Jackson* (1993), *Pontee et al.* (2004), *Curtiss et al.* (2009), *Miller et al.* (2011), and *Hay et al.* (2014).

Much of our conceptual understanding of MSG beach morphology is derived from investigations of MSG beaches in New Zealand in the 1970s and 80s (e.g., *McLean*, 1970; *Kirk*, 1975, 1980; *Matthews*, 1983). Some illuminating field and laboratory experiments were also carried out by *Longuet-Higgins and Parkin* (1962), treating the role of spatial and temporal hydraulic gradients (i.e., percolation) related to grain size segregation in the context of MSG beach cusp formation.

In the past 20 years, MSG beaches have seen an increase in research interest due in large part to the increasing use of sand-gravel mixtures in beach replenishment schemes (*Mason and Coates*, 2001). MSG beaches have also been acknowledged to be of interest in a purely scientific sense due to their complex dynamics, their generally well-mixed nature making them well-suited to investigations of sediment size segregation and pattern formation (*Hay et al.*, 2014). The majority of recent field studies have been concerned with MSG beach sediment and morphodynamics. Many of these studies have investigated sediment dynamics using Lagrangian tracers, through radio frequency identification (RFID) tagging (*Osborne*, 2005; *Allan et al.*, 2006; *Curtiss et al.*, 2009; *Dickson et al.*, 2011; *Miller et al.*, 2011; *Miller and Warrick*, 2012; *Bertoni et al.*, 2012; *Grottoli et al.*, 2015, 2019) or fluorescent painting of coarse natural sediments (*Ciavola and Castiglione*, 2009; *Stark and Hay*, 2016). These studies span a wide range of transport dynamics, e.g., with regard to magnitudes of longshore versus cross-shore transport and response to energetic or fairweather wave forcing conditions. Site-dependent considerations, including the characteristics of the forcing climate, coastline orientation, profile shape, and sediment type (e.g., size, shape, composition) are also important sources of variation.

Studies of MSG beach morphodynamics have been undertaken by *Pontee et al.* (2004),

Horn and Walton (2004), *Ivamy and Kench* (2006), *Miller et al.* (2011), *Miller and Warrick* (2012), *Bramato et al.* (2012), *Roberts et al.* (2013), *Hay et al.* (2014), *Almeida et al.* (2014), and *Grottoli et al.* (2017). Of these, *Pontee et al.* (2004), *Miller et al.* (2011), *Miller and Warrick* (2012), *Roberts et al.* (2013) and *Hay et al.* (2014) also reported observations of grain size, though none of their sampling strategies were designed to evaluate collocated changes in bed level and grain size. With regard to the coevolution of morphology and the grain size distribution – observations of which are required in order to evaluate the importance of sedimentary feedbacks in beach morphological evolution – two studies have been undertaken (*Masselink et al.*, 2007; *Austin and Buscombe*, 2008), though both at pure gravel beach sites, with none treating MSG.

Only *Horn and Walton* (2004) and *Almeida et al.* (2014) reported observations of morphological processes in the swash zone at timescales commensurate with the wave forcing. *Horn and Walton* used a manual post-and-ruler method, sampling one-metre (cross-shore) spaced stations in the swash zone every 10-25 seconds over a three-hour period encompassing high tide. Their emphasis was on the magnitude of intra-swash timescale bed level oscillations, in comparison to magnitudes of bed level change over longer periods (i.e., hours). *Almeida et al.* used a terrestrial laser scanner which sampled the intertidal bed elevation at 2.5 Hz over the course of a tidal cycle characterised by energetic conditions. They noted a minimal morphological response to forcing in the intertidal zone in comparison to three other beaches surveyed (two pure gravel and one composite gravel), but did not emphasise morphological changes at wave timescales.

Leading order factors influencing sediment transport on MSG beaches are outlined in section 2.3. For a more complete overview of MSG beaches and their dynamics, refer to the review papers of *Kirk* (1980) and *Mason and Coates* (2001).

2.2 Beach Cusps

Beach cusps are spatially periodic sedimentary features common on beach foreshores. They consist of seaward-pointing sequences of ridges (horns), separated by topographic depressions (embayments), with quasi-regular spacings varying from $O(10^{-1})$ to $O(10^{2})$ m (*Coco et al.*, 1999). Cusps are generally acknowledged to be swash-generated features, though recent studies have drawn a distinction between beach cusps of short wavelength (< 20 m), and the longer-wavelength 'large beach cusps' which may be tied to surf- as well

as swash-zone morphodynamic processes due to their larger cross-shore extent (*Garnier et al.*, 2010). The generation of cusps by swash processes links them closely to shoreline position, cusps generally being formed near the high water line. Cusps have been observed to form under a wide range of conditions and beach types, though they are acknowledged to form most readily during low energy, shore-normal incident wave forcing on reflective, medium- to coarse-grained beaches (*Holland*, 1998).

The modern (*ca.* 1970s to present) cusp literature has been largely focused on understanding the mechanism(s) responsible for cusp formation and establishing predictive relationships between cusp spacing and hydrodynamics. Efforts to establish relationships between spacing and wave forcing were initially based on the concept of a hydrodynamic template, provided by standing low mode subharmonic or synchronous edge waves – alongshore-propagating waves trapped to the shoreline through a combination of reflection and refraction – whose spatial structure would become imprinted on the underlying sediment (*Guza and Inman*, 1975; *Guza and Bowen*, 1981; *Holman and Bowen*, 1982). Later models are based on free, self-organising behaviour characterised by asymmetric feedbacks between hydrodynamics and morphology (*Werner and Fink*, 1993; *Coco et al.*, 2000, 2004; *Sunamura*, 2004; *Dodd et al.*, 2008). Both mechanisms have been shown through laboratory and modelling studies to be capable of producing cusp-like patterns, and predict cusps of comparable wavelength. Criticisms of the edge wave model stem in part from a lack of observed edge wave presence during episodes of cusp formation (e.g., *Holland and Holman*, 1996; *Masselink et al.*, 1997). *Ciriano et al.* (2005) suggested that both mechanisms may play a role at different stages of cusp evolution, for example, spatially periodic perturbations being provided by standing edge waves, after which self-organising feedbacks become dominant. Many have noted that the difficulty in identifying the mechanism responsible for cusp formation arises as a result of the difficulty in verifying the presence of edge waves, which require multidimensional arrays of current meters or pressure sensors to observe (e.g., *Coco et al.*, 1999).

Though the self-organisation model, which predicts cusp spacing as a linear function of swash zone width, has been used to successfully predict cusp spacings in a range of settings, *Sunamura* (2004) noted that the linear model is not predictive; since both the cusp length scale and the swash zone width are dependent variables, the formula represents no causality. Based on this, *Sunamura* suggested a model to predict cusp spacing that depends

upon wave height, period, and grain size, which in turn influence the beach slope and the swash zone width. The model predicts cusp spacing with accuracy similar to that of the edge wave and swash zone width models, but is the only length scale-predicting model that incorporates grain size.

The focus on cusp initiation mechanisms and predictors of spacing has given way in the last decade to renewed emphasis on cusp morphology and characterisation of their dynamics (*Almar et al.*, 2008; *van Gaalen et al.*, 2011; *Vousdoukas*, 2012; *Poate et al.*, 2014), based largely on the acknowledgement that predicting cusp spacing alone is an inadequate predictor of process (e.g., *Coco et al.*, 1999; *Almar et al.*, 2008). However, uncertainties remain about the nature of beach cusp morphological evolution. These include: varied and, in some cases, inconsistent conclusions regarding factors influencing cusp evolution timescales; the importance and/or role of grain size sorting; and a lack of consensus on the roles of accretion and erosion.

There has been little emphasis on cusp formation timescale. This may be partly due to the difficulty inherent in establishing meaningful formation time metrics. The data indicate that beach cusp lengthscale and formation time are related. The observations by *Komar* (1973) of beach cusps on a sandy lake shore often provide a lower limiting case in the literature for both cusp spacing and formation time – as short as 11 cm and 10 mins, respectively, though cusp formation is generally reported to occur over tidal timescales (hours to days), with cusp spacings on the order of tens of metres.

The relationship between timescale and beach composition is largely uninvestigated. Numerical modelling by both *Coco et al.* (2000) and *Dodd et al.* (2008) indicated a relationship between a dimensional transport constant in their sediment flux parameterisations and the number of swash cycles required for cusp formation. Fewer cycles were required when the transport constant was increased. As noted by *Dodd et al.* (2008), it is possible to approximate this constant as a function of median grain diameter using the *Van Rijn* (1984) sediment transport equation. The implication is that cusps would form more rapidly on beaches with a larger mean grain size. *Dodd et al.* (2008) also concluded from their model results that beach permeability favours cusp development by enhancing the feedback mechanism (i.e., infiltration through the horns decreases the backwash volume, therefore decreasing offshore transport). For the case of mixed sand and gravel beaches, the gradation of fine and coarse material between bays and horns would be expected to further

enhance feedbacks by increasing the asymmetry between erosion/depositional processes in bays and horns. Indeed, *Longuet-Higgins and Parkin* (1962) concluded from field observations that cusps form most easily given a vertical stratification of material: coarse sediments sitting atop a well-mixed, "impermeable" layer are more readily mobilised due to the reduced fluid infiltration. The heaping of sediments atop the horns makes them more permeable than the thinner layer in the bays, and therefore less subject to erosion.

Despite their long history of study, previous studies of beach cusps have generally been limited to beach environments comprised of a single sediment type (i.e., sand or gravel), with little emphasis on beaches composed of mixed sand and gravel. *Nolan et al.* (1999) presented the only study of which the author is aware from the last 20 years treating mixed sand-gravel cusps specifically. As their focus was on cusp morphometry, the dynamics of the formation process were not investigated.

The role of size sorting in the process of cusp formation was investigated by *van Gaalen et al.* (2011) for the case of a sandy, microtidal beach on the Atlantic coast of Florida. Using regular morphological observations from a terrestrial laser scanner and discrete surficial sediment sampling, they found no significant correlation between grain size and position between horn and embayment. This led them to suggest that horn coarsening and embayment fining occurs after cusp development, making them inherently different from other sorted bed forms whose formation depends on differential transport characteristics for different grain sizes. However, the sediment size distribution at their site was narrow, with typical grain sizes ranging from 0.17 to 0.35 mm.

Results regarding the relative importance of accretion and erosion are varied. Instances of cusps formation have been reported for conditions dominated by sediment accretion, erosion, or a combination of both (e.g., *Antia*, 1987; *Masselink et al.*, 1997; *Almar et al.*, 2008). In addition to their conclusions regarding size-sorting, *van Gaalen et al.* (2011) demonstrated that the accretive/erosive properties of cusps observed on a sandy, microtidal beach were dependent upon the position of the cusps relative to larger-scale coastal morphology. The reader is referred to the *van Gaalen et al.* paper for a more complete review of past results treating cusp horn/bay sedimentation.

2.3 Factors Affecting Mixed Sediment Transport

Though there are dynamic similarities between MSG and gravel beaches – e.g., narrow surf zones, and emphasis on swash zone transport – their responses to forcing may be markedly different. In particular, MSG beaches have percolation properties influenced by their high sand content, which may greatly reduce the hydraulic conductivity of the beach sediments (*Carter and Orford*, 1984). Hydraulic conductivity, sometimes referred to as the coefficient of permeability, is a measure of the ease with which a fluid travels through a porous medium, and has units of length over time. *Mason and Coates* (2001) identify hydraulic conductivity as a leading order factor influencing mixed beach transport, along with infiltration and groundwater, wave reflection, and the threshold of sediment motion. Hydraulic conductivity acts as a primary control on beach profile via uprush/backwash asymmetry introduced by in/exfiltration effects (bed shear stresses are reduced during uprush through infiltration and/or frictional dissipation, leading to profile steepening), and influences the relative importance of groundwater dynamics. Groundwater dynamics have been widely demonstrated to play in important role in swash zone sediment transport, most notably via the influence on swash uprush-backwash asymmetry (e.g. *Longuet-Higgins and Parkin*, 1962; *Packwood*, 1983), but also by altering the boundary layer thickness and the vertical force associated with fluid flow into or out of the bed (see: seepage forces, *Nielsen*, 1992, p. 101). The dynamics of substrate and groundwater response to wave loading also have implications for bed stability and mobilisation via, for example, impulsive pressure forces associated with wave breaking (*Pedrozo-Acuña et al.*, 2008) or periodic, momentary liquefaction events (*Michallet et al.*, 2009).

Initiation of motion and transport of mixed sediments has been studied extensively in the context of fluvial transport (e.g., *Wilcock and McArdell*, 1997; *Wilcock et al.*, 2001; *Wilcock and Crowe*, 2003; *Buscombe and Conley*, 2012). However, most studies involve steady unidirectional flow over a mildly sloping bed. MSG transport in the swash zone is complicated by percolation effects, fluid acceleration, and turbulence (e.g., following bore collapse). The limited availability of field observations also poses a challenge, especially in shallow aerated flows, where accurate non-intrusive observations of sediment transport remain beyond the state-of-the-art (*Pedrozo-Acuña et al.*, 2007).

Incipient sediment motion is typically described in terms of a threshold fluid velocity above which particles are mobilised (e.g., the Shields parameter, *Nielsen*, 1992). The

typical dependence of threshold parameters on bulk properties of the sediment (e.g., median grain diameter, D_{50}) is problematic for cases of wider grain-size distributions or sediment bimodality. For mixed sediments, interactions between size-fractions complicate the interpretation of mobilisation thresholds: larger particles are heavier, thus more difficult to move, but also protrude into the flow, and are therefore subject to larger lift and drag forces. Smaller grains are more readily entrained, but may be sheltered by the larger grains. Similarly, the ability of the flow to roll a grain depends upon its size relative to the substrate, the angle of pivot required for mobilisation being larger when a grain is nestled among grains of similar or larger size. These properties lead to mobilisation thresholds for mixed sediments which are different from estimates made assuming a bed of uniform composition (*Wilcock and McArdell*, 1993). The use of 'hiding' functions, empirically-derived correction factors that adjust thresholds based on the sediment distribution, circumvent this problem to some extent, but do not account for changes in transport properties resulting from size sorting (e.g., armouring, sorted bedforms, cusps) or spatial and temporal sediment heterogeneity.

The hiding-sheltering and rollability effects described above are intrinsic to the processes of armouring and overpassing, which have been used to describe size-sorting phenomena (*Moss*, 1962). In the process of armouring, aggregations of large grains create a substrate that readily 'accepts' grains of similar size, leading to bed surface coarsening and preventing further transport of coarse grains locally, while finer grains infiltrate through pore spaces (kinetic sieving). This is in contrast to overpassing, during which the inertia and rollability of larger grains cause them to be 'rejected' by a finer substrate. Armouring has been investigated in the fluvial literature for cases of unidirectional flow (e.g., *Gomez*, 1983), as well as in the swash zone literature (e.g., *Isla*, 1993).

On macrotidal beaches, morphodynamics are influenced by the tidal state. The position of the shoreline and swash zone translate in the cross-shore in phase with changing water level, varying the relative influence of in/exfiltration, reflectivity, and surficial grain-size distribution on sediment transport. Interactions between tide and groundwater have been demonstrated to be capable of influencing beach profiles (e.g., *Turner*, 1995), and in the case of a nonplanar beach face, reflection coefficients may vary with tidal stage (*Davidson et al.*, 1994). In the case of changing mean grain diameter in the cross-shore, rates of frictional dissipation may be affected. It is common for gravel and mixed beaches to

exhibit coarsening of mean grain size shoreward (*Mason and Coates*, 2001).

The effects of spatial and temporal variation in hydraulic conductivity, differential and distribution-dependent mobilisation thresholds, and grain size sorting on MSG sediment transport are difficult to capture in a predictive framework, and highlight the importance of an empirically-based, phenomenological understanding of processes.

CHAPTER 3

ADVOCATE BEACH

The objectives of this thesis are addressed using data from two field experiments at Advocate Beach, Nova Scotia. This section begins with an overview of the study site. Though the relevant components of each experiment are described in each chapter, overviews of the 2015 and 2018 field experiments are also provided here for completeness and ease of reference. The relevant analysis methodologies are outlined in the individual chapters. Chapters 4 and 5 treat data collected during the 2015 field campaign, and Chapters 6 and 7 are associated with the 2018 campaign.

3.1 Site Description

Advocate Beach is a mixed sand-gravel barrier beach positioned near the head of the Bay of Fundy in Nova Scotia, Canada (Fig. 4.3, p. 31; Fig. 5.1, p. 60). Based on the 8-12 m tidal range, Advocate beach can be classed as megatidal rather than macrotidal (*Levoy et al.*, 2000). The beach separates the headlands of Cape Chignecto to the west and Cape D'Or to the southeast, and is 5 km long with a nearly linear shoreline. The beach face is steep (approximately 1 in 10 slope) and the sediments poorly sorted, ranging from medium sand to cobbles and boulders greater than 20 cm in diameter. From the lower beach face to beneath lowest low water, the sediment composition transitions to cobble and boulder-sized material. From the southwest, the beach is exposed to the full 500 km fetch of the Bay of Fundy and adjacent Gulf of Maine, but is otherwise more fetch-limited. At low tide, the beach is observed to be uniformly planar with crest to low water distance as much as 100 m in spring tides (see *Taylor et al.*, 1985; *Hay et al.*, 2014).

During and after fairweather forcing, an active high tide berm can commonly be observed

near the high water line. One or more relict berms may be present landward of the active berm, particularly during neap tides. The berm composition is generally of coarser material than that found in the intertidal zone, consisting of relatively well sorted gravel and cobbles. Following periods of energetic wave forcing, the beach appears free of distinct morphological features, and the beach surface sediments are predominantly sandy. Episodes of pattern formation and surficial sediment sorting often occur at Advocate Beach, commonly in the form of beach cusps on the upper beach face (e.g., Fig. 5.2, p. 62). The cusps generally appear as well-organised sediment structures near the high water line, often extending tens of metres seaward, forming cross-shore bands of loose gravel and cobbles separated by sandy embayments. The beach experiences changes in forcing conditions over tidal time scales, which is reflected by daily changes in surficial sediment composition and topography. Consequently, cusp episodes at Advocate Beach are generally limited to a single tide.

During storms, peak incident wave periods typically fall within the wind-wave band (T_p = 4-7 seconds), with longer period swell usually limited to the weaker wave forcing conditions between storms. The combination of a steep beach slope and typically short period, wind-generated incident waves result in a highly energetic shore break for offshore significant wave heights of *ca*. 0.5 m and larger (*Hay et al.*, 2014). Under average forcing conditions, the beach is best described as dissipative rather than reflective, which is uncommon for beaches of similar composition and profile type (e.g., *Wright et al.*, 1979). For example, the mean reflectivity computed for a two week period in October 2018 was $R^2 = 0.14$, where R^2 is an approximation of the ratio of seaward to shoreward propagating wave energy, computed as a Miche number (*Miche*, 1951), following the method of *Elgar et al.* (1994). Driftwood and other mobile flotsam are often present in the shorebreak, providing additional hazards to *in situ* instrumentation over and above the impacts from coarse-grained sediment projectiles propelled by the high water velocities in the shorebreak and surf.

For additional information on Advocate Beach, including its history and more detailed descriptions of hydrodynamic processes, see *Taylor et al.* (1985), *Wilson et al.* (2014), and *Hay et al.* (2014).

3.2 2015 Field Experiment

The 2015 Advocate Beach field campaign (Fig. 4.4, p. 33; Fig. 5.3, p. 63) was carried out between 21 September and 9 October (i.e., yeardays 264-282), with the purpose of characterising the vertical pore pressure response of the bed under wave loading, and the morphodynamics of beach cusps. Data were obtained primarily using arrays of buried pressure sensors and a fixed-frame video system. The pore pressure response was evaluated in terms of the depth dependence of the attenuation and phase of the oscillatory component of the pore pressure signal through the mixed sand-gravel medium. Beach cusp morphodynamics were observed by tracking the time evolution of video-derived shoreline estimates.

Measurements of sediment pore water pressure were made using a vertical array of four MS5803-14BA high resolution (0.02 kPa) pressure sensors spanning the upper 50 cm of the sediment column (0, 15, 30, and 50 cm sediment depth), near the mid-tide level. Each sensor was secured in an acrylic housing, the openings of which were covered in aluminum mesh to prevent the mechanical force of sand grains from impinging on the sensing surface. The array was installed on yearday 265, and operated from yearday 266 to 281. The verticality of the array was established during installation using a spirit level, and was confirmed to still be vertical upon the excavation of the array at the end of the campaign. Data were sampled at a mean rate of 50 Hz, then resampled at 20 Hz for analysis. Two BeagleBone Black single-board computers were used for data logging. The BeagleBones were networked and time synchronised using Precision Time Protocol (PTP) via a junction box at the top of the berm to ensure accurate phase estimates. Power was supplied from a building behind the dune crest. Additional pressure measurements were made using sensors arranged in longshore and cross-shore arrays between the mid- and high tide levels for the purpose of observing low mode edge waves. The sensors in the longshore and cross-shore arrays were buried 30 cm deep in the beach and ported to the beach surface to avoid potential phase-shifting effects introduced by the sediment.

Video imagery was recorded daily from a fixed-frame camera installed atop a 5.3 m tower on the beach crest, facing southward. The camera field of view contained the intertidal zone, and spanned approximately 30 m of shoreline at spring high tide and nearly 100 m at low tide. The images were georectified and rotated into local coordinates, with x alongshore, positive to the northwest, y positive offshore, and the origin defined as the

position of the vertical pressure sensor array – roughly 20 m seaward of the nominal high tide shoreline. Video was recorded with a resolution of 1920x1080 pixels at 2 Hz for roughly 6 hours per tide during daylight, corresponding when possible with the period before, during, and after high tide.

Time-averaged images were used to estimate the shoreline position and track the evolution of the swash zone morphology over the course of selected high tides. The averaging interval was three minutes (360 frames). Here, the term "shoreline" is defined to be the x-y position of the water's edge, as determined from the three-minute time-averaged imagery. The video-tracked shorelines were used to estimate the wavelengths and amplitudes of beach cusps. The instantaneous position of the water's edge was tracked using 'timestack' images composed of cross-shore pixel transects (i.e., fixed x-coordinate) from the 2 Hz images stacked consecutively through time. The timestacks were used to estimate swash runup statistics.

Pressure measurements for monitoring incident wave conditions were obtained using an internally logging RBR Duo, deployed on an above-bed frame near lowest low water, sampling continuously at 6 Hz between yeardays 267 and 281. Laboratory measurements of sediment porosity and hydraulic conductivity were made following the experiment, using sediment samples collected from the upper beach face. Hydraulic conductivity was estimated using constant head permeameter tests, as outlined by *Craig* (1974). Grain size distributions were obtained following the method of *Ingram* (1971).

Beach surveys were carried out at each daylight low tide using a cart-mounted RTK (real time kinematic) GPS.

The forcing conditions during the experiment were characterised by periods of wave inactivity (yeardays 265-270 and 275-277), owing both to light winds and to winds from the N-NE (offshore), and interspersed with wind events from the SW, leading to the steep, locally generated wind and swell waves that are characteristic of the Bay of Fundy. The first, and largest, of the wind events lasted two days (yeardays 270-271) with peak significant wave heights approaching 1.5 m. Two other SW wind events occurred on yeardays 274 and 281. During the period from yearday 277 to 280, wave energy spectra were dominated by long period ($>$15 seconds), low amplitude (0.05-0.15 m) swell waves generated by Hurricane Joaquin which passed well to the south of Nova Scotia. The mean peak period, computed for storms (tide-averaged significant wave heights greater than 0.15

m) and intervals between storms, was 7.6 seconds and 9.7 seconds, respectively.

3.3 2018 Field Experiment

The 2018 Advocate Beach experiment (Fig. 6.1, p. 87; Fig. 7.1 p. 118) was conducted between 14 and 27 October, with an emphasis on the coevolution of bed level and mean surficial grain size both at the beach scale and at the scale of the swash zone, and on Lagrangian tracking of natural cobble tracers in swash flows. At the beach scale, bed level and grain size were observed using GPS and photo surveying each low tide. An array of ultrasonic range sensors and cameras was used to observe the subaerial bed level and grain size at the swash scale, and video data used for the Lagrangian particle tracking. The experiment spanned 27 tides, which are referred to by their low tide index within the experiment, i.e., 1 though 27.

Local grid coordinates were defined in keeping with a previous experiment at the site, with the origin defined as the former position of a vertical pressure sensor array (see Chapter 3.2), approximately 20 m seaward of the nominal high tide shoreline. x is alongshore, positive to the northwest, and y is positive offshore.

Beach-scale monitoring of bed elevation and beach surface grain size was carried out using RTK (real time kinematic) GPS and camera surveys. A survey grid (Fig. 6.1) was established consisting of one cross-shore beach transect spanning 90 m and two longshore transects spanning 75 m, all sampled at 3 m intervals, as well as a more densely sampled grid, consisting of six 24 m longshore transects spaced at 1 m intervals, and 2 m intervals across-shore. The cross-shore transect spanned from the beach crest to the mean spring tide low water shoreline along the $x = 0$ m coordinate, though the number of surveyed points differed from tide to tide depending on the shoreline position at the time of the survey. The two longshore transects were positioned on the upper beach face, but seaward of the nominal high water line. The most seaward transect was positioned at $y = -5$ m, and the more shoreward transect at $y = -13$ m. The densely sampled grid, and the larger grid layout in general, were designed to encompass the high tide shoreline, in order to emphasise high tide swash processes.

The survey grid was sampled every low tide from tide 14 to 27, an RTK GPS position and photograph being taken at each grid point. Photographs were taken using a 20 megapixel Canon Powershot Elph 190 camera, mounted to a tripod at fixed height. Prior to tide 14,

different grid configurations were surveyed, and only one survey was conducted per day (i.e., once per two tides). Survey data collected prior to tide 14 are not included in any analyses.

A wavelet-based digital grain sizing package (see *Buscombe*, 2013), implemented in Python, was used to estimate arithmetic grain size statistics from the survey photographs. The DGS algorithm does not require calibration, and takes as input a grain-resolving image containing only sediment. The survey images were cropped to half width and height, centred in the frame, corresponding to a field of view at the bed of 0.33×0.25 m, assuming a camera height of 0.3 m above the bed. The pixel to physical unit scaling was computed by photographing an object of known length and width. The same scaling was used for all survey images.

At the swash scale, data were collected using a four-element array of collocated ultrasonic range sensors and cameras, along with an overhead camera used for tracking the movements of tracer cobbles in the swash. Both systems were mounted over the swash zone during periods of low to moderate energy forcing conditions.

The coincident evolution of beach morphology and sediment properties in the swash zone was investigated using an array of collocated Maxbotix MB7383 HRXL ultrasonic range sensors (range resolution of *ca*. 1 mm) and 5 megapixel Raspberry Pi cameras. The array consisted of four downward-facing range sensor-camera pairs, cantilevered approximately 2 m over the swash zone on an instrument frame that could be moved with the changing shoreline position. The pairs were separated by 0.9 m alongshore (i.e., having a total longshore span of 2.7 m), and at a nominal elevation of 0.75 m above the bed. The range data were sampled at 6 Hz, and the images at 0.2 Hz. Each of the four array element pairs were controlled by a Raspberry Pi single board computer, on which the data were also logged. The four computers were time-synchronised using network time protocol (NTP), and powered from a 12 V marine battery. The instrument frame was assembled near the high water line and data were collected at 3-5 "stations" during late flood tide, high tide, and early ebb. At each flood tide station, sampling was initiated prior to the maximum swash runup position passing beneath the array, and continued until the bed was fully obscured by water (i.e., the swash zone was no longer in the instruments' field of view). At ebb stations, the frame was positioned so that the transition from full water cover to fully-exposed bed could be captured. The longest sampling periods corresponded

to high tide, when the array stations could be held through the shoreline's advance and retreat, from late flood into early ebb. The position of each array element was recorded using RTK GPS at each station. Images of the exposed bed (i.e., between instances of swash runup) captured by the Raspberry Pi cameras were processed using the same digital grain sizing algorithm used to analyse the survey images.

An overhead Raspberry Pi camera used for monitoring tracer cobble transport in the swash zone was mounted to a second instrument frame. The frame consisted of a semi-stationary base which could be moved with the changing shoreline position, and a moveable arm which supported the camera, allowing it to view the swash zone from a height of *ca*. 3 m without the frame base being in the image. The image field of view at the beach surface was approximately 2.4 by 4.3 m (longshore by cross-shore). During low to moderate wave energy conditions, the overhead camera frame occupied 3-5 stations near the high water line. A minimum of three ground control points were captured at each station using RTK GPS to provide a scaling between pixel and ground coordinates. Prior to deployment, cobbles were sieved into three different size classes: 22.4-31.5 mm, 31.5-45 mm, and 45-63 mm. The cobbles were painted blue, orange, and yellow, respective to each size class. The camera frame stations were typically chosen to capture cobble transport during high tide and early ebb, so the cobbles could be retrieved and redeployed after the shoreline had retreated. The frame held a station until the camera's field of view no longer contained the mean shoreline position. Video was recorded continuously throughout.

The alongshore orientation of the four range sensor-camera elements on the array frame was chosen to capture the development of beach cusps, or other three-dimensional morphology in the alongshore, though no beach cusp events were satisfactorily captured. The geometries of both instrument frames (i.e., their fields of view in relation to their bases, which were in contact with the beach surface) were chosen so that the mid-swash zone could be sampled without the bases of the instrument frames interfering with either the data collection, or the swash processes being observed. This limited the use of the frames to 'fairweather' conditions, during which the maximum swash runup distance was less than approximately 4 m, favourable for cusp formation (*Guest and Hay*, 2019). The majority of tides were characterised by high steepness, wind-band incident waves leading to an energetic shorebreak. There were three periods of fairweather forcing characterised by low amplitude, low steepness waves during which the swash array frame could be deployed:

tides 15-16, tides 19-22, and tide 27.

An RBR Duo pressure sensor was deployed on a heavily weighted frame resting on the bed near the neap low water shoreline to observe the “offshore” wave climate. Due to a prolonged period of high winds and energetic wave conditions at the outset of the experiment, the pressure sensor was not deployed until the sixth day of the experiment (prior to tide 10). Pressure data were recorded at 6 Hz.

CHAPTER 4

VERTICAL STRUCTURE OF PORE PRESSURE UNDER SURFACE GRAVITY WAVES ON A STEEP, MEGATIDAL, MIXED SAND-GRAVEL-COBBLE BEACH

This chapter was first published in the *Journal of Geophysical Research: Oceans*[1].

4.1 Introduction

In sandy, wave-forced nearshore environments, synchronous measurements with multiple pressure and velocity sensors arranged in along- and/or across-shore arrays enable determination of essential characteristics of the nearshore incident and forced wavefield, including e.g., resolving shoreline-trapped modes via wavenumber-frequency and wave-directional spectra (e.g., *Huntley et al.*, 1981; *Oltman-Shay and Guza*, 1987). Direct measurement of *in situ* hydrodynamics in the surf and swash zones of steep mixed sand-gravel (MSG) beaches is challenging in comparison, owing to the high likelihood of instrument damage by impact from gravel to cobble-sized grains. With this factor as a contributor, and despite contemporary interest in MSG beaches arising from their acknowledged role as effective natural shoreline defences, our current understanding of hydrodynamic and sediment transport processes in these environments is limited (*Mason and Coates*, 2001; *Osborne*, 2005). The use of pressure sensors buried beneath the active sediment layer on the beach

[1] **Guest, T. B.**, and A. E. Hay, Vertical structure of pore pressure under surface gravity waves on a steep, megatidal, mixed sand-gravel-cobble beach, *Journal of Geophysical Research: Oceans*, 122, 153–170, 2017.

face represents a potential means of *in situ* data collection while reducing the instrument vulnerability associated with above-bed deployment.

It is well known (e.g., *Yamamoto et al.*, 1978) that wave-induced pressure signals propagating vertically through a porous bed will in general experience frequency-dependent amplitude attenuation and phase shifting, the magnitudes of which are determined by elastic and fluid mechanical properties of the skeleton built from the solid particle phase and the interstitial fluid, respectively. Under certain conditions, i.e., pore pressure phase shift, the passage of a single wave trough can induce a vertical pressure gradient sufficiently large to overcome static gravitational equilibrium, leading to momentary sediment liquefaction, with implications for seabed stability (e.g., *Sakai et al.*, 1992; *Bonjean et al.*, 2004; *Mory et al.*, 2007). Based on the theory of three-dimensional consolidation of porous granular media put forward by *Biot* (1941), numerous models have been developed (*Putnam*, 1949; *Sleath*, 1970; *Massel*, 1976; *Madsen*, 1978; *Yamamoto et al.*, 1978; *Mei and Foda*, 1981; *Okusa*, 1985, and many more), incorporating varied assumptions concerning the compressibility of the bed and fluid, (an)isotropy, magnitude of strains, etc. For a comprehensive review of porous bed response models, the reader is referred to *Jeng* (2003). Many of these models have successfully reproduced the observed pressures in beds of various composition. For example, *Sakai et al.* (1993) compared field observations of pore-pressure in a saturated bed of medium sand to the boundary layer theory of *Mei and Foda* (1981), and reported minimal attenuation and phase lag. *Raubenheimer et al.* (1998) tested the ability to use measurements from a single pressure sensor buried in a beach consisting of fine sand to estimate wave height in the field. Using the *Yamamoto et al.* (1978) model, their findings indicated that attenuation of pore-pressure signals with burial depth was independent of their sediment properties, and that phase shifts were negligible. *Pedrozo-Acuña et al.* (2008) compared predictions from the Yamamoto model to observed pore pressure amplitudes within a gravel beach in a laboratory wave flume, with no phase lag values reported. *Michallet et al.* (2009) observed large pore pressure attenuation and phase lags with sediment depth in front of a large concrete structure in the intertidal zone of medium sand beach. Their results indicated that conditions conducive to wave-induced momentary liquefaction were often reached, and comparison with the model presented by *Sakai et al.* (1992) was consistent with interstitial trapped air as a key parameter affecting the transmission of pressure within the sediment.

The studies summarised above present results from laboratory investigations (e.g., *Pedrozo-Acuña et al.*, 2008, gravel beach) and meso- to macrotidal beaches consisting of fine to medium sand (e.g., *Raubenheimer et al.* (1998), 2-2.5 m tidal ranges, fine sand; *Michallet et al.* (2009), *ca*. 4 m tidal range, medium sand). In contrast to these studies, the present work considers the case of a megatidal (10-12 m range), steeply sloping, natural MSG beach environment. The objectives are twofold: (1) to characterise the depth dependence of the phase lag and attenuation of oscillatory pore water pressures induced by surface gravity waves and (2) to test the feasibility and potential challenges associated with using buried pressure sensors to estimate surface wave-field characteristics on steep MSG beaches.

The paper is organised as follows: The basics of the theory and the Yamamoto model are outlined in Section 4.2, followed by a description of the experiment site, the instrumentation employed, and the analysis methods in Section 4.3. The results are presented in Section 4.4, beginning with a summary of hydrodynamic conditions, pore-pressure attenuation, and phase results spanning the full experiment. Then the sediment depth dependence of the modeled pressure response is compared to observed pressure for a single tide. Discussion and conclusions follow in Sections 4.5 and 4.6.

4.2 Theory

Biot (1941) derived a system of linear, multi-phase, poro-elastic equations describing the flow of fluid through, and the elastic deformation of, a porous medium, based on the assumptions of (1) an isotropic soil skeleton, (2) linear, reversible (i.e., Hookean) stress-strain relations within the soil skeleton, (3) small strains, and (4) Darcian fluid flow. Based on the work of Biot, *Yamamoto et al.* (1978) developed an analytic model treating the transmission of wave pressure signals through a porous bed. The Yamamoto model is considered to be quasi-static, owing to the assumption of small deformations in the medium, and no acceleration due to fluid and/or soil motion.

For an infinitely deep seabed, the ratio of the amplitude of the oscillatory component of pore pressure, $p(z)$, at sediment depth z (positive downward, with $z = 0$ at the sediment-water interface) to that at the bed surface, p_0, is given by (*Yamamoto et al.*, 1978)

$$\frac{p(z)}{p_0} = \Big[1 - \frac{im\omega''}{-\tilde{k}'' + i(1+m)\omega''}\Big] \exp(-\tilde{k}z) + \frac{im\omega''}{-\tilde{k}'' + i(1+m)\omega''} \exp(-\tilde{k}'z), \quad (4.1)$$

where ω and $\tilde{k}$ are the radian frequency and wavenumber of the surface gravity waves in the overlying fluid, and satisfy the linear dispersion relation $\omega^2 = g\tilde{k}\tanh(\tilde{k}h)$, with h the water depth. The parameters m, ω'', $\tilde{k}'$, and $\tilde{k}''$, defined below and in Appendix A, are functions of the sediment porosity n, hydraulic conductivity k_c (sometimes referred to as the coefficient of permeability), the shear modulus G of the porous matrix, Poisson's ratio ν, and the effective compressibility β' of the pore fluid.

If the pore fluid is free of air, β' is equal to the compressibility of water β. If the pore fluid contains trapped air bubbles, β' is significantly increased, and is related to β by

$$\beta' = S\beta + \frac{1-S}{P}, \quad (4.2)$$

where $S = S(z)$ is the degree of saturation and $P = P(z)$ is the absolute pore-water pressure. Equation (4.2) is readily derived from first principles, assuming the ideal gas law for isothermal conditions – giving $\beta_a = 1/P$ for the bulk compressibility of air – and conservation of volume. P is here given by

$$P(z) = \rho g(h+z) + P_a, \quad (4.3)$$

where h is the mean local water depth, and P_a is atmospheric pressure. In our implementation, both S and P vary in accordance with the ideal gas law for isothermal conditions, applicable to spherical bubbles smaller than 1.2 cm diameter (*Leighton*, 1994, p.178). We note that the factor S in the first term on the right hand side of equation (4.2) is missing from equation 2.2 in Yamamoto et al., but is clearly required since the bulk compressibility of water cannot affect that of the pore fluid when $S = 0$.

The weighting of terms in equation (4.1) is determined by the parameter m, given by

$$m = \frac{nG\beta'}{1-2\nu}. \quad (4.4)$$

The product $G\beta'$ indicates the stiffness of the porous matrix relative to the pore fluid. In the limit $G\beta' \to 0$, the case for fully saturated sands and gravels, $m \to 0$ and equation

(4.1) becomes

$$\frac{p(z)}{p_0} = \exp(-\tilde{k}z). \tag{4.5}$$

The pressure signal at depth in the sediment is in phase with that at the sediment water interface, and the exponential decay of the amplitude with depth is independent of the mechanical properties of the soil. This is the case which *Raubenheimer et al.* (1998) found to be consistent with their measurements in the surf and swash zones of two sandy beaches with *ca*. 2–2.5 m tidal ranges and 1:20 to 1:30 beach slope.

For the case of $G\beta' >> 0$, $m \neq 0$ and a second vertical scale is introduced, given by

$$\tilde{k}'(z) = \tilde{k}\Big\{1 + \frac{i\gamma\omega}{k_c\tilde{k}^2}\Big[n\beta' + \frac{1-2\nu}{2(1-\nu)G}\Big]\Big\}^{1/2}, \tag{4.6}$$

where γ is the unit weight of the pore fluid. The phase lag at depth differs from that at the bed surface and attenuation at depth is increased, owing primarily to the effective compressibility of the fluid (i.e., the degree of saturation). Decreasing the saturation leads to an increase in the magnitude of the complex wavenumber $\tilde{k}'$ (Fig. 4.1) and the phase difference. Simplifications to equation (4.6) are presented in Appendix A for the set of parameter values specific to the study site introduced in Section 4.4.2, allowing a more straightforward interpretation of the influence of $\tilde{k}'$ on the pore pressure response.

When $m >> 0$ (e.g., unsaturated sands and gravels), equation (4.1) can be approximated by

$$\frac{p(z)}{p_0} = \exp(-\tilde{k}'z). \tag{4.7}$$

In the case of partial saturation, mechanical properties of the porous medium must be considered by employing the full analytical solution (4.1), or the approximation (4.7).

Model output from equations (4.1) and (4.5) is shown in Fig. 4.2, with input parameter values set to be representative of the field site introduced in Section 4.4.2. Though the pore-pressure phase lags modeled by equation (4.1) continue increasing with sediment depth, the signals are almost entirely attenuated within $O(1\text{ m})$ below the beach surface.

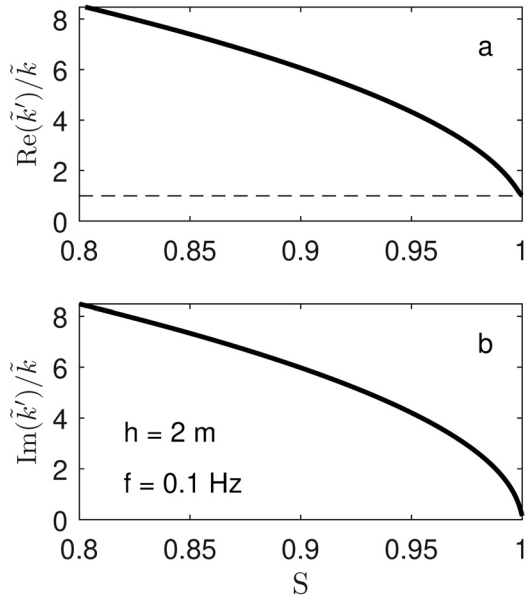

Figure 4.1: The ratio of radian wavenumbers $\tilde{k}'$ (equation (4.6)) to $\tilde{k}$ (the surface gravity wavenumber determined using the linear wave dispersion relation) is plotted versus saturation S for the (a) real and (b) imaginary components of $\tilde{k}'$. $\tilde{k}' >> \tilde{k}$ when $S < 1$, leading to the presence of a phase lag and greater attenuation. When $S \rightarrow 1$, $\tilde{k}' \rightarrow \tilde{k}$ and the full solution, equation (4.1), is reduced to the exponential result, equation (4.5).

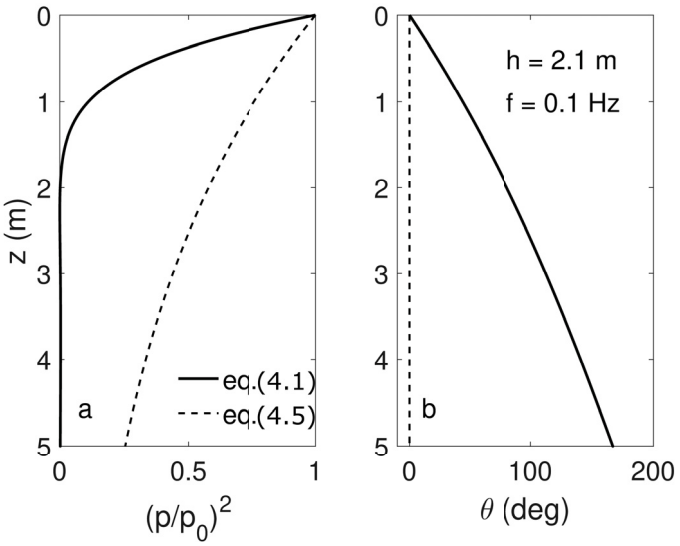

Figure 4.2: Modeled profiles of (a) pressure variance ratio and (b) phase lag, with input parameter values representative of Advocate Beach sediments ($S(z = 0) = 0.9$, $k_c = 7.6\times10^{-4}$ m s^{-1}).

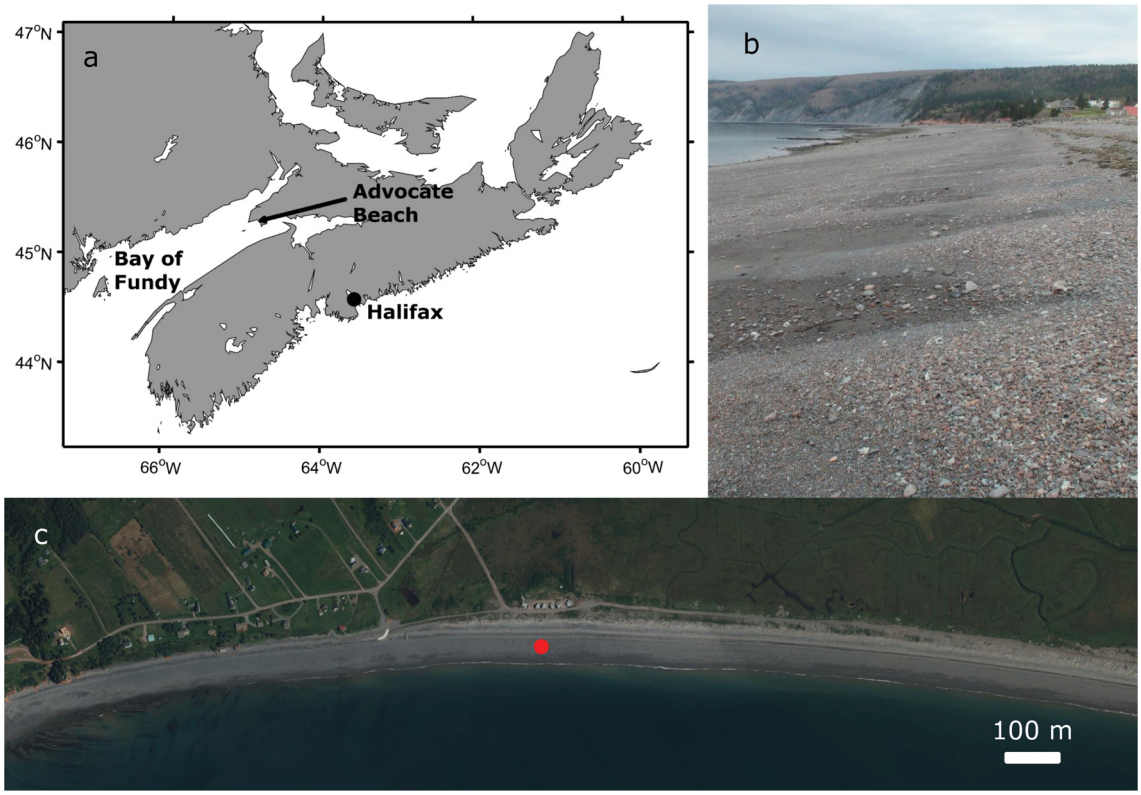

Figure 4.3: (a) Map indicating the location of Advocate Beach, near the head of the Bay of Fundy, Canada. (b) Image of Advocate Beach taken near the high tide mark at low tide, in the presence of well organised cusps. (c) Aerial view of Advocate Beach. The array location is indicated by the red dot.

4.3 Methods

4.3.1 Field Site

In this study, measurements from a vertical array of buried pressure sensors are used to determine the dependence of signal phase and attenuation in the sea and swell bands on sediment depth at Advocate Beach, Nova Scotia, Canada – a coarse-grained, megatidal (10-12 m range) barrier beach located near the head of the Bay of Fundy (Fig. 4.3). Megatidal beaches, as defined by *Levoy et al.* (2000), have spring tidal ranges exceeding 8 m. The field experiment was undertaken between 21 September and 9 October (i.e., yeardays 264-282) 2015, and was initially motivated by questions related to possible phase-shifting effects of Advocate Beach sediments on wave pressure signals. The beach face sediments range from medium sand to $>$ 20 cm diameter cobbles, well-mixed both across-shore and at depth. The steep ($\approx 1:10$) slope and mixed-size, poorly sorted sediment identify

Advocate as a mixed sand and gravel (MSG) beach under the field-based classification scheme proposed by *Jennings and Shulmeister* (2002). The beach is 5 km long and has a nearly linear shoreline, separating the headlands of Cape Chignecto to the west, and Cape D'Or to the southeast. The beach face is exposed to the full 500 km fetch of the Bay of Fundy and adjacent Gulf of Maine. At low tide, the beach face is uniformly planar and the intertidal zone up to 100 m wide during spring tides (see *Taylor et al.*, 1985; *Hay et al.*, 2014). From the lower beach face to beneath lowest low water, the beach composition transitions to cobble and boulder-sized material. Well-sorted beach cusps are often seen to form on the upper beach, with cusp horns typically composed of loose gravel and cobbles, and fine material in the embayments. Sediment sorting has also been observed to follow energetic wave events in the form of widespread fining of the surficial material (*Hay et al.*, 2014). During storms, peak incident wave periods typically fall within the wind-wave band (T_p = 5.5-6 seconds), with longer period swell usually limited to the weaker wave forcing conditions between storms. The combination of a steep beach slope and typically short period, wind-generated incident waves in the Bay of Fundy result in a highly energetic shore break for significant wave heights of *ca.* 0.5 m and larger (*Hay et al.*, 2014).

Results from earlier field deployments (2012, 2013) at Advocate Beach are presented in *Hay et al.* (2014), *Stark and Hay* (2014), *Stark et al.* (2014), and *Wilson et al.* (2014). The reader is referred to these articles for further site characterisation and observations of sediment and hydrodynamics.

4.3.2 Measurements

Pore-pressure was measured using a vertical array of four MS5803-14BA high resolution (0.02 kPa) pressure sensors, at 0, 15, 30, and 50 cm sediment depth and near the mid-tide level on the beach face (Fig. 4.4). Each sensor was secured in an acrylic housing, the openings of which were covered in aluminum mesh to prevent the mechanical force of sand grains from impinging on the sensing surface. The array was installed on yearday 265, and operated from yearday 266 – 281. Data were sampled at a mean rate of 50 Hz, then resampled at 20 Hz for analysis. Resampling was necessary to ensure a uniformly sampled time vector, and 20 Hz provided ample spectral frequency resolution (0.0098 Hz with a window width of 2048) for our purposes. Two BeagleBone Black single-board computers were used for data logging. The BeagleBones were linked via Ethernet and synchronised using Precision Time Protocol (PTP) via a junction box at the top of the

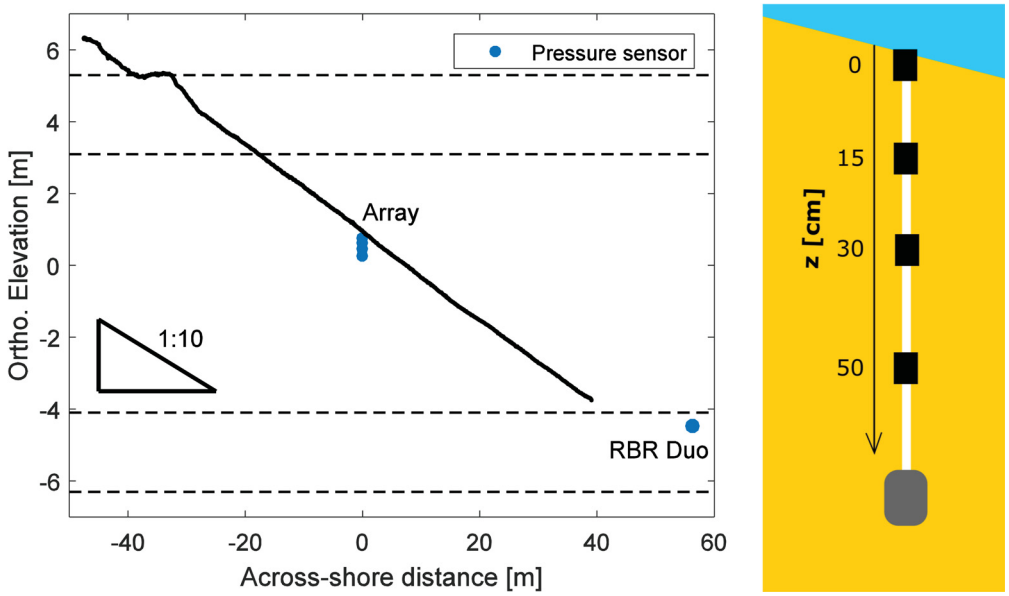

Figure 4.4: Left: Cross-shore profile of Advocate Beach on yearday 271, 2015. Pressure sensor positions are indicated by blue dots, with the vertical pressure sensor array identified near mid-beach. Highest high and lowest low water during spring and neap tides during the experiment are indicated with dashed lines. Right: A schematic of the vertical array.

berm. Power was supplied from a chalet behind the dune crest. Two of the four sensors ($z = 0$ cm [beach surface], $z = 30$ cm) failed near high tide during the first data collection cycle as a result of seawater intrusion at the cable connection points, yielding a limited record length of approximately 2 hours over which to perform the desired analysis with the full array. The remaining two sensors ($z = 15$ cm, $z = 50$ cm) operated throughout the experiment (29 tidal cycles). Water depth h was determined using the deepest sensor. The uppermost sensor ($z = 0$ cm) was visible at the beach surface at low tides throughout the experiment, with the exception of a 2-3 day period of burial which occurred during low amplitude, long period swell on yeardays 277-280. Additional pressure measurements for monitoring incident wave conditions were made using an internally logging RBR Duo, deployed on an above-bed frame near lowest low water, sampling continuously at 6 Hz between yeardays 267 and 281.

Beach surveys were carried out at each daylight low tide using a cart-mounted Hemisphere Model S320 RTK (real time kinematic) GPS. A typical beach profile is shown in Fig. 4.4.

Relevant sediment properties were obtained from samples collected at five depth increments (0-5, 5-15, 15-25, 25-35, and 35-50 cm), 1 m from the location of the vertical

Table 4.1: Measured porosity, n, and hydraulic conductivity, k_c. Measurements were made in the laboratory on samples collected in the 5 depth intervals indicated, with the coarse fraction ($D > 16$ mm) removed. The porosity was corrected to account for the coarse fractions by assuming $n[D > 16 \text{ mm}] = 0$.

depth, z (cm)	n (corrected)	n (fines)	k_c (10^{-4} m s^{-1})
0–5	0.305 ± 0.008	0.335 ± 0.008	11.257 ± 0.442
5–15	0.259 ± 0.009	0.295 ± 0.007	7.930 ± 0.435
15–25	0.230 ± 0.006	0.284 ± 0.005	7.392 ± 0.105
25–35*	0.150 ± 0.006	0.208 ± 0.003	5.396 ± 0.089
35–50	0.194 ± 0.006	0.248 ± 0.002	7.613 ± 0.074
depth average	0.217 ± 0.053	0.265 ± 0.043	7.553 ± 1.709

*Computed for $D < 22.4$ mm due to a higher percentage of coarse material.

array on yearday 277. To collect the samples, a pit was dug, with one of its walls carefully maintained as a vertical face. Samples were collected from the top down, in a column, with care taken to ensure that material for each sample was taken only from within the pre-determined depth increment. Grain size distributions were obtained following the method of *Ingram* (1971). Grains with diameter $D > 16$ mm were removed from the samples prior to carrying out the measurements of sediment porosity, n, and hydraulic conductivity, k_c. Porosity was estimated volumetrically using a 1 L graduated cylinder. Distilled water was added first, to prevent the entrainment of air bubbles in the sediment, which was then added in 6-9 250 g (approx.) increments with displaced water volume and bulk sample volume noted at each addition. The mean value and standard deviation of n were then obtained via linear regression, and the result corrected to account for the volume of gravel and cobbles removed ($n[D > 16 \text{ mm}] = 0$). The hydraulic conductivity of each sample was estimated with a permeameter using the constant head method outlined in *Craig* (1974). Each sample was added incrementally to the water-filled permeameter cell (7.6 cm diameter), to prevent both air entrainment and grain size-segregation. Three successive measurements – with the sample removed and reintroduced each time – were used to estimate the mean and standard deviation of k_c for each depth bin. No correction was made for the omitted large size fractions.

Measurements of grain size, porosity, and hydraulic conductivity are presented in Fig. 4.5, with porosity and hydraulic conductivity measurements also summarised in Table 4.1. Note that both n and k_c tend to decrease with depth in the sediment. The porosity values reported here are comparable with those found by *López de San Román-Blanco et al.*

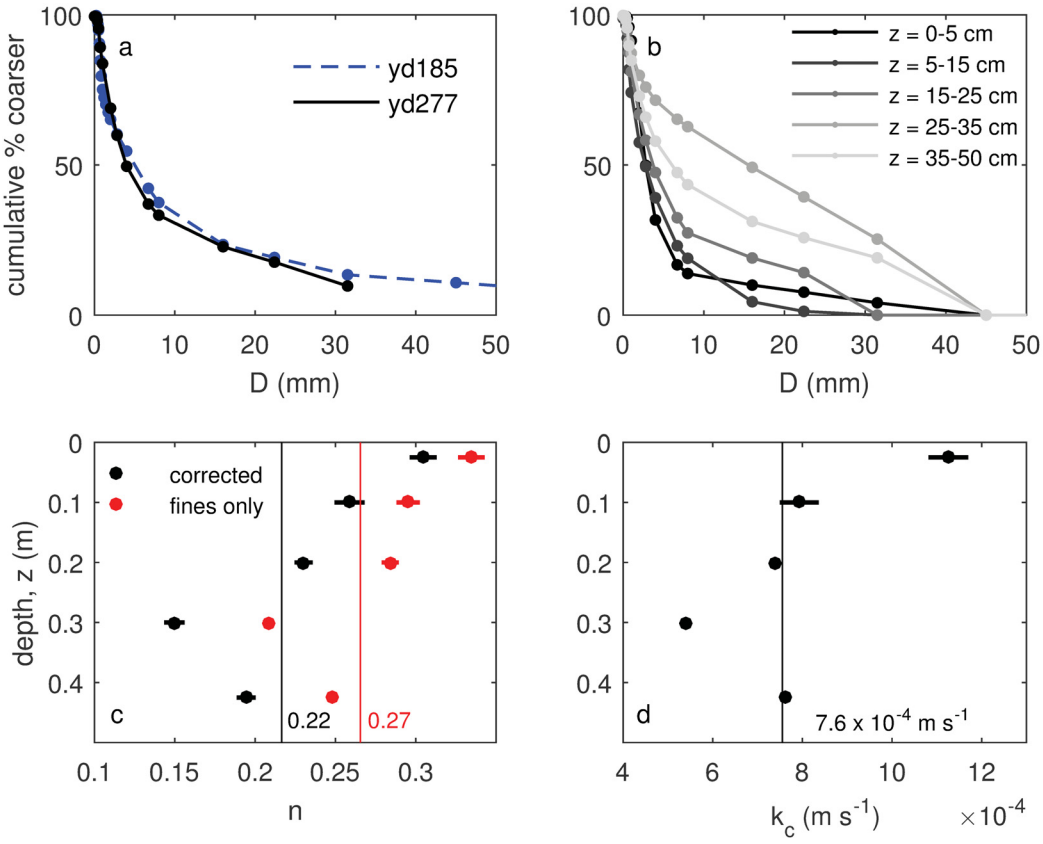

Figure 4.5: Advocate Beach sediment properties. (a) Bulk grain size distributions from yearday 277 (during the experiment) and yearday 185 (an earlier test deployment). (b) Size distributions at 5 depth bins $\approx$ 1 m from the array location (samples collected on yearday 277). (c) Porosity n associated with each depth bin, corrected to account for large size fractions (black) and for fine fractions only ($D < 16$ mm, red). (d) Hydraulic conductivity k_c associated with each depth bin. Depth-averaged values in (c) and (d) are indicated by vertical lines, and the error bars indicate the standard deviation of the estimate at each depth.

(2006), who reported a starting porosity of approximately 0.2 for a 30:70% sand:gravel mixture used in a laboratory wave flume experiment, with values varying between 0.2 and 0.4 as the mix ratio varied (on yearday 185, Advocate beach had a sand:gravel:cobble mix ratio of 35:58:7%). Few measurements of the hydraulic conductivity of natural MSG beach sediments have been reported in the literature, however the values reported here fall within the range typical for a sand-gravel mixture – roughly 10^{-1} to 10^{-4} m s^{-1} (*Craig*, 1974).

4.3.3 Analysis

In keeping with previous work (e.g., *Raubenheimer et al.*, 1998; *Michallet et al.*, 2009), and for straightforward comparison of observed and modeled pressure results, pressure variance and spectral density ratios are used as metrics for quantifying attenuation. The theoretical prediction at a given frequency is given by $[(p(z)/p_0)^2]$, hereafter written as $(p/p_0)^2$, and is compared with the observed spectral ratio $S_{pp}(f,z)/S_{pp}(f,0)$ (hereafter written as $S_{pp}/S_{pp,0}$). Variance attenuation is then given by the complement of these values, $[1-(p/p_0)^2]$ and $[1-S_{pp}/S_{pp,0}]$, respectively. The observed phase lag, $\theta(z)$, was determined from the cross-spectrum of $p(z)$ and p_0, unless otherwise indicated.

Owing to the large tidal range at this location, water depth changes rapidly on the rising and falling tide. Thus, spectral estimates were computed using detrended 12 minute records (maximum change of 0.6 metres mean water level), to assure quasi-stationarity. A Hanning window of length 2048 samples (102.4 seconds) was used, with 50% overlap. The resulting spectra have a frequency resolution of 0.0098 Hz and 24 degrees of freedom.

4.4 Results

4.4.1 Observed Forcing and Response

The hydrodynamic forcing conditions during the experiment are presented in Fig. 4.6. Periods of wave inactivity (yeardays 265-270 and 275-277), owing both to light winds and to winds from the N-NE (offshore), were interspersed with wind events from the SW, leading to the steep, locally generated wind and swell waves that are characteristic of the Bay of Fundy. The first, and largest, of the wind events lasted two days (yeardays 270-271) with peak significant wave heights approaching 1.5 m. Two other SW wind events occurred on yeardays 274 and 281. During the period from yearday 277 to 280, wave energy spectra

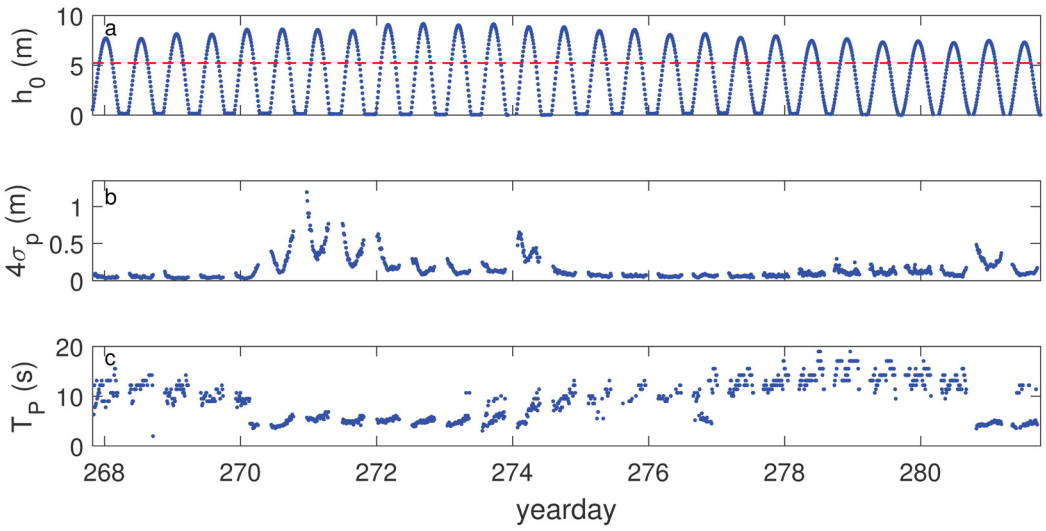

Figure 4.6: Hydrodynamic conditions during the experiment, registered by the frame-mounted RBR Duo pressure sensor near lowest low water. (a) Tidal elevation, h_0, with the relative level of the uppermost pressure sensor in the array indicated by the dashed red line. (b) Significant wave height, computed as $4\sigma_p$. (c) Peak wave period, T_p.

were dominated by long period (>15 seconds), low amplitude (0.05-0.15 m) swell waves generated by Hurricane Joaquin which passed well to the south of Nova Scotia. The mean peak period, computed for storms ($4\sigma_p > 0.15$ m) and intervals between storms, was 7.6 seconds and 9.7 seconds, respectively. Mean peak wave periods measured during two previous studies were 5.5-6 seconds (e.g., *Hay et al.*, 2014).

The data from the vertical array while all four sensors were functioning are presented in Fig. 4.7. Visual inspection of the four pressure fluctuation time series (Fig. 4.7a) indicates attenuation of the dominant wave signal with depth of burial in the sediment. The pressure records from the buried sensors also can be seen to lag the surface record increasingly with burial depth. Pressure spectra from the respective sensors (Fig. 4.7b) reflect the observed attenuation with depth, with variance ratios decreasing – i.e., attenuation increasing – with increasing frequency (Fig. 4.7c), consistent with past observations (*Yamamoto et al.*, 1978; *Raubenheimer et al.*, 1998; *Pedrozo-Acuña et al.*, 2008, etc.). Fig. 4.8 shows the magnitude squared coherence of the signals, which was generally above the significance level (95% confidence) for frequencies below 0.6 Hz at high tide, and up to 1 Hz in shallower water. Phase lags are also frequency dependent, with smaller lags at lower frequencies.

The pressure variance ratio and phase at sea and swell band frequencies are dependent on water depth, h, as well as changes to the beach state over the course of the experiment.

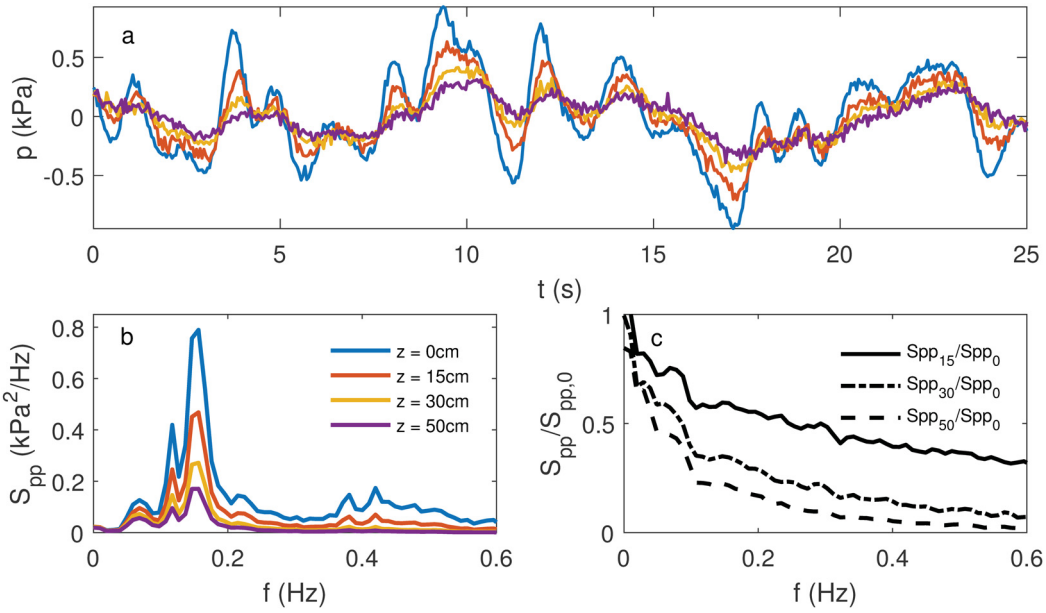

Figure 4.7: Pressure time series (a) and energy spectra (b) at the four sensor burial depths for $h = 50$ cm on yearday 266. A decrease in spectral pore-pressure ratios (c) across much of the gravity wave band indicates frequency-dependent attenuation. The subscripts in the legend in (c) indicate sediment depth in cm.

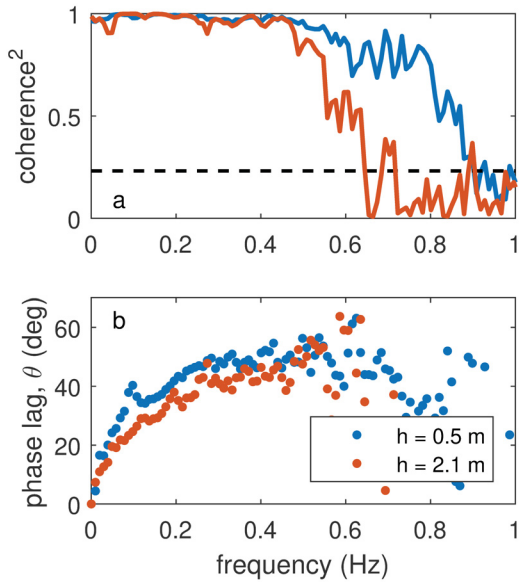

Figure 4.8: Coherence (a) and phase (b) of the deepest sensor ($z = 0.5$ m) relative to the bed surface sensor ($z = 0$ m) for mean local water depths $h = 0.5$ m and $h = 2.1$ m on yearday 266. The 95% significance level is indicated with a dashed black line.

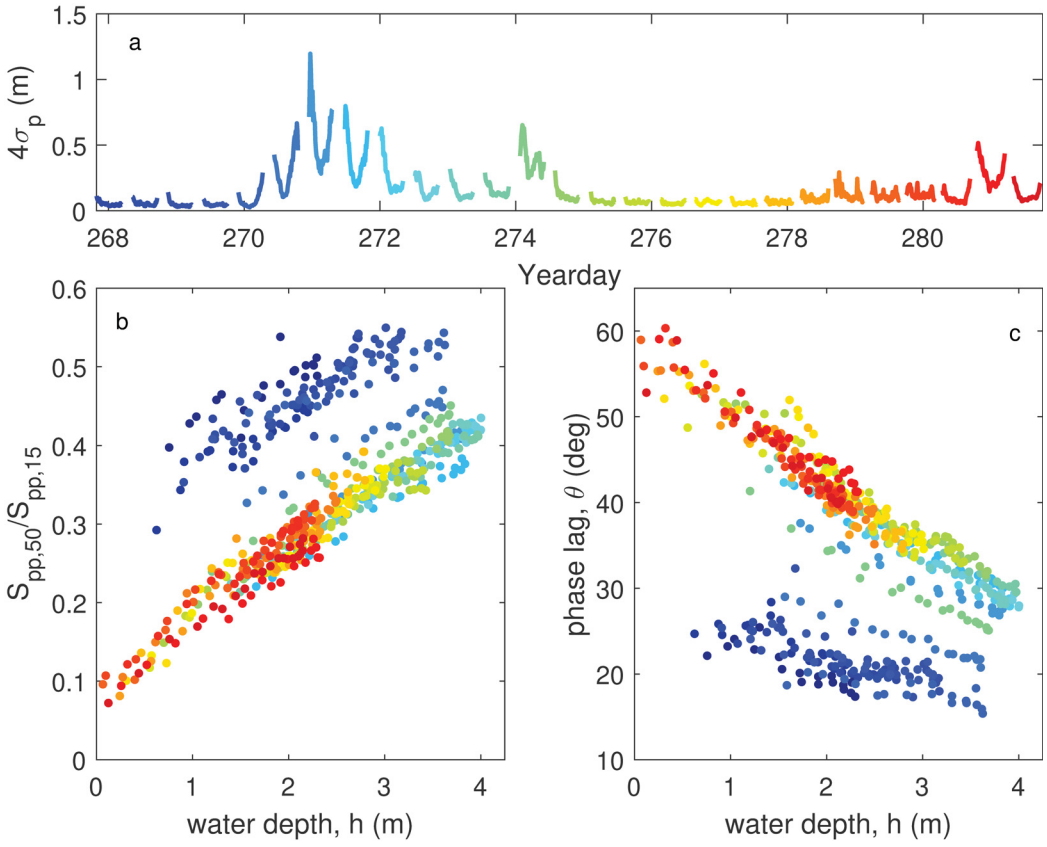

Figure 4.9: (a) Time series of significant wave height, $4\sigma_p$, (b) pore pressure variance ratio, and (c) phase lag at $z = 50$ cm relative to $z = 15$ cm and $f = 0.1$ Hz, plotted versus mean local water depth h. Warmer colors denote later times. Attenuation and phase are maximal as h approaches zero. Note the pronounced increases in attenuation and phase lag following the peak wave forcing associated with the first storm (second tide of yearday 270). Though the pressure sensor responsible for producing the data in (a) did not begin sampling until late in yearday 267, (b) and (c) include data from yearday 266 onward (darkest blue).

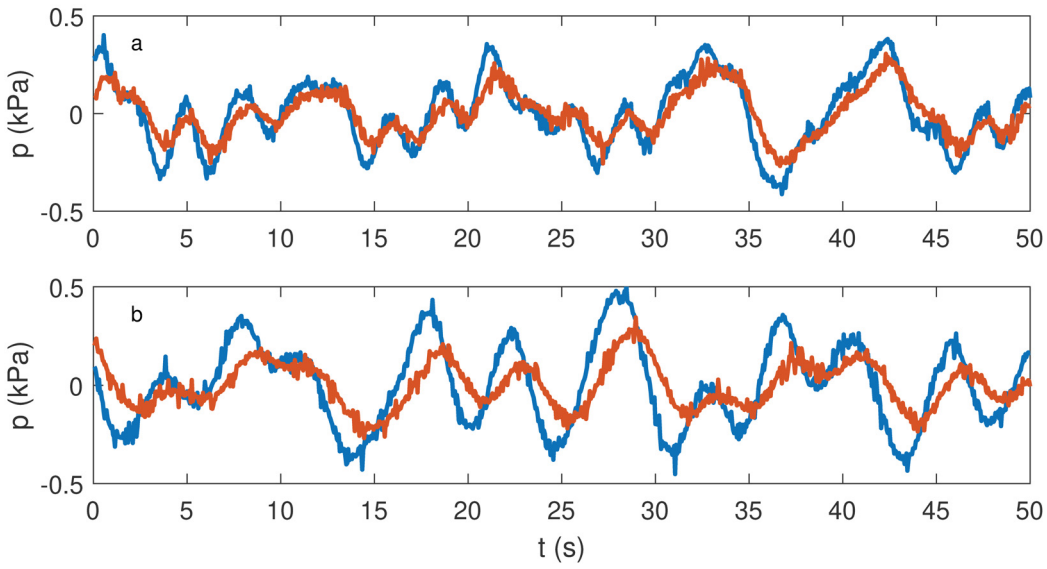

Figure 4.10: The oscillatory components of pore pressure measured at 15 cm (blue) and 50 cm (red) sediment depth are plotted, corresponding to (a) the first tide of yearday 269, prior to the first storm event of the experiment, and (b) the second tide of yearday 276, following the storm event. Mean local water depth is 2 m in both cases. Increased attenuation and phase shifting of the pressure signal are evident in the latter.

An example is shown in Fig. 4.9, where the variance ratio and phase lag (at $f = 0.1$ Hz) associated with signals from the two pressure sensors that functioned for the full experiment (p_{50}, relative to p_{15}, spanning 35 cm of sediment) are plotted versus mean local water depth. At a given frequency, the pressure variance ratio decreases with decreasing water depth, corresponding to higher attenuation for shallower water. Correspondingly, the phase lag increases as water depth decreases, so the phase lag is also higher for shallower water.

A marked change in the relationship is seen to have occurred early in the experiment, in the form of a pronounced increase in both attenuation and phase lag of the pore-pressure signal during the second tide of yearday 270, relative to observations from the five preceding days. At 2 m water depth, for example, the average pore pressure variance ratio decreased from approximately 0.50 to 0.25, and the average phase increased from about 20 degrees to more than 40 degrees. These factor of two changes coincided with the arrival of a strong southwest wind event accompanied by 0.5 to 1 m significant wave heights. It is thought that the low wave energy conditions during the five days prior to this wave event were insufficient to re-consolidate the beach material disturbed during instrument

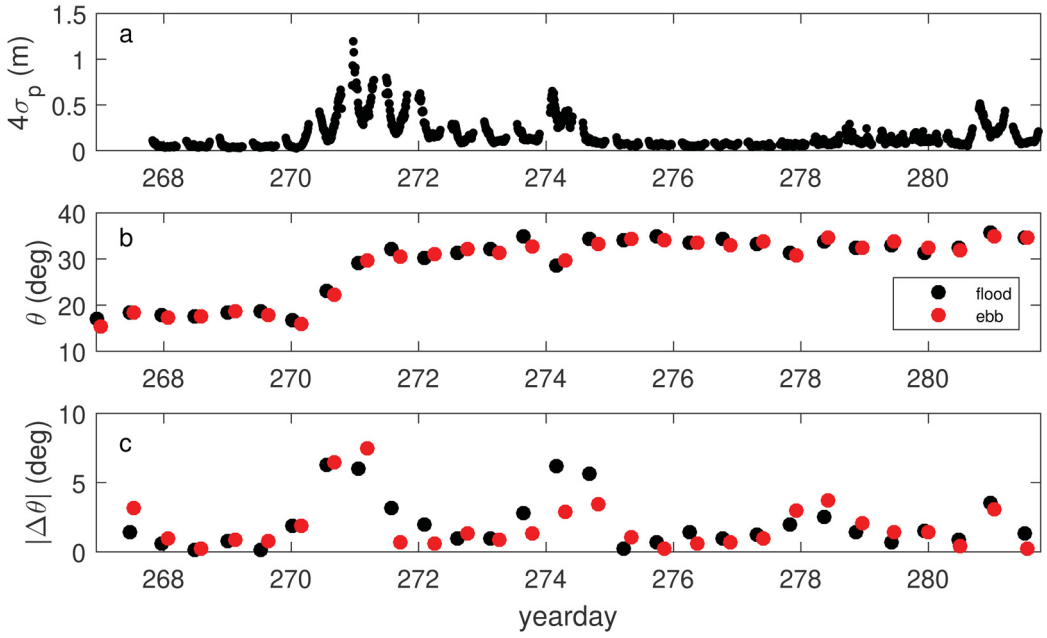

Figure 4.11: Significant wave height, $4\sigma_p$, (a) is shown to correspond well with changes in phase lag (b and c) during the experiment for fixed frequency ($f = 0.1$ Hz), sediment depth (50 cm relative to 15 cm sediment depth), and water depth ($h = 2$ m). $|\Delta\theta|$ (c) denotes the magnitude of difference in phase lag between successive tides, computed as the difference in phase lag on a flood (ebb) tide from the previous flood (ebb) tide. Though the pressure sensor responsible for producing the data in (a) did not begin sampling until late in yearday 267, (b) and (c) include data from the end of yearday 266 onward.

burial. In Fig. 4.10, time series recorded at 15 and 50 cm sediment depth are compared for periods before and after the storm event, with increased signal attenuation and phase lag evident in the latter. Additional variability corresponding to later wave events is reflected by the magnitude of difference in phase lag between successive tides, $|\Delta\theta|$, shown to vary in proportion to the significant wave height, $4\sigma_p$, in Fig. 4.11. These findings are discussed further in Section 4.5.2.

In Fig. 4.12, the pore pressure variance ratio and phase lag are plotted versus mean local water depth for three different frequencies, with the observations prior to the wind/wave event on yeardays 270-271 omitted. Thus, the effects of sediment disturbance due to instrument burial are not included, and the pore pressure transmission properties of the typical beach state are represented. The relationship between water depth and both the pore pressure variance ratio and phase lag is nearly linear over the observed range of water depths. Frequency dependence is also evident in both cases.

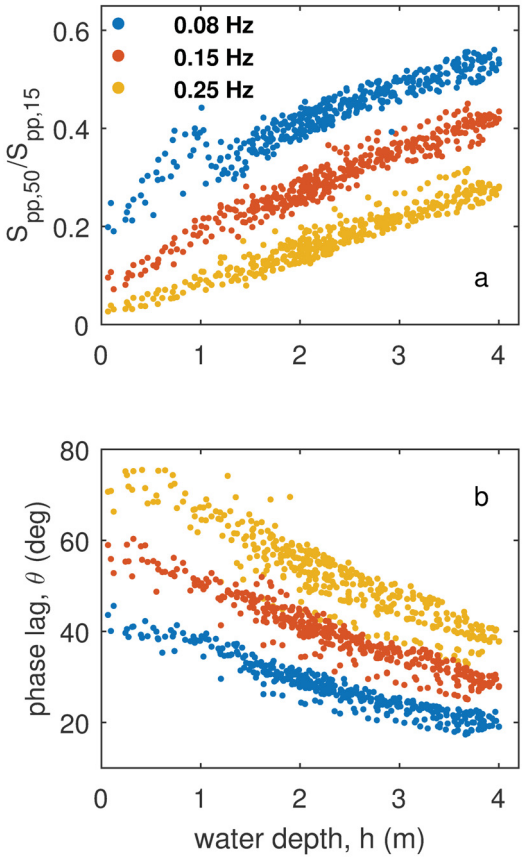

Figure 4.12: Pressure variance ratio (a) and phase lag (b) between the pressure sensors at z = 15 cm and z = 50 cm for three frequencies, plotted versus mean local water depth for the period after yearday 271 (see Fig. 4.9). Frequency dependence is evident, with lower frequencies exhibiting smaller phase shifts and lower attenuation.

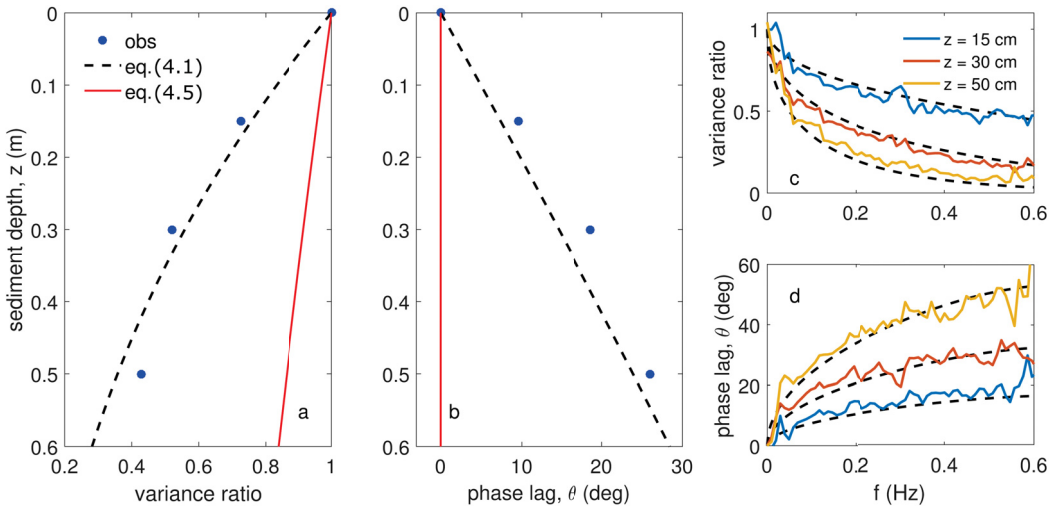

Figure 4.13: Observed and model-predicted pore pressure attenuation and phase at 0.1 Hz and 1.8 m water depth versus sediment depth [(a), (b)] and frequency [(c), (d)], with $S(z = 0) \simeq 0.9$ and $k_c = 7.6 \times 10^{-4}$ m s^{-1}. The observations correspond to the last tide of yearday 266, when all 4 sensors in the vertical array were working.

4.4.2 Comparisons to the *Yamamoto et al.* Model

Predictions of pore pressure attenuation and phase versus both sediment depth and frequency from the full analytical solution (4.1) are compared in Fig. 4.13 to observations from the full vertical array for the second tide of yearday 266. The observed values were computed for consecutive 12 minute segments of pressure data in order to account for the rapid variation in mean water level. The depth averaged values of $n = 0.22$ (± 0.05 standard deviation) and $k_c = 7.6 \times 10^{-4}$ m s^{-1} ($\pm 1.7 \times 10^{-4}$ m s^{-1} standard deviation), were used as model input. Poisson's ratio ν and the shear modulus G were set at 0.3 and 4×10^8 Pa, respectively, typical values for a sand and gravel mixture. The degree of saturation S (varying with z according to the isothermal ideal gas law), was adjusted to minimise the least-squares error between the predictions and observations. The best-fit values of S ranged from 0.85–0.90 in 1–2 m of water depth, yielding values for the stiffness product $G\beta'$ between 320 at $h = 2.1$ m, $z = 0.5$ m and 520 at $h = 0.1$ m, $z = 0$ m. Recall from Section 4.2 that when $G\beta' >> 0$, the relative stiffness of the porous matrix exceeds that of the pore fluid, and the mechanical properties of the soil must be considered.

The model predicts the observations well both with sediment depth and frequency, with a relative RMS error generally less than 10%. The $m = 0$ limit (4.5) accounts for only about 20% of the observed variance attenuation with sediment depth for the case shown

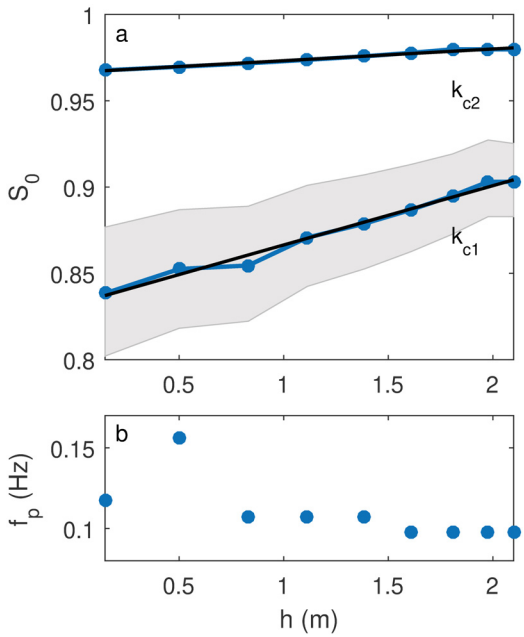

Figure 4.14: (a) Best-fit model-predicted estimates of the percent saturation S_0 at z = 0 versus water depth h, for the measured hydraulic conductivity value, k_{c1} = 7.6×10^{-4} m s^{-1}, with uncertainty region computed using k_{c1} ±1 standard deviation, and lower value, k_{c2} = 1.5×10^{-4} m s^{-1}. Linear regressions are shown in black. (b) Peak incident wave frequency, f_p, used for the best-fit calculation, observed at the array on yearday 266. The available data are limited to flood tide of yearday 266. The data points are 12 min apart.

in Fig. 4.13a, and, as expected, predicts zero phase lag with sediment depth (Fig. 4.13b), quite unlike the observations. The frequency dependence of the pore pressure variance ratio and phase at each sediment depth, relative to the pressure at the bed, is shown in Figs. 4.13c and d. The observed and model-predicted pressure ratio and phase exhibit very similar dependencies on forcing frequency and sediment depth.

Best fit saturation values are plotted in Fig. 4.14 together with the forcing frequencies – the peak frequency in the pressure spectrum for each data run – used in the calculations. The saturation values shown are the best fit values at the bed surface ($z = 0$), given by S_0, and are shown to increase linearly with increasing water depth. To demonstrate the sensitivity of the best fit value of S_0 to our choice of k_c, model predictions are shown using two different values of k_c: the measured, depth-averaged value ($k_{c1} = 7.6 \times 10^{-4}$ m s^{-1}), for which the computed standard deviation allowed a quantification of uncertainty in S_0, and a reduced value ($k_{c2} = 1.5 \times 10^{-4}$ m s^{-1}). The lower value yielded $O(10\%)$ higher saturations. With the decay scale $\tilde{k}'$ fixed by the observations, a continuum of best-fit

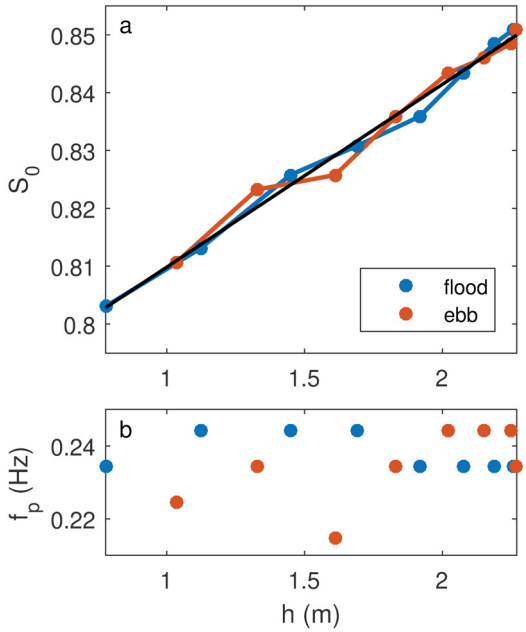

Figure 4.15: (a) Best-fit model-predicted estimates of the saturation S_0 at z = 0 versus water depth h from the flood tide (blue) and ebb tide (red) of an earlier test deployment (yearday 185), with k_c = 1.5×10^{-4} m s^{-1}. A linear regression is shown in black. (b) Peak incident wave frequency, f_p, used for the best-fit calculation, observed at the array on during a previous test deployment (yearday 185). Limited knowledge of sediment mechanical parameter values for the test deployment make the reported saturation values themselves unreliable, however the approximately symmetric relationship about high tide is the result of interest from the yearday 185 test. The data points are 12 min apart.

solutions can be obtained, depending on the set value of k_c. It is true in general that for fixed $|\tilde{k}'|$ (and therefore a), when k_c is decreased, S must increase (see Appendix A).

Observations are only available from the flood tide on yearday 266. However, we had carried out a test deployment several months earlier (yearday 185) with three sensors buried at 0, 25, and 50 cm sediment depth in order to test whether interstitial air might affect pore pressure at surface gravity wave frequencies in this environment. The results from this test are plotted in Fig. 4.15, and are relevant here because the data span both flood and ebb. Fig. 4.15 includes an equivalent best-fit model analysis of the yearday 185 dataset using the same parameter values, and $k_c = k_{c2}$ (the lower value of the two stated above). We note that the choice of k_c is arbitrary with respect to these data, as no observations of soil properties are available. However, the important result is that the best fit values for S_0 increase and decrease symmetrically about high tide – indicating that

air present in the pore spaces was not released with either the rising or falling tide. Also apparent from Fig. 4.15 is that the change in best-fit value of S with h is independent of the time rate of change of h. This is important because, as both Figs. 4.14 and 4.15 indicate, the rate of change of h is very high – about 3 m hr^{-1} at mid-tide – and decreases as the tide advances to values approaching zero at high tide. The linearity of the observed response persists throughout, however, indicating that the assumption of stationarity in the model – i.e., constant absolute pore water pressure, $P(z)$ – is not violated despite the very rapid changes in water level at mid-tide.

4.5 Discussion

4.5.1 Comparison to Previous Results

Few studies have reported wave-resolved pore pressure measurements in a natural beach setting, especially with regard to the vertical structure of phase. In the only other field study to use a vertical array of buried pressure sensors to estimate characteristics of the surface wave field of which the authors are aware, *Raubenheimer et al.* (1998) found that the mechanical properties of the sediment-water matrix were unimportant. The implication is that air inclusions were not present in the sediment at their sites: two gently sloping (roughly 1:30 slope) fine sand beaches with tidal ranges of 2-2.5 m. *Michallet et al.* (2009) (see also *Bonjean et al.*, 2004; *Mory et al.*, 2007) observed pore pressure attenuation and phase shifting in medium sand in the intertidal zone of a macrotidal beach (4 m tidal range, roughly 1:16 slope), which they attributed to interstitial air inclusions, based on comparisons to the *Sakai et al.* (1992) model and supported by direct observations of pore-trapped air using a geoendoscopic camera (described by *Breul and Gourvès*, 2008). The work of *Michallet et al.* (2009) is the only other study – that we have been able to find in the literature – of field observations of vertical changes in pore pressure phase at surface gravity wave frequencies in a nearshore setting. However, their measurements were made on the face of a several-metre wide, partially buried, concrete World War II bunker. How the presence of this structure might have affected the measurements is not known.

Though the sensitivity of pore pressure attenuation and phase to wave activity was also noted by *Michallet et al.* (2009), their results indicated a clear relationship between significant wave height and spectral ratio, with larger wave heights corresponding to larger observed spectral ratios (i.e., lesser attenuation), the implication being that bed erosion

associated with heightened wave activity allowed pore-trapped air to escape. With the exception of a single event (see Section 4.5.2), this finding is not apparent in our results. However, we acknowledge that our observations, made at depths of 15 and 50 cm in the sediment, do not take into account the uppermost 15 cm of the sediment column.

The findings of *Michallet et al.* (2009) indicated that the distribution of trapped air with depth in the sediment was not homogeneous, with saturation values nearing 1 both in the upper 10 cm of the sediment column and below 45 cm, with a saturation minimum at approximately 25 cm of sediment depth. The model-predicted pressure variance ratios and phase lags with sediment depth fit our observations remarkably well (see Fig. 4.13), given our assumption of isotropic saturation by an isothermal ideal gas, indicating that the distribution of trapped air in the bed was approximately uniform. The difference between our results and those presented by *Michallet et al.* (2009) could be due to a combination of factors, including the differing grain sizes and distributions, proximity to a coastal structure, and/or proximity to the fixed minimum height of the water table, below which saturation S might be assumed to be 1. In both cases, tidal range appears to be a key component influencing the presence of air in pore spaces.

4.5.2 Sensitivity to k_c and Sediment Disturbance

The modeled pore pressure attenuation and phase were found to be most sensitive to the values of saturation, S, and the hydraulic conductivity, k_c, a result consistent with previous investigations. Varying G within the range of realistic values for a sand-gravel mixture was found to have negligible effect on model output. The influence of n and ν was also found to be negligible. The best-fit saturation values reported here, ranging from 0.85 to 0.90 with increasing water depth, are sensitive to the choice of k_c. Thus, any error associated with the variability of k_c is also present in the estimation of S. It is well known (*Baird et al.*, 1997; *Horn et al.*, 1998) that significant variability can occur in measured values of permeability for a given sample, owing to variations in particle arrangement and the degree of consolidation. The effect of varying k_c on our S estimate was approximately 10:1 in the neighbourhood of our best-fit solution. For example, to change the saturation value at the bed surface in 2 m water depth from 0.90 to 0.98 (a saturation estimate reported by *Yamamoto et al.* (1978) for their laboratory experiments), k_c must take on a value of 1.5×10^{-4} m s^{-1}, a decrease of 80% from the measured, depth averaged value. As shown in Appendix A (equation (A.9)), it is true in general that an increase in S must be coupled

with a decrease in k_c when the amplitude decay scale with sediment depth is fixed by the observations.

Between yeardays 270 and 272, the relationship between pore pressure transmission properties and mean water depth changed markedly. For example, the pore pressure spectral ratio computed between signals recorded at 15 and 50 cm sediment depth, 0.1 Hz, and 2 m mean water depth, decreased from approximately 0.55 to 0.35, and the phase lag, θ, was effectively doubled from approximately 15 to 30 degrees. We interpret this phase lag increase to be the result of wave-forced changes in the hydraulic conductivity, k_c, of the sediments surrounding the vertical array, in turn affecting the ability of the sediment to retain air (and thereby decrease the saturation). Decreasing k_c increases the model-predicted values of both pore pressure attenuation and phase lag with sediment depth. As a limiting case (i.e., for fixed S, k_c variable), for $S(z = 0)$ fixed at 0.90, the observed doubling of phase lags can be accounted for in the model by decreasing k_c from 7.6×10^{-4} to 1.9×10^{-4} m s^{-1} – a reduction of 75%.

Following the installment of the array in the beach, care was taken in refilling the instrument burial pit (with approximate diameter and depth of 0.75 m) to return sediments to the approximate depths from which they were removed, and compaction was attempted by foot-packing the reintroduced material surrounding the array. However, the disturbance of the sediment associated with burying the array led to a reduced level of compaction and increased hydraulic conductivity – a state which persisted until the arrival of the first storm event of yearday 270. The preceding discussion suggests that wave action during the storm event reduced the hydraulic conductivity of sediments that had been shoveled back into the instrument burial pit, either by compaction or possibly through the settling/transport of fine-grained particles into pore spaces, thus decreasing the hydraulic conductivity. Before this point, we note that the pore pressure phase and attenuation properties appear consistent between tides, and, from our yearday 185 result (Fig. 4.15), there is little discernible difference in the best fit saturations during ebb tide compared to the immediately preceding flood. Thus, the hydrostatic pressure cycling associated with the tide alone, and the pore water infiltration/exfiltration cycling with the tide, appear to change neither the trapped air content, nor the permeability (via compaction) of the sediment significantly.

Instrument burial has significant effects on pore pressure amplitude and phase. *Bonjean et al.* (2004), based on dynamic penetrometer resistance profiles at the same location for

successive tides following instrument installation in a medium sand bed, concluded that a duration of two tides was sufficient to regain a level of sediment compaction similar to undisturbed sediment. It is apparent in the present case that the sediment remained loosely packed for much longer (seven tides, spanning four days, represented in Figs. 4.9 and 4.11), and that the mean hydrostatic pressure levels associated with the tides are largely irrelevant to the process. Thus, the effects of sediment disturbance due to instrument burial may persist for periods lasting days to weeks at this site, depending on wave conditions. Given these findings, it is likely that the observed spectral ratios on yearday 266 (Fig. 4.13) prior to the first storm event, when all four sensors were operational, are overestimated, and the phase lags underestimated, relative to what might be considered a 'typical' beach state.

In addition to the large change in pore pressure transmission properties accompanying adjustment to the first wave event, restructuring of the sediment associated with subsequent wave events led to further variation in attenuation and phase properties, as shown by the correspondence between the significant wave height, $4\sigma_p$, and the magnitude of difference in phase lag between successive tides, $|\Delta\theta|$, in respective Figs. 4.11a and c. However, unlike the first wave event, changes to pore pressure transmission did not persist in the cases of the subsequent wave events, but rather returned to the apparent equilibrium that prevailed from yearday 271 onward (e.g. Fig. 4.11b). The magnitude of changes in attenuation and phase in these cases, along with the associated significant wave heights, were also smaller. During the second wave event, on yearday 274, the phase lag is observed to have decreased. Of the three wave events identified during the experiment (i.e., yeardays 270-271, 274, and 281), this is the only instance that a decrease in phase lag occurred, and may indicate that air was released from the sediments around the array due to disturbance of the beach surface by wave action, as *Michallet et al.* (2009) inferred from their results. There was a positive change in the observed phase lag associated with the third wave event on yearday 281. However, the magnitude of change in this case was the smallest of the three events, and corresponded to the smallest significant wave heights.

Variations in bed level at the array location were not quantified during the experiment, though the cross-shore low-tide bed profile was observed to be very stable, in general not changing by more than a few cm from tide to tide with respect to the visible uppermost array sensor. However, the subaqueous bed profile has been observed (*Hay et al.*, 2014)

to change during storm events with the emergence of wave orbital-scale ripples of $O(1$ m$)$ wavelength. The effects of varied bed level on the pore pressure response and model predictions have been investigated assuming a maximum bed level change of $\pm$5 cm. With parameter values set to be representative of Advocate Beach sediments and $S_0 = 0.90$, the predicted phase lag between sensors at $z = 15$ cm and $z = 50$ cm depth for incident waves of 0.1 Hz would be expected to change by $\pm$0.8 to 1.2% in water depths of 0.1 to 2.1 m. This change is small, as expected, owing to the approximate linearity of phase lag with sediment depth. Similarly, the expected change in pressure variance ratio would be $\pm$7.8 to 10.5% in 0.1 to 2.1 m water depth. A 5 cm change in bed level would be expected to alter our best fit S estimate by $\pm$0.04 in 2.1 m water depth. Owing to the low energy wave conditions on yearday 266, it is expected that the variation in the bed elevation at the array location would have been negligible.

4.5.3 Anisotropy

The model developed by *Yamamoto et al.* (1978), though shown in this and previous studies to accurately (relative RMSE < 0.1, in this case) reflect observed values, does involve a number of simplifying assumptions. An important potential source of error is the assumption of isotropy of the medium. The depth dependent structure of porosity and hydraulic conductivity shown in Fig. 4.5 clearly demonstrates that Advocate Beach sediments are anisotropic in the vertical. A more accurate assumption would be one of two-dimensional isotropy (i.e., to account for variations with depth alone). However, for the purposes of this study – i.e., demonstrating the likelihood that the observed dependence of pore pressure amplitude and phase on sediment depth can be attributed to included air – the assumption of isotropy and the use of depth-averaged soil parameter values are justified.

Grain shape may also play an important role with respect to variable permeability in this setting. The characteristic sediment types at Advocate Beach include a dominant proportion of flat, oval-shaped shale grains, along with more spherical feldspar-based grains, particularly in the sand and fine gravel size fractions. *Stark et al.* (2014) proposed that preferential arrangement of plate-like particles from the same study site led to the observed increase of internal friction angles. Preferential particle arrangement could contribute to the observed variations in hydraulic conductivity and porosity with sediment depth.

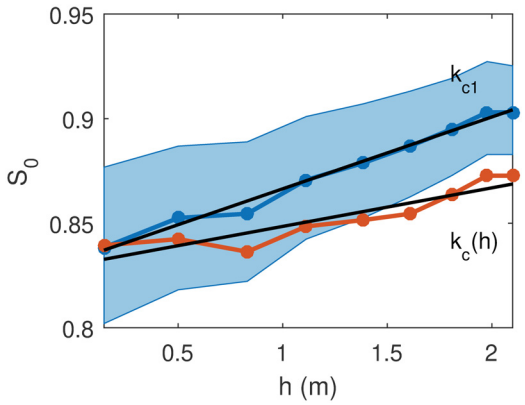

Figure 4.16: Best-fit model-predicted estimates of the saturation S_0 at $z = 0$ versus water depth h for fixed $k_c = k_{c1}$ (blue), the measured, depth-averaged value, with an uncertainty region computed using $k_{c1} \pm 1$ standard deviation, and variable $k_c = k_c(h)$ (red). Linear regressions are shown in black. The range of S_0 estimates made using $k_c(h)$ is in agreement with the prediction made assuming hydrostatic compression of an isothermal ideal gas. The available data are limited to flood tide of yearday 266. The data points are 12 min apart.

Direct measurements of saturation have not been made. Video endoscopy allows the direct measurement of "surfacic air content" – i.e., the fractional surface area occupied by bubbles in a 2-d image. The relationship between surfacic air content and volumetric air content is nontrivial. In a first approximation, *Breul and Gourvès* (2008) estimated volumetric air content to be equivalent to one third of the surfacic air content using geometric arguments, and taking into account edge effects and the flattening of bubbles against the apparatus. Using this technique, *Bonjean et al.* (2004) observed a sediment depth-dependent distribution of surfacic air content with a maximum of 6% observed near 25 cm sediment depth in medium sand. *Breul and Gourvès* (2008) reported similarly shaped distributions with a maximum surfacic air content of 16% using the same apparatus, in the same location, at different times. The direct observation of pore-trapped gas in such quantities, considered in tandem with the large tidal range at Advocate Beach (and the associated twice daily drainage of water from, and concurrent re-aeration of, the beach face sediments), lends justification to the values reported here.

4.5.4 Hydraulic Conductivity vs. Saturation and Water Depth

The slope, dS/dh, in Fig. 4.14, is 0.007 m^{-1} for k_{c2} and 0.034 m^{-1} for k_{c1}, both less than the respective predictions of 0.003 m^{-1} and 0.016 m^{-1} based on hydrostatic compression of

free air. The discrepancy persists regardless of the choice of k_c. The best-fit and predicted slopes can be brought into agreement only when the k_c estimate is allowed to vary with h. In Fig. 4.16, the best-fit values, S_0, for k_c set as the measured, depth-averaged value (k_{c1}, as shown in Fig. 4.14) are compared with S_0 estimates for k_c values that increase with increasing h. For this case, the initial k_c value (corresponding to a mean water depth of 0.145 m) was set as k_{c1}, then increased in proportion to the change in h, giving the relation

$$k_c(h) = Ak_{c1}h + B, \tag{4.8}$$

with A = 1/5 and B = 7.33$\times 10^{-4}$, for a total increase in k_c of 39% over the observed range of h. The slope of a linear regression of the associated best-fit S_0 values with mean water depth is in agreement with the prediction made on the basis of hydrostatic compression of free air in this case. Combining equation (4.8) with the equation of the linear regression yields an equation for $k_c(S)$ which is linear, with k_c values that increase with increasing S. The dependence of hydraulic conductivity on soil saturation is well documented in the soil mechanics literature, and closed form solutions have been obtained: e.g., *van Genuchten* (1980) equation (8), designated vG8 here. Although vG8 is highly nonlinear, the predicted relationship is consistent with the sign and magnitude of change in k_c with S for the range of values of S in Fig. 4.16. However, because the vG8 relation involves an exponent which must be determined empirically, and depends upon the residual saturation – which we did not measure – a quantitative comparison to the van Genuchten model is not carried out here.

In physical terms, an increase in k_c with increasing water depth can be attributed to a reduction in trapped air volume because of the higher hydrostatic pressure, and therefore an increase in the pore space available for water to flow.

4.6 Summary and Conclusions

New observations have been presented of the vertical structure of pore pressure phase and attenuation in the surface gravity wave band on a natural, megatidal, mixed sand-gravel-cobble beach. The data indicate significant attenuation and phase shifting within the upper 50 cm of the sediment column.

The observations are compared to the analytic poro-elastic bed response model formulated by *Yamamoto et al.* (1978). Good agreement (relative RMSE less than 10%) is obtained between observed and modeled pressure phase and attenuation profiles versus sediment burial depth and forcing frequency. Consistent with the existing literature, the predictions are most sensitive to the effective compressibility of the pore fluid β' – determined by the degree of pore-fluid saturation S – and (though to a lesser degree) the hydraulic conductivity k_c. In order to reproduce the observed phase lag between the pore pressure at depth within the sediment and the pressure at the sediment-water interface, it was necessary to adjust the value of S, i.e., to include interstitial trapped air. Using the observed values of k_c – measured in the laboratory using (highly disturbed) samples of the beach face sediments – best-fit saturation values ranged from 85% to 90% depending on water depth. The model/data comparison indicates that oscillatory pore pressures at frequencies of 0.1 Hz and higher were confined to sediment depths less than *ca*. 1 m.

Pore pressure phase-shifting and attenuation are both found to be pronounced over the 0.5 m sediment depth range of the buried sensors. Observed values were sensitive to tidal changes in mean water depth h, with phase shifting and attenuation decreasing as h increased, qualitatively consistent with reduced volume of entrapped air in response to increased absolute ambient pressure. Agreement between changes in best-fit saturation values with water depth and changes predicted by isothermal ideal gas compression are in quantitative agreement only when the hydraulic conductivity is allowed to increase with increasing water depth.

Sensitivity to redistribution of beach material within the upper 50 cm of the sediment column by wave action is strongly indicated. The largest changes occurred with the onset of the first storm event, following a five day period of calm conditions. It is suggested that the limited wind and wave activity following instrument burial was insufficient to reconsolidate the beach material to a typical state, resulting in increased hydraulic conductivity, and decreased phase-shifting and attenuation of pore pressure signals. Additional, though less pronounced, variability was observed during later energetic wave events.

The following conclusions are drawn: (1) Pore-trapped air plays a key role in the dynamics of pressure transmission through the sediment column at Advocate Beach. (2) Changes in pore pressure transmission properties are driven by changes in the hydraulic conductivity of the beach face sediments associated with energetic wave events. (3)

Hydrostatic pressure alone does not serve to restore disturbed steep beach sediments to equilibrium, at least not on time scales of *ca*. 1 week. Disturbance of beach material associated with instrument burial can therefore affect measured pore pressure values on time scales of days to weeks in the absence of energetic wave events. (4) Rapid attenuation attributed to the presence of pore-trapped air limits the effects of cyclic pressure loading by wave action to a region near the bed surface. (5) Symmetry of best-fit saturation estimates (in one case) and of phase estimates (in general) about high tide, indicates that air escapement did not generally occur between 15 cm and 50 cm sediment depth, over a tidal cycle. (6) Because of the presence of trapped air, the associated phase shift, and the possible changes in burial depth associated with active transport conditions, buried pressure sensors deployed in the intertidal zone of MSG beaches for the purpose of wave measurement should be ported to the sediment-water interface. Otherwise, multi-sensor, coherent vertical arrays are required to remove the effects of the sediment on the pressure signal, and therefore infer the kinematic properties of surface gravity waves on MSG beaches.

Future work could attempt to draw a connection between depths of beach disturbance by wave action and pore-pressure profiles, and examine the effects of particle shape, and (vertical) anisotropy of sediment properties. While including the effect of air bubbles on the bulk compressibility of the sediment column does bring the data and model predictions into satisfactory agreement, $O(10\%)$ by volume of air is required. It seems likely that such high concentrations of included air should influence infiltration/exfiltration processes and sediment stability at Advocate Beach. Similar investigations at other steep mixed sand and gravel beach sites with high tidal ranges would therefore be of interest.

CHAPTER 5

TIMESCALES OF BEACH CUSP EVOLUTION ON A STEEP, MEGATIDAL, MIXED SAND-GRAVEL BEACH

This chapter was first published in *Marine Geology*[1].

5.1 Introduction

Beach cusps are spatially periodic sedimentary features common on beach foreshores. They consist of seaward-pointing sequences of ridges (horns), separated by topographic depressions (embayments), with quasi-regular spacings varying from $O(10^{-1})$ to $O(10^{2})$ m (*Coco et al.*, 1999). Cusps are generally acknowledged to be swash-generated features, though recent studies have drawn a distinction between beach cusps of short wavelength (< 20 m), and the longer-wavelength large beach cusps (LBC) which may be tied to surf- as well as swash-zone morphodynamic processes due to their larger cross-shore extent (*Garnier et al.*, 2010). Cusps have been observed to form under a wide range of conditions and beach types, though are acknowledged to form most readily during low energy, shore-normal incident wave forcing on reflective, medium- to coarse-grained beaches (*Holland*, 1998).

Despite their long history of study, focus on beach cusps has generally been limited to beaches comprised of a single sediment type (i.e., sand or gravel), with little emphasis on beaches composed of mixed sand and gravel (MSG). *Nolan et al.* (1999) presented the only

[1] **Guest, T. B.**, and A. E. Hay, Timescales of beach cusp evolution on a steep, megatidal, mixed sand-gravel beach, *Marine Geology*, 416, 105984, 2019.

study we are aware of from the last 20 years treating mixed sand-gravel cusps specifically. Their focus was on cusp morphometry. The dynamics of the formation process were not investigated.

Sediment dynamics on MSG beaches in general are less well studied than sand or gravel beaches, but have received increased attention in recent years owing to the increased use of sand and gravel mixtures in coastal engineering schemes, e.g., involving beach replenishment (*Mason and Coates*, 2001). Also, the relative efficiency of gravel, cobble, and mixed beaches for dissipating wave energy provides a natural form of coastal defence.

The tendency for different sediment grain sizes and types on mixed beaches to self-segregate under some conditions is also of great interest, and has recently garnered attention in the context of other nearshore bedforms and processes (e.g., *Murray and Thieler*, 2004; *Van Oyen et al.*, 2010; *Hay et al.*, 2014). Beach cusps are perhaps the most widely recognisable feature demonstrating size-segregation in the nearshore, having long been associated with grain size sorting between bays and horns (e.g., *Longuet-Higgins and Parkin*, 1962).

The modern (*ca*. 1970s to present) cusp literature has been largely focused on understanding the mechanism(s) responsible for cusp formation and establishing predictive relationships between cusp spacing and hydrodynamic forcing. Efforts to establish predictive relationships between cusp spacing and the wave forcing were initially based on the concept of a hydrodynamic template, provided by standing low mode subharmonic or synchronous edge waves, whose spatial structure would become imprinted on the underlying sediment (*Guza and Inman*, 1975; *Guza and Bowen*, 1981; *Holman and Bowen*, 1982). Later models are based on free, self-organising behaviour, characterised by asymmetric feedbacks between hydrodynamics and morphology (*Werner and Fink*, 1993; *Coco et al.*, 2000, 2004; *Sunamura*, 2004; *Dodd et al.*, 2008). Though both types of theory have been used to predict the spacing of beach cusps with reasonable skill in some circumstances (*Coco et al.*, 1999), the self-organisation mechanism has been found to be more widely applicable (*Coco and Murray*, 2007).

Focus on cusp initiation mechanisms and predictors of spacing has given way in the last decade to renewed emphasis on cusp morphology and characterisation of dynamics (e.g., *Almar et al.*, 2008; *van Gaalen et al.*, 2011; *Vousdoukas*, 2012; *Poate et al.*, 2014). However, uncertainties remain about the nature of beach cusp morphological evolution.

These include: varied and, in some cases, inconsistent conclusions regarding factors influencing cusp evolution timescales; the importance and/or role of grain size sorting; and a lack of consensus on the roles of accretion and erosion.

There has been little emphasis on cusp formation timescale. The data indicate that beach cusp lengthscale and formation time are related. The observations by *Komar* (1973) of beach cusps on a sandy lake shore often provide a lower limiting case in the literature for both cusp spacing and formation time – as short as 11 cm and 10 mins, respectively. However, these observations are largely qualitative, and do not document the morphodynamic evolution of the cusp fields. *Longuet-Higgins and Parkin* (1962) reported similarly short formation timescales from a wave tank experiment, in which 1.5 s waves of < 2 cm height led to the onset of cusp formation (mean wavelength of *ca*. 50 cm) in fine sand within a few minutes. Cusp formation in the field is generally reported to occur over much longer timescales – on the order of tidal time (hours to days) rather than minutes. *Holland* (1998), reporting on 57 cusp events spanning nearly a decade, observed that the transition from indistinguishable to well-formed cusps on a medium sand beach generally occurred over three consecutive days, with no indication of well-developed cusps forming in less than a few hours. The mean cusp wavelength was 25 m. *Poate et al.* (2014) reported 25 m wavelength cusp formation on a high-energy, pure gravel beach occurring in under 12 hours. *Garnier et al.* (2010) established formation timescales for large beach cusps (*ca*. 30 m wavelength) on a medium-coarse sand beach that depended upon the forcing energy. Their shortest reported formation times (3-6 hours) occurred when offshore wave heights exceeded 2.5 m, 9-12 hours for wave heights between 1.5 and 2.5 m, and 2-3 days for wave heights less than 1.5 m. Model results from *Dodd et al.* (2008) indicated a dependence of cusp growth rate on incident wave period, with growth rates increasing as period decreased.

The relationship between timescale and beach composition is largely uninvestigated. Numerical modelling by both *Coco et al.* (2000) and *Dodd et al.* (2008) indicated a relationship between a dimensional transport constant in their sediment flux parameterisations and the number of swash cycles required for cusp formation. Fewer cycles were required when the transport constant was increased. As noted by *Dodd et al.* (2008), it is possible to approximate this constant as a function of D_{50} using the Van Rijn sediment transport equation. The implication is that cusps would form more rapidly on beaches with a larger

mean grain size. *Dodd et al.* (2008) also concluded from their model results that beach permeability favours cusp development by enhancing the feedback mechanism (i.e., infiltration through the horns decreases the backwash volume, therefore decreasing offshore transport). For the case of mixed sand and gravel beaches, the gradation of fine and coarse material between bays and horns would be expected to further enhance feedbacks by increasing the asymmetry between erosion/depositional processes in bays and horns. Indeed, *Longuet-Higgins and Parkin* (1962) concluded from field observations that cusps form most easily given a vertical stratification of material: coarse sediments sitting atop a well-mixed, "impermeable" layer are more readily mobilised due to the reduced fluid infiltration. The heaping of sediments atop the horns makes them more permeable than the thinner layer in the bays, and therefore less subject to erosion.

In their gravel beach review paper, *Buscombe and Masselink* (2006) emphasised the importance of sediment characteristics in gravel beach processes, suggesting that morphodynamics alone are an inadequate descriptor of process on gravel (including MSG) beaches. They suggested a morpho-sedimentary dynamics framework, in which properties of the grain-size distribution (e.g., spatial and temporal heterogeneity, sorting) exert a fundamental control on morphological evolution, for further research and discussion around gravel beach processes. The role of size sorting in the process of cusp formation was investigated by *van Gaalen et al.* (2011) for the case of a sandy, microtidal beach on the Atlantic coast of Florida. Using regular morphological observations from a terrestrial laser scanner and discrete surficial sediment sampling, they found no significant correlation between grain size and position between horn and embayment. This led them to suggest that horn coarsening and embayment fining occurs after cusp development, making them inherently different from other sorted bed forms whose formation depends on differential transport characteristics for different grain sizes. However, the sediment size distribution at their site was relatively narrow compared to MSG beaches, with typical grain sizes ranging from 0.17 to 0.35 mm: i.e., fine to medium sand.

Results regarding the relative importance of accretion and erosion are varied. Instances of cusps formation have been reported for conditions dominated by sediment accretion, erosion, or a combination of both (e.g., *Antia*, 1987; *Masselink et al.*, 1997; *Almar et al.*, 2008). In addition to their conclusions regarding size-sorting, *van Gaalen et al.* (2011) demonstrated that the accretive/erosive properties of cusps observed on a sandy,

microtidal beach were dependent upon the position of the cusps relative to larger-scale coastal morphology. The reader is referred to the van Gaalen et al. paper for a more complete review of past results treating cusp horn/bay sedimentation.

Video-based techniques are well-suited for observing short-term morphological change at the shoreline (e.g., *Holman and Stanley*, 2007). Video-based shoreline tracking has been employed to study beach cusps by *Holland and Holman* (1996), *Holland* (1998), *Sunamura and Aoki* (2000), *Almar et al.* (2008), *Garnier et al.* (2010), and *Vousdoukas* (2012). With the exception of *Sunamura and Aoki* (2000), all these studies were on sandy beaches. *Almar et al.* (2008) and *Vousdoukas* (2012) used shoreline tracking to characterise the evolution of cusp fields, and so are particularly relevant here. Both tracked daily changes in cusp horn positions over periods of months. *Sunamura and Aoki* (2000) used images from a suspended camera to chronicle the formation of beach cusps on a steep gravel beach. Video-based methods are especially appealing for gravel or mixed sand-gravel environments where energetic shorebreaks impose challenges to observation by limiting the utility of *in situ* instrumentation.

Here we present video-based observations from a mixed sand-gravel beach in Advocate, Nova Scotia, Canada (Fig. 5.1). The purposes of this paper are to investigate (1) the timescales of cusp evolution at Advocate Beach using high temporal resolution observations; and (2) the role of size-segregation in the cusp formation process on a mixed sand and gravel beach. The steep slope, large tide range, and very broad sediment size distribution at Advocate Beach enable closer investigation of processes influencing cusp evolution timescales, and the role of grain size sorting.

The paper is organised as follows: Regional context is provided in Section 5.2. Experimental setup and analysis methods are outlined in Section 5.3. Section 5.4 contains results, beginning with experiment scale forcing and response, followed by detailed summaries of individual cusp events, including the two events which were characterised by pronounced topographic relief, and a third event which fortuitously captured an instance of differing surficial sediment properties in the cross-shore, providing insights into the relationship between size distribution and cusp formation timescale. A discussion of the results is presented in Section 5.5, with particular emphasis on horn dynamics, and the influence of a wide grain size distribution on cusp evolution timescales.

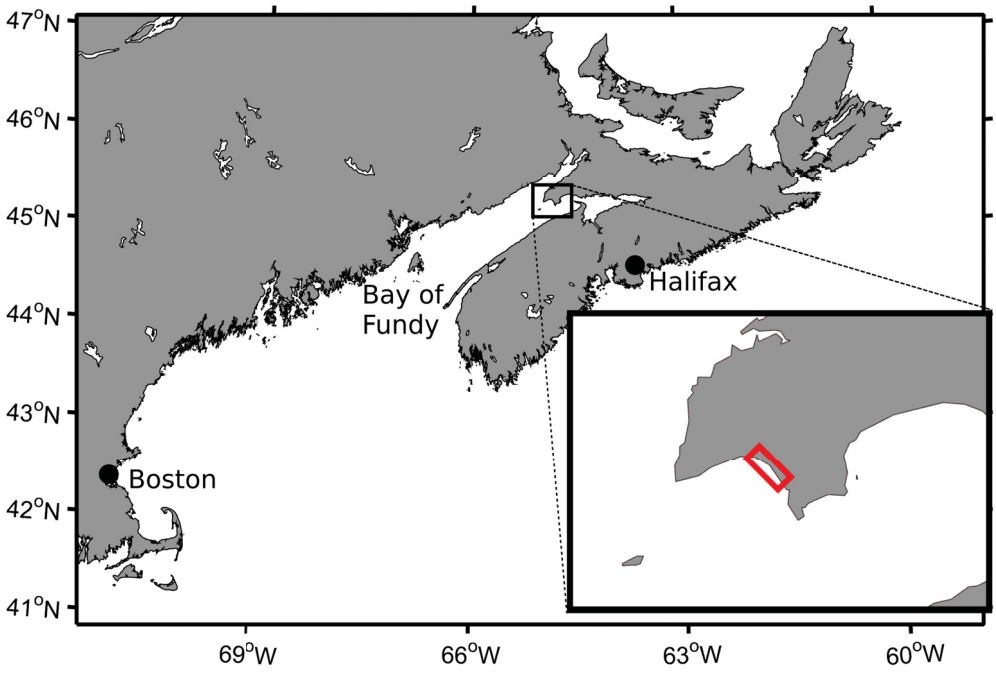

Figure 5.1: Map indicating the location of Advocate Beach (red box), Nova Scotia, Canada, near the head of the Bay of Fundy.

5.2 Regional Context

The study site is Advocate Beach, Nova Scotia (Fig. 5.1), a mixed sand-gravel barrier beach positioned near the head of the Bay of Fundy. It separates the headlands of Cape Chignecto to the west and Cape D'Or to the southeast, and is 5 km long with a nearly linear shoreline. The beach faces southwest, exposing it to the prevailing winds during summer months, as well as the direction of maximum fetch–roughly 500 km along the Bay of Fundy and into the adjacent Gulf of Maine. From the south and west-northwest, the beach is more fetch-limited.

Tides in the region are semidiurnal, and at Advocate Beach have a range of 8-12 m. According to *Levoy et al.* (2000), beaches with a tidal ranges in excess of 8 m may be classified as megatidal rather than macrotidal. The intertidal beachface has a uniform slope of roughly 1:10 that has persisted nearly unchanged through surveys conducted since the early 1980s (*Hay et al.*, 2014). During spring tides, the beach crest to low-water distance is approximately 100 m. The beach sediments range in size from medium sand to cobbles and boulders greater than 20 cm in diameter, generally well-mixed both across-shore and at depth. From the lower beach face to beneath lowest low water, the beach composition transitions to cobble and boulder-sized material, and the slope decreases substantially.

The wave climate at Advocate Beach is generally dominated by locally-generated wind waves. Peak wave periods during a 2-week experiment in spring 2012 ranged from 5 to 7 seconds (*Hay et al.*, 2014). During periods of weak local wind forcing, low-amplitude swell waves propagating from outside the Bay of Fundy may dominate the wave energy spectra (e.g., *Guest and Hay*, 2017). The combination of a steep beach slope and typically short period, wind-generated incident waves result in a narrow surf zone and energetic shore break for offshore significant wave heights of *ca*. 0.5 m and larger (*Hay et al.*, 2014). Wave incidence is predominantly shore-normal, in correspondence to the prevailing southwesterly wind direction and fetch limitation.

Episodes of cusp formation occur frequently at Advocate Beach, most commonly on the upper beach face (e.g., Fig. 5.2). The cusps generally appear as well-organised sediment structures near the high tide level, and as the tide recedes often extend tens of metres seaward, forming cross-shore bands of loose gravel and cobbles separated by sandy embayments. The beach experiences changes in forcing conditions on tidal time scales, which is reflected in daily changes in surficial sediment composition and topography.

Figure 5.2: Well-sorted beach cusps observed during a 2012 field experiment at Advocate Beach. Note the sandy overwash (red arrow) at the top of several cusp embayments, atop the high tide berm. A discussion of mixed sand-gravel cusp formation mechanisms can be found in Section 5.5.2.

Consequently, cusp episodes at Advocate Beach are generally limited to a single tide. Sediment sorting has also been observed to follow energetic wave events in the form of widespread fining of the surficial material (*Hay et al.*, 2014).

5.3 Methods

5.3.1 Experiment Overview

Data were collected during a field experiment at Advocate Beach, between 21 September and 8 October (yearday 264-281) 2015. Video imagery was recorded daily using a Raspberry Pi single-board computer and 5 megapixel camera module, both installed atop a 5.3 m tower on the beach crest, facing southward. The camera field of view (shown in Fig. 5.3) contained the intertidal zone, and spanned approximately 30 m of shoreline at spring

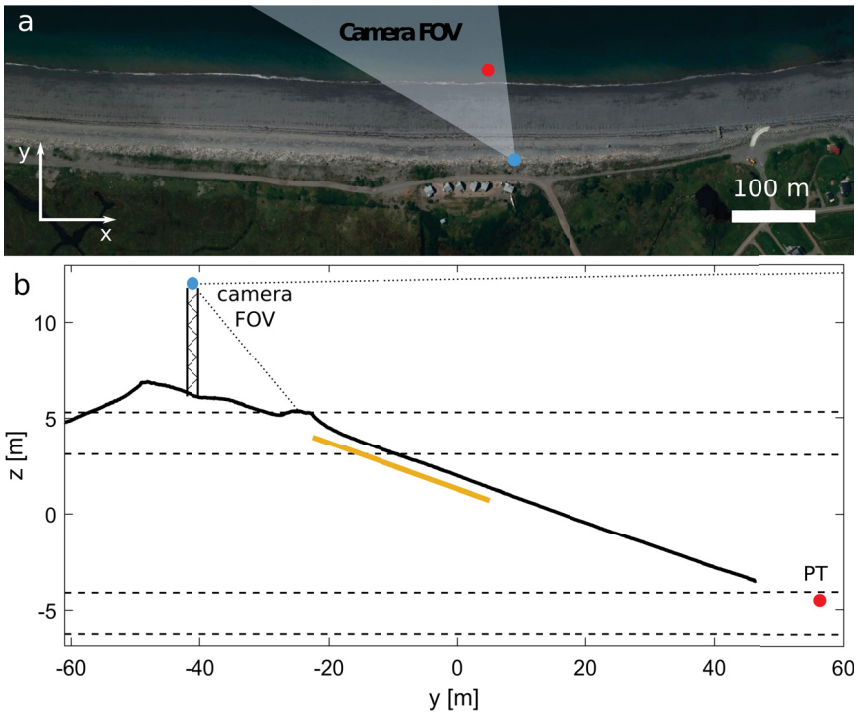

Figure 5.3: (a) Aerial view of Advocate Beach, with instrument locations during the 2015 experiment shown. The location of the camera tower is indicated by the blue dot, the camera's approximate field of view (FOV) by the light-shaded triangle, and the pressure transducer (PT) by the red dot. (b) Profile of the Advocate Beach study site from yearday 274 of 2015. Dashed black lines indicate the spring/neap tidal range observed during the experiment. The yellow line (slope of 0.12) indicates the region where cusps were typically observed, corresponding roughly to the upper one-third of the beach face.

high tide and nearly 100 m at low tide. Video was recorded with a resolution of 1920x1080 pixels at 2 Hz for roughly 6 hours per tide during daylight, corresponding when possible with the period before, during, and after high tide.

Incident wave conditions were monitored using an internally logging RBR Duo pressure sensor, deployed on an above-bed frame near lowest low water (Fig. 5.3), sampling continuously at 6 Hz between yeardays 267 and 281.

Additional pressure measurements were made using high resolution (0.02 kPa) MS5803-14BA digital pressure sensors, arranged in longshore, cross-shore, and vertical arrays. The longshore and cross-shore arrays, spanning 16 m and 9 m respectively, were designed for observing low mode edge waves, and the vertical array, spanning the upper 50 cm of the sediment column, for observing sediment pore water pressure. The pressure array observations are not treated in this chapter. Results from the vertical array are presented in

Chapter 4.

A Hemisphere Model S320 RTK (real time kinematic) GPS was used to survey the beach profile at each daylight low tide, and to obtain ground control points for image rectification. A typical beach profile is shown in Fig. 5.3.

5.3.2 Shoreline Tracking

Video imagery was used to produce time exposure-type images for analysis of shoreline position. The image products were georectified onto a plane approximating the beach surface, and rotated into longshore and cross-shore coordinates. The georectification step was completed using the g_rect toolbox for MATLAB (e.g., *Bourgault*, 2008; *Richards et al.*, 2013). Thirty-four ground control points captured on yearday 281 were used for the rectification. The same coordinate transform was used for all image data. Lens distortion was mitigated using a second-order polynomial correction implemented within the g_rect algorithm.

Time-averaged images were used to estimate the shoreline position and track the evolution of cusps on tidal and subtidal timescales. Shoreline contours were estimated from 3-minute (360 frame) average images during periods of interest. In this study the term 'shoreline' refers to a beach contour defined by the x-y position of the water's edge (i.e., the intersection of the sea surface and the beach, for fixed vertical coordinate), as determined from the time-averaged imagery. There are many techniques available for estimating shoreline position from time-averaged video, most commonly employing time exposure (TIMEX, *Plant and Holman*, 1997; *Pearre and Puleo*, 2009), variance (*Holland et al.*, 1997; *Pearre and Puleo*, 2009), and colour balance imagery (*Almar et al.*, 2008), all of which utilise peaks in intensity or intensity gradients associated with the shorebreak to infer shoreline position. A quasi-variance technique similar to that used by *Vousdoukas et al.* (2011) was found to give stable estimates over the widest range of conditions. This method uses differences in pixel intensity between each image and the preceding image summed over a desired image sequence to illuminate the regions of greatest change. The process is summarised in Fig. 5.4. In keeping with the terminology of *Vousdoukas et al.* (2011), we refer to images produced in this way as SIGMA images.

The algorithm for estimating shoreline position was designed as follows: Pixels outside a pre-defined region of interest were masked prior to georectification to reduce computation time. Each georectified SIGMA image was smoothed using a 2-dimensional, 3 point

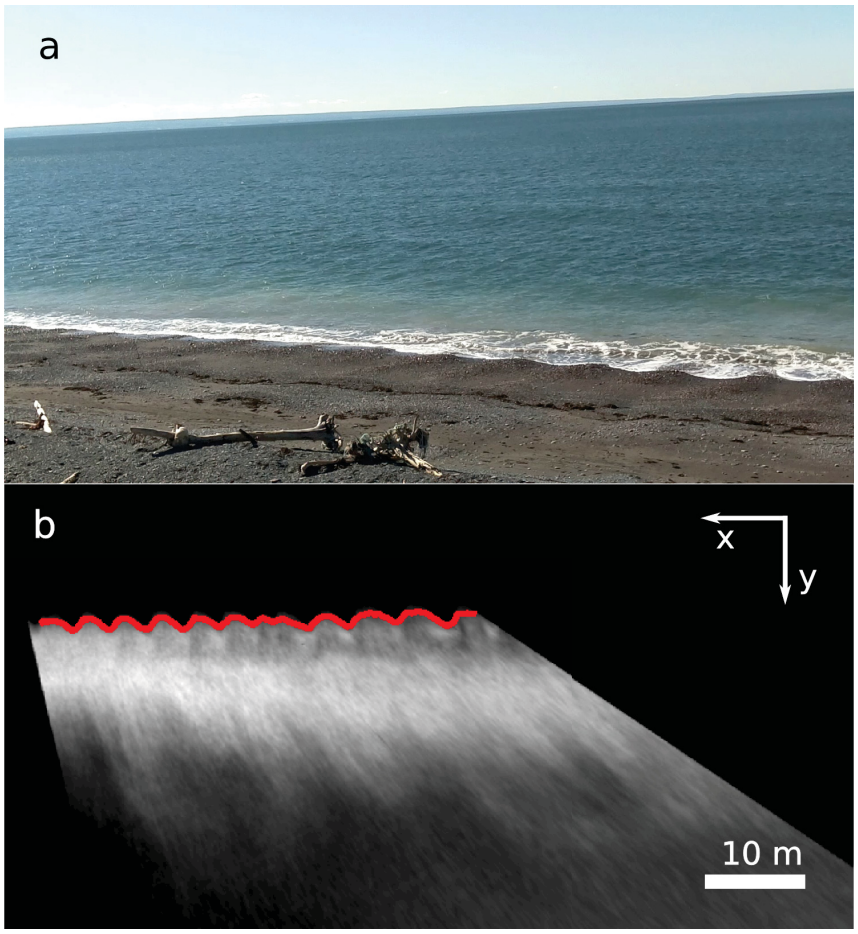

Figure 5.4: (a) Still frame captured by the tower-mounted camera during event 281A on ebb tide. (b) Orthorectified SIGMA image corresponding to the same time period as panel (a), with the estimated shoreline position overlaid in red. Lighter shades represent regions of greatest change in pixel intensity over the 3 minute (360 frame) averaging period.

mean filter (0.15 m width across-shore, 0.24 m width alongshore) to remove high spatial frequency changes in pixel intensity. Each cross-shore pixel transect was normalised by the maximum intensity value in the transect, with resultant values exceeding a predefined intensity threshold being set to 1, and all others set to 0. The resulting binary image contained 'structures' demarcating regions of high and low variability in pixel intensity. Unity-valued 'islands' containing fewer than 100 pixels were removed. The shoreward edge of the unity-valued region associated with the surf and swash zone – i.e., the first nonzero element of each cross-shore pixel column – was defined as the shoreline. The intensity threshold was set at 0.35 for all cases.

Averaging periods of 10 minutes have been previously suggested to be appropriate for similar analyses on dissipative beaches exposed to swell band incident waves (*Plant and Holman*, 1997). Mean swash periods during cusp events at Advocate Beach were observed to fall within the range of 4-6 s. The short swash periods, coupled with the rapid rate of change of water level, led to the choice of a shorter 3-minute averaging period, which typically spanned 30-45 swash cycles.

Video-tracked shorelines were used to estimate bulk cusp properties. As indicated schematically in Fig. 5.5, these variables were wavelength λ_c, the mean longshore distance between cusp horns; and cross-shore cusp amplitude A_y. A_y is a measure of cusp prominence defined as half the difference between the mean cross-shore coordinates of the cusp horns y_h, and cusp bays y_b, for a given shoreline contour. The shoreline contours were smoothed using a 7 point mean filter (0.56 m width) prior to determining wavelength and amplitude. Cusps were distinguished from other topographic irregularities by defining a minimum cross-shore amplitude threshold of 7.5 cm for the local maxima (cusp horns).

To infer bed level change (i.e., accretion or erosion), topographic mapping of the intertidal zone was carried out as an extension of the shoreline tracking method outlined above. With the low-tide, frame-mounted pressure sensor providing a vertical coordinate, video-tracked shoreline contours from respective flood and ebb tides were interpolated onto a regular 0.25 m square grid using the quadratic loess method outlined by *Plant et al.* (2002) (loess filter half-width of 1 m).

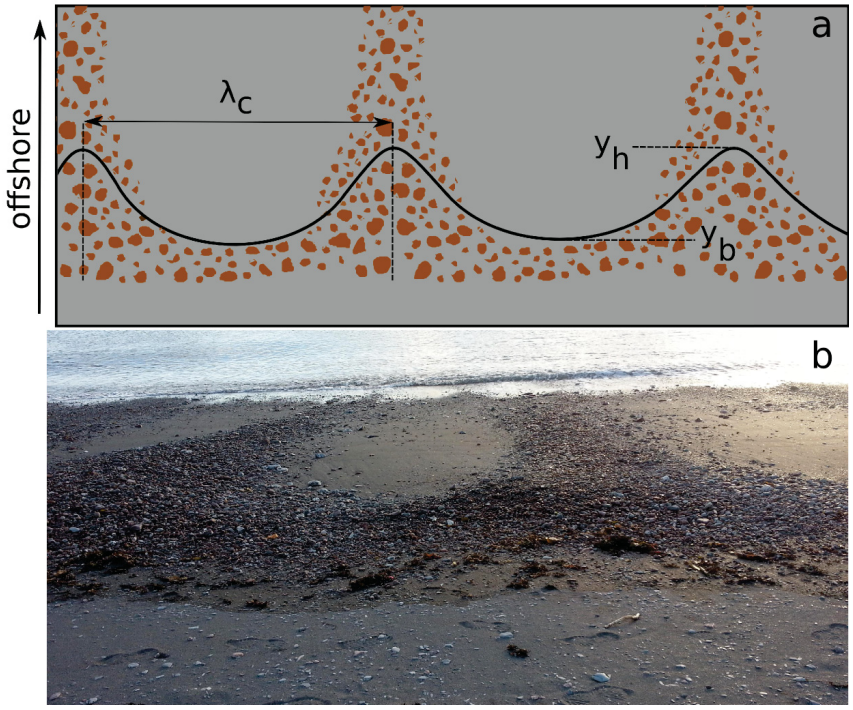

Figure 5.5: (a) A schematic showing well-sorted beach cusps in plan view. The solid black line represents a fixed-elevation contour (i.e., the shoreline). Dimensions measured were cusp wavelength, λ_c, and cross-shore cusp amplitude, A_y, which was computed as half the difference between the mean cross-shore horn coordinate, y_h, and mean bay coordinate, y_b. (b) A photograph of well-organised cusps at Advocate Beach, taken from atop the spring tide berm during event 276B. The two horns are separated by approximately 6 m. Note the strip of fine material (grey-coloured) landward of the high water line, indicated by the clumps of flotsam (mainly seaweed).

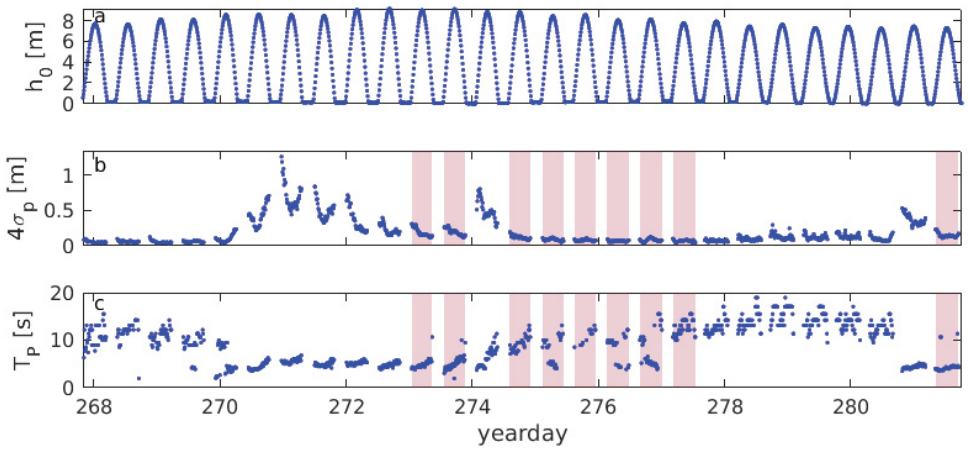

Figure 5.6: Forcing conditions during the experiment, registered by the pressure sensor near lowest low water (Fig. 5.3). (a) Tidal elevation, h_0. (b) Significant wave height, computed as $4\sigma_p$. (c) Peak wave period, T_p. Shaded regions in panels b and c indicate tides during which cusps were identified.

5.4 Results

5.4.1 Forcing

The hydrodynamic forcing conditions during the experiment, determined from the pressure sensor at the beach toe and representing "offshore" wave conditions in the present context, are presented in Fig. 5.6. Periods of low wave energy (yeardays 265-270 and 275-277), owing both to light winds and to winds from the N-NE (offshore), were interspersed with wind events from the SW, leading to the steep, locally generated wind and swell waves that are characteristic of the Bay of Fundy. The first, and strongest, of the wind events lasted two days (yeardays 270-271) with peak significant wave heights approaching 1.5 m. Two other SW wind events occurred on yeardays 274 and 281. During the period from yearday 277 to 280, wave energy spectra were dominated by long period (15-20 seconds), low amplitude (0.05-0.15 m) swell waves generated by Hurricane Joaquin which passed well to the south of Halifax (Fig. 5.1). The mean peak period, computed for storms ($4\sigma_p > 0.15$ m) and intervals between storms, was 7.6 seconds and 9.7 seconds, respectively. Mean peak wave periods measured during two previous experiments at Advocate Beach were 5-7 seconds (e.g., *Hay et al.*, 2014).

In general, cusp events occurred during periods of low wave energy, with offshore significant wave heights of O(10 cm) and wind-band peak periods of 4-6 s. Incident waves

Table 5.1: Summary of beach cusp dimensions for the five events observed during daylight hours. Cusp wavelength, λ_c, and cross-shore amplitude, A_y, were computed from contiguous cusps near the time of peak pattern regularity for each event.

Event (yd, tide)	λ_c (m)	A_y (m)
273, B	3.88 ± 1.10	0.32
274, B	3.13 ± 0.54	0.20
275, B	2.75 ± 0.63	0.13
276, B	6.29 ± 0.39	0.61
281, A	3.79 ± 0.53	0.46

were short-crested. Offshore wave heights of 10 cm correspond to break point wave heights of *ca*. 17 cm based on the breaker criterion of *Dean and Dalrymple* (1984, p. 115). Wave incidence angle was not measured, but was generally observed to be shore-normal, owing to the prevailing southwestly wind and fetch limitation.

Tidal currents were not measured, but have previously been observed to be weak near the shoreline. *Hay et al.* (2014) reported mean alongshore currents of less than 0.25 m s^{-1}, recorded at a mid-tide platform roughly 0.5 m above the bed. The maximum values occurred during high tide, when the water depth was greatest at the location of the instrument platform. The alongshore currents were much weaker–less than 0.08 m s^{-1}–immediately after the shorebreak passed the instrument platform on the rising tide, suggesting that the tidal currents are likely negligible in comparison to surf- and swash-driven flows.

5.4.2 Cusp Occurrence

Over the experiment's two week duration, nine cusp events were identified (Figs. 5.6b, 5.6c), five of which occurred during daylight. Cusp events are herein defined to include instances of incipient cusp formation: i.e. longshore topographic undulations and sediment size-sorting were apparent, but where stable, uniform horn spacings may not have emerged.

Cusp presence during these events was limited to the upper third of the beach face, as indicated in Fig. 5.3. The dimensions of the cusps observed during the five daylight events are summarised in Table 5.1. Cusps generally formed near the high water line (HWL) during high tide, when the rate of change of shoreline position was greatly reduced, and continued through early ebb, resulting in bands of well-sorted sediment extending up to 20 metres seaward. No well-formed cusps were observed at midtide, during which the rate of change of water level was as high as 3 metres per hour, or 1.25 metres across-shore

between 3 minute SIGMA video images. The presence of newly-formed cusps was rarely observable in the SIGMA image shorelines during flood tides, due to the rapid shoreward advance of the swash zone. No cusp formation was observed at the low tide shoreline.

5.4.3 Cusp Evolution

Of the five identified cusp events that occurred during daylight, three are examined in detail: (1) the first tide of yearday 281; (2) the second tide of yearday 276; and (3) the second tide of yearday 275, hereafter referred to as 281A, 276B, and 275B. The most pronounced horn-bay topographic relief was exhibited during 281A and 276B; 275B was characterised by incipient cusp formation and apparent sensitivity of formation rate to available grain size. The remaining two events were characterised by early-stage cusp formation, and are not examined here. During events 281A and 276B, existing cusps from the previous tide were inundated during flood tide and either readjusted or were planed nearly flat during high tide, with new cusps formed during the subsequent ebb. Timestack plots of the shoreline contours encompassing each of events 281A and 276B are shown in Fig. 5.7. In both cases, emergent horn positions appear to have been influenced by the pre-existing morphology.

5.4.3.1 Event 281A

Fig. 5.8 shows the forcing conditions and cusp parameters associated with event 281A. Significant offshore wave heights were 11-16 cm, corresponding to wave heights of 18-25 cm at the break point. Peak incident wave periods were 4-5 s. Relict cusps from the previous tide had a mean wavelength of 5 m and mean cross-shore amplitude of 0.5 m at maximum relief (Fig. 5.8d-f, 12:00-12:40). The HWL did not reach the maximum shoreward extent of the relict cusps due to a decrease in mean high water (MHW) from 7.5 m during the previous tide to 7.3 m. During high tide, local adjustments to cusp spacing were observed, with some horns maintaining their alongshore positions and others shifting or branching until a new mean wavelength of 4 m was reached (12:40-13:30). The cross-shore amplitude of the cusps was reduced to a minimum of 0.2 m during the adjustment period, and returned to a maximum of 0.5 m. The transition time between maximum cross-shore amplitudes was *ca*. 1 hour. The newly formed cusp field had regular horn spacing, with a standard deviation of 0.4 m during and immediately following maximum cross-shore amplitude (Fig. 5.8d, 13:50-14:30). Cusp formation continued

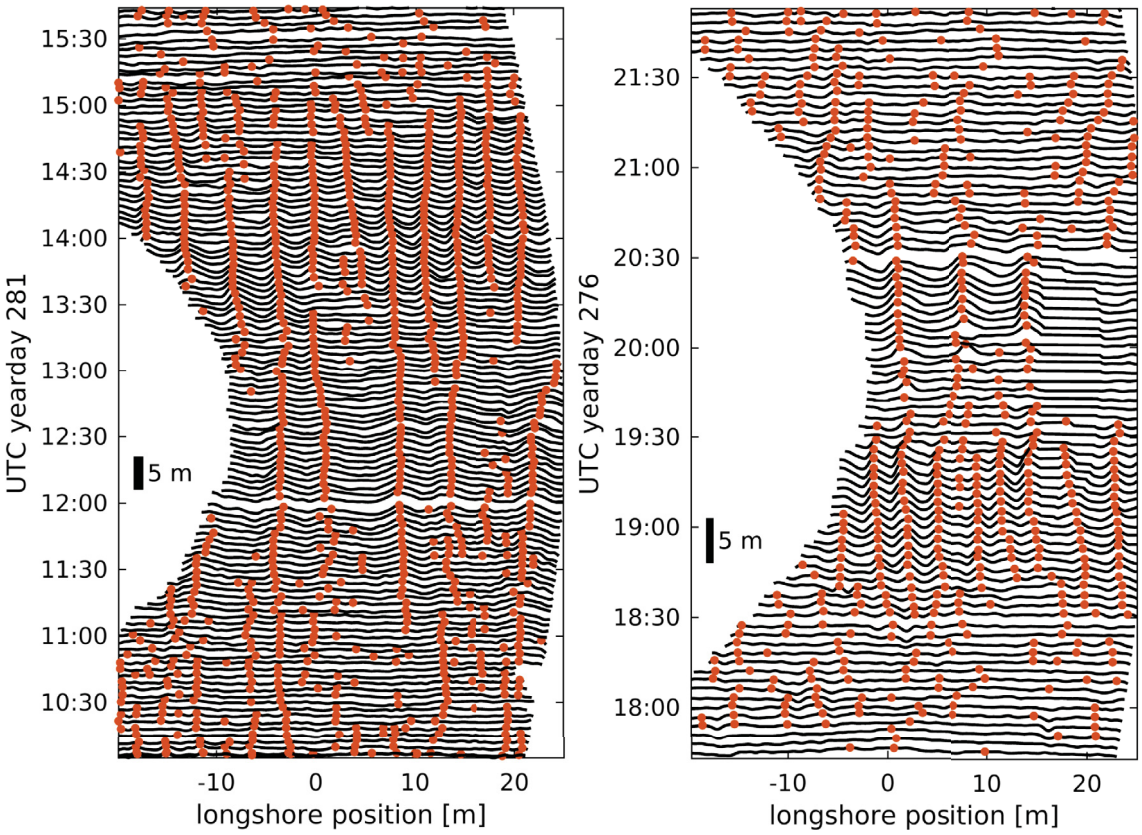

Figure 5.7: Timestack plot of the shoreline contours extracted from SIGMA images at 3-min intervals during cusp events 281A (left) and 276B (right). Orange dots mark local maxima exceeding a cross-shore amplitude threshold of 7.5 cm. Persistent maxima correspond to the locations of cusp horns. High tide was at approximately 12:30 during event 281A, and 19:45 during event 276B. The cross-shore spatial scale is indicated by the vertical black bars.

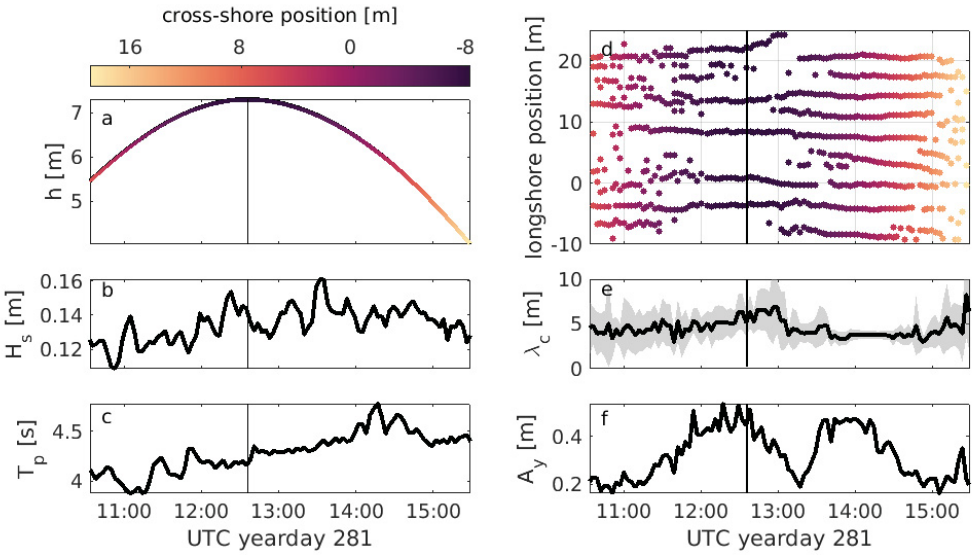

Figure 5.8: Time series of hydrodynamic conditions and morphodynamic response during cusp event 281A. (a) Water depth, h, registered by the low-tide pressure sensor. The colourscale indicates the cross-shore shoreline coordinate, estimated using the water depth h and the mean beach slope ($\beta_s = 0.12$), and translated to conform to the locally defined coordinate system. (b) Significant wave height, computed as $4\sigma_p$. (c) Peak wave period, T_p. (d) Longshore cusp horn coordinates, defined as any maxima in the video-tracked shoreline contours exceeding a cross-shore amplitude threshold of 7.5 cm. The cross-shore coordinate colourscale is the same as in panel (a). (e) Mean beach cusp wavelength, λ_c, computed as the mean separation between the maxima plotted in panel (d). The gray-shaded region indicates $+/-$ one standard deviation from the mean. (f) Cross-shore cusp amplitude, A_y. The vertical black line in all panels indicates high tide.

down the foreshore with the outgoing tide, resulting in well sorted bands of gravel and cobbles extending over 20 m seaward of the high tide level.

5.4.3.2 Event 276B

Forcing conditions and cusp parameters during event 276B are presented in Fig. 5.9. Significant wave heights at the beach toe were 8-12 cm, corresponding to break point wave heights of 15-21 cm and peak periods of 5-6 s. During flood tide, the relict cusp topography from the previous tide was intersected by the advancing shoreline. These relict cusps had a mean wavelength of 4 m and peak cross-shore amplitude of 0.5 m (Fig. 5.9d-f, 18:50-19:20). MHW during the previous tide was 8.1 m. The existing cusps were overtopped during high tide of 276B, during which MHW reached 8.2 m. The cusps were planed almost flat within *ca.* 10 mins (19:20-19:30). The new cusp field emerged equally rapidly after high tide, and had a mean wavelength of 6 m and peak cross-shore amplitude

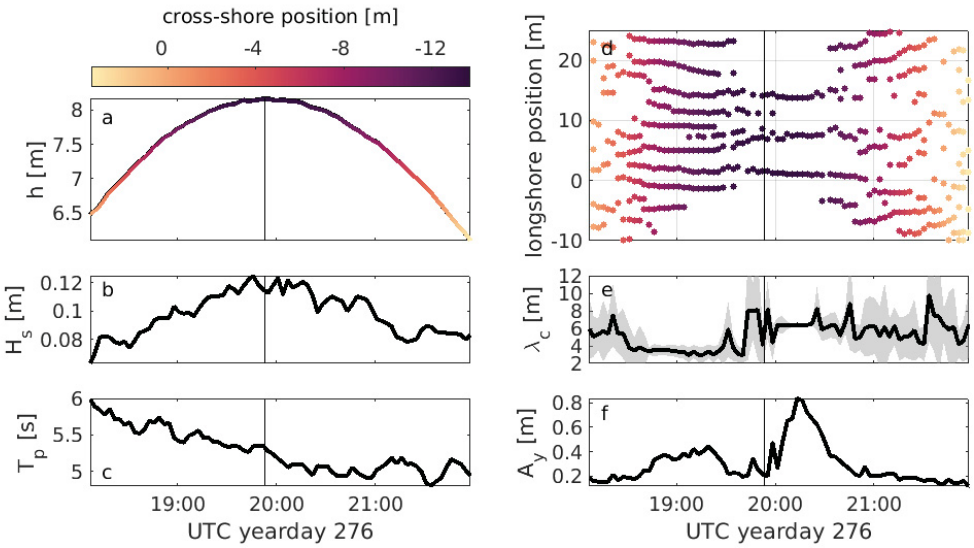

Figure 5.9: Time series of hydrodynamic conditions and morphodynamic response during cusp event 276B. See Fig. 5.8 caption for panel descriptions.

of 0.8 m (20:00-20:15). The new cusp horns formed in locations where relict horns existed. The transition time between cusp fields, from maximum old to maximum new cross-shore amplitude, was *ca.* 50 minutes (Fig. 5.9f).

Maintenance of the high-tide cusps did not continue as the water level receded during ebb. After the shoreline reached roughly 5 m seaward, the beach returned to an effectively planar state. It is important to note that the transition from cuspate to planar topography was not a result of cusp erasure or reworking, but rather a result of an increase in the rate of change of sea level such that continued cusp formation was not maintained.

5.4.3.3 Event 275B

The cusp event 275B was preceded by a period of energetic waves on yearday 274, during which MHW reached 8.9 m. The wave event peaked early in the day and left a layer of sand on the beach surface. Though uncommon in general, this effect – i.e., fining of the surficial sediments following energetic wave forcing – is consistently observed at Advocate Beach, and attributed by *Hay et al.* (2014) to the gathering of sand into the crests of metre-wavelength ripples to then be planed flat by the swash on the receding tide. During the first tide of yearday 275 (8.5 m at MHW), light, wind-band wave forcing returned the beach surface up to the high tide shoreline to a more typical, well-mixed state, leaving a strip of fine material extending 4-5 m landward of the HWL. This strip is visible in Fig.

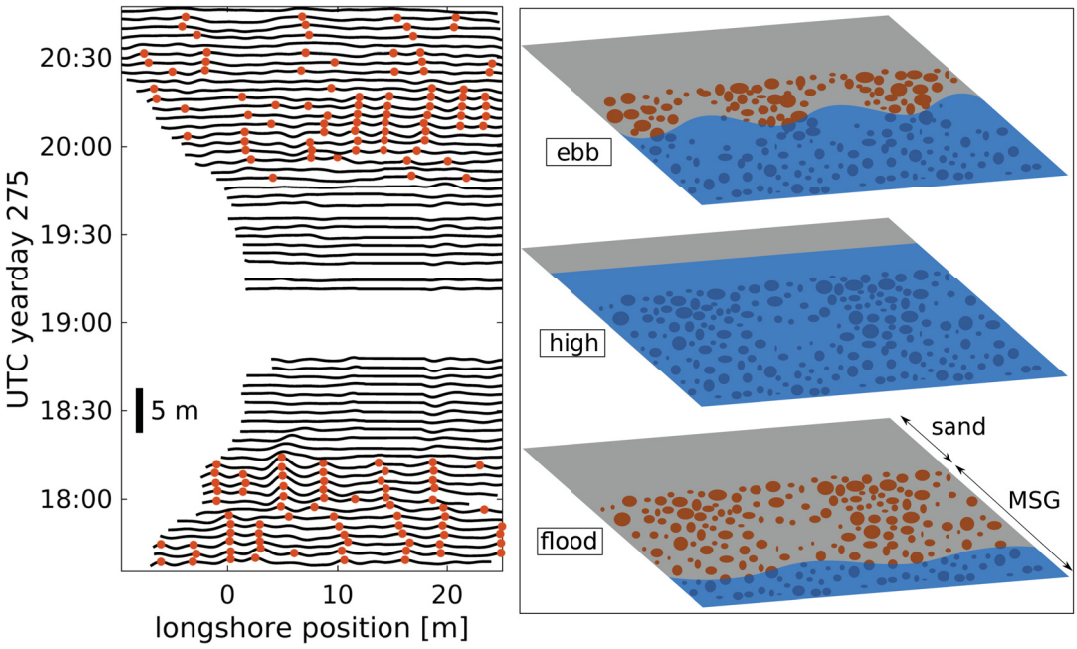

Figure 5.10: Left panel: A timestack of video-tracked shoreline contours associated with cusp event 275B. Peaks (cusp horns) were marked with orange dots if more than three surpassed a cross-shore amplitude threshold of 7.5 cm. The gap of roughly 20 mins encompassing 19:00 UTC corresponds to high tide. No video was recorded during this time. The cross-shore spatial scale is indicated by the vertical black bar. Right panel: A cartoon illustrating the sequence of beach sediment and tide states leading to grain size dependent cusp formation during event 275B. No cusps formed during high tide, when only sand was present on the beach surface. Cusp formation was initiated during ebb, when the shoreline coincided with mixed sand and gravel at the beach surface.

5.5b, landward of the well-sorted cusps. The incoming tide of 275B (8.6 m at MHW) inundated existing cusps at the upper extent of the well-mixed sediment region. No cusp formation was observed during high tide, while the shoreline coincided with the strip of fine material. Nascent cusp formation was observed on the ebb tide, initiation coinciding with shoreline recession to the well-mixed portion of the beach surface. This process is summarised in Fig. 5.10. The incident wave height and period measured at the beach toe ranged from 7-12 cm and 4.5-6.5 s, respectively, throughout. The possible effects of available grain sizes on cusp formation are discussed further in Section 5.5.2.

5.4.4 Accretion and Erosion

In order to evaluate the contributions of accretion and erosion in the evolution of new cusps, bed levels prior to and following high tide were compared for one of the three cusp events outlined above. The video-tracked shoreline contours associated with event

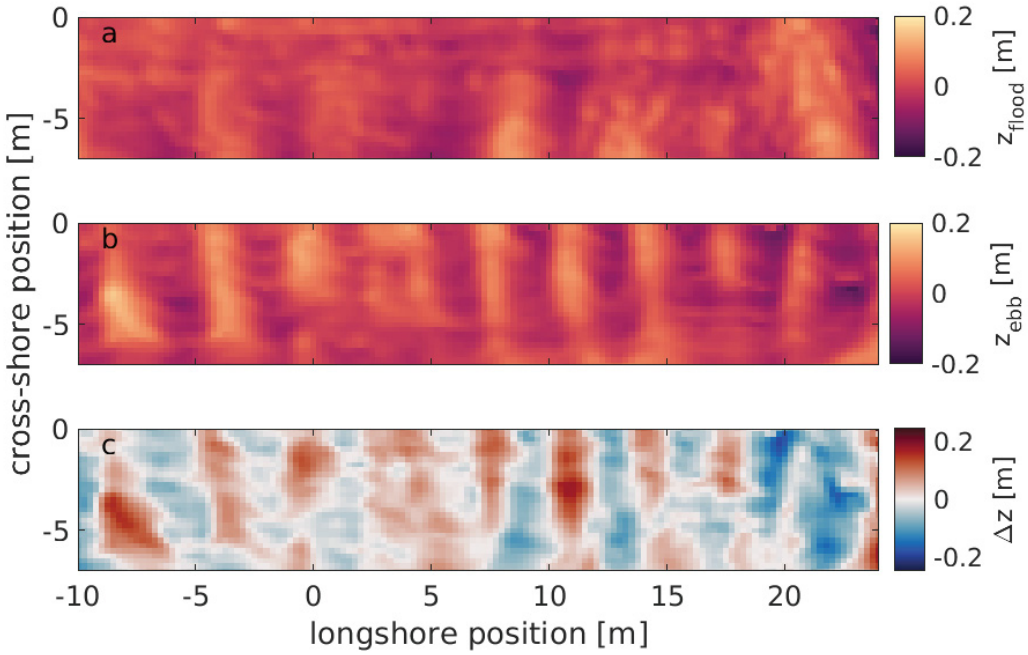

Figure 5.11: Beach surface elevations interpolated from video-derived shoreline contours and pressure data. (a) Relict topography, derived from event 281A flood tide shoreline contours, presented as deviation of the beach surface elevation from a best-fit plane. (b) New topography, derived from event 281A ebb tide contours, as deviation from the same plane used in (a). (c) Difference in bed elevation between flood and ebb.

281A were interpolated onto a regular grid so that changes in bed elevation between flood and ebb tide could be estimated. Each contour was assigned a z-coordinate using water depths registered by the pressure sensor. To maximise the in-frame shoreline at high tide, while mitigating the effects of changing light and forcing conditions on the estimated shoreline positions, the grid-domain was limited to a rectangular region near high tide with dimensions of 34 m in the alongshore and 7 m across-shore. The shoreward extent of the domain was chosen to omit the region nearest to high tide, where the topography likely remained dynamic through successive shoreline estimations due to the temporary stationarity of the sea level.

The flood and ebb cusp topography, and the associated residual field, are shown in Fig. 5.11. Though interpretation of the topographic change is complicated by the presence of cusps from the previous tide, it is apparent that accretion generally occurred at the cusp horns, and erosion in the embayments. The overall flood-ebb volume change in the control region was small (<1 m^3), suggesting that sediment volume was conserved.

5.5 Discussion

5.5.1 Cusp Morphodynamics

The field measurements presented herein describe the short-term morphological evolution of beach cusps on a steep mixed sand-gravel beach. Cusps formed during periods of low wave energy, and were characterised by pronounced grain size sorting. The generation and evolution of cusps was strongly influenced by tide stage, and the location and dynamics of cusp horns (i.e., erasure/(re)emergence versus branching/merging/shifting) appeared to depend on the HWM and its location relative to any pre-existing cusp morphology.

During instances of cusp formation, relict cusp horns branched (i.e., wavelength approximately halved), merged, or shifted in adjustment to the changes in forcing, or were planed nearly flat. The relict horn response appears to have been related to the range of the tide during adjustment: specifically, the changes in MHW within the spring-neap cycle, which resulted in up to 0.5 m differences between consecutive high tides, corresponding to a 4-5 m cross-shore change in the HWL. Because of a shoreward migration of the HWL during event 276B, the relict cusps were overtopped during high tide, and their cross-shore amplitude was rapidly reduced–the cusps appearing to be planed almost flat (see Fig. 5.9d-f, *ca.* 19:15-19:45). The relict cusps during event 281A were not overtopped, and the period of decrease in cross-shore amplitude coincided with localised branching and longshore adjustment of the horn positions (Fig. 5.8d-f, 12:30-13:30).

No cusp formation was observed near the low tide shoreline. There are two potential explanations: (1) The sediment size distribution tended toward increasingly larger grain sizes approaching the beach toe. Large, sometimes boulder-sized material may have stabilised the surficial sediments via high mobilisation thresholds and disruption of flow near the bed, preventing cusp formation. (2) Near saturation of the inter-granular pore spaces by ground water reduced the permeability of the beach surface relative to the upper beach, decreasing the influence of infiltration-related feedbacks.

The properties of cusp horn branching, merging, local adjustment, and interaction with relict morphology (Figs. 5.7-5.9) have been previously observed by *Almar et al.* (2008) and *Vousdoukas* (2012), both using image-based shoreline tracking techniques. *Almar et al.* (2008) tracked cusp horn positions (*ca.* 20 m spacing) daily over periods of weeks to months on a steep, microtidal, medium sand beach. They noted that the observed merging and disappearance of cusp horns is consistent with cusp dynamics simulated by *Coco*

et al. (2000) using a model based on self-organisation. *Vousdoukas* (2012) observed horn positions daily over a 5 month period on a steep (greater than 1:10 mean slope), mesotidal, medium to coarse sand beach. Cusps on the upper beach face had large wavelengths (mean of 50 m), and were stable, lasting from days to months. The horn positions were displaced coinciding with storm events, sometimes resulting in branching or merging, though the discrete nature of the sampling did not capture the transitions clearly. Cusps on the lower beach face were of shorter wavelength (mean of 38 m), and were more dynamic, often changing daily and lasting no longer than a week. Both *Almar et al.* (2008) and *Vousdoukas* (2012) emphasised the influence of existing morphology on cusp evolution, acknowledging that evolution occurred in most cases as a result of localised adjustment rather than through the emergence of a global pattern.

The observed differences in horn response between events 281A and 276B can likely be attributed to the diffusive influence of the surf zone on the beach surface sediments, which has similarly been implicated in tidal modulation of cusp amplitude on sand beaches. *Coco et al.* (2004) observed lower topographic relief of developed cusps during flood tide, and higher relief during ebb. They attributed this difference in relief to the smoothing of features seaward of the swash front, where the impinging surf zone during flood increasingly mobilises sediment, damping cusp growth. The observed modulation of relief was reproduced with a self-organisation-based numerical model by incorporating surf-zone morphological smoothing (sediment diffusion) and in/exfiltration. Their model results indicated that smoothing was of leading order importance in this process, with infiltration effects being of lesser importance. Our results show that cusp evolution at Advocate Beach is similarly modulated, with cusp formation being favoured during ebb tide. Though the relative importance of surf zone smoothing and infiltration is not known, one could speculate that infiltration is more important than in the sandy beach case due to higher hydraulic conductivity and grain-size sorting effects.

Garnier et al. (2010) noted that large beach cusps (25 m spacing or more) may be acted upon by surf as well as swash zone forces at different stages of the tide, due to their large cross-shore extent. Their results suggest that surf zone processes may not be purely destructive, and in some cases may reinforce cusp patterns. They ascribed this to a surf zone hydrodynamic instability independent of swash or tide processes, which they investigated using a numerical model. The cusps at Advocate Beach are morphologically quite distinct

from the large beach cusps observed by *Garnier et al.* (2010), and though we have no observations of subaqueous morphology, it is apparent that swash processes dominated the evolution of cusps in our case–the impinging surf zone during flood appearing to act destructively as suggested by *Coco et al.* (2004). This is evidenced by the rapid destruction of relict cusps during event 276B, which were inundated during high tide. *Almar et al.* (2008) similarly concluded that the overtopping of existing horns leads to decreased control exerted by the existing morphology on flow, reducing the tendency of horns to divert flow.

5.5.2 Timescales and the Influence of Grain Size Distribution

For cusp events 281A and 276B, the time between maximum relief (as determined using the cross-shore cusp amplitudes) of relict cusps and newly formed cusps was *ca*. 1 hour. This period encompasses relict cusp amplitude decay and emergent cusp amplitude growth. Conceptually, cusps approaching equilibrium under steady forcing conditions would be expected to become growth-inhibited as a result of negative feedback processes. Here, the cross-shore amplitude growth and decay timescales are similar in magnitude and appear exponential in form, but both are different from the timescale representative of the process leading to equilibrium cusps (e.g., logistic growth). It is not apparent that equilibrium cusp conditions were met during the Advocate experiment. Hereafter, discussions of timescale refer to the emergence timescale associated with initial cusp growth, and the relict cusp decay timescale.

A visual inspection of the cross-shore cusp amplitude time series for events 281A and 276B (Figs. 5.8f, 5.9f) indicates that the timescales associated with initial cusp growth and decay are of the order of tens of minutes. Indeed, fitting exponential curves to the initial cross-shore amplitude growth and decay periods for events 281A and 276B yields e-folding times between 10 and 20 minutes in 3 of the 4 cases: i.e., those qualitatively well-described by the fit. These timescales are short relative to those typically reported in the field literature. Previously identified factors influencing timescale include randomness in runup trajectory (*Coco et al.*, 2000), swash period (*Dodd et al.*, 2008), swash transport capacity – presented in modelling terms via a sediment transport constant (*Coco et al.*, 2000; *Dodd et al.*, 2008), beach permeability (*Dodd et al.*, 2008), and energetics (*Garnier et al.*, 2010). Some of these factors are interrelated, as has been acknowledged in the context of cusp formation via (for example) surf scaling or similarity parameters. The importance of mean grain size in predicting beach cusp spacing was suggested by the

model proposed by *Sunamura* (2004), in which cusp spacing is inversely proportional to grain size, but the possible effects of grain size and distribution on timescales of beach cusp evolution have not been discussed in the recent literature.

The general absence of cusps at mid-tide level on the beach face suggests a constraint on cusp formation imposed by the high rate of change of shoreline position, and allows us to establish an estimate of the minimum formation timescale. During maximum flood or ebb, the rate of change of water level was as much as 3 m hr^{-1}, or 0.007 m s^{-1} in the across-shore. Swash zone widths during cusp formation of 3-5 m divided by the 0.007 m s^{-1} rate of horizontal shoreline change gives a minimum timescale of $O(10)$ minutes. This is close to our suggested timescale for initial cusp growth of 10-20 minutes. The often-observed banding of sorted material extending tens of metres seaward from the high tide level, but terminating before mid-tide, is consistent with these values being similar in magnitude.

The event 275B results suggest sensitivity of timescale to the range of available grain sizes, with the presence of gravel and cobbles in addition to sand at the beach surface leading to shorter adjustment times. The morpho-hydrodynamic feedbacks often considered fundamental in the process of cusp formation appear to be bolstered by additional feedback mechanisms provided by the presence of a wide range of grain sizes and the process of size segregation: i.e., (1) increased and immediate feedback on flow due to larger volume displacement by individual grains, causing flow divergence and drag losses, and (2) increased infiltration losses through accumulation of coarse-grained material (i.e., gravel/cobble) in the horns. Sedimentary and hydraulic feedbacks are intrinsic in the morpho-sedimentary dynamics framework described by *Buscombe and Masselink* (2006) for gravel beaches.

In the conceptual framework put forward by *Longuet-Higgins and Parkin* (1962), cusps form most rapidly when a coarse-grained permeable surface layer sits atop a relatively well-mixed and impermeable subsurface layer. In this case, reduced infiltration through the subsurface layer would increase the ability of the swash to transport sediment. Accretion of coarse material on cusp horns would increase the thickness of the permeable layer, decreasing the strength of the backwash and thus the erodibility of the horns. Measurements of the hydraulic conductivity of Advocate Beach sediment reported by *Guest and Hay* (2017) are consistent with the conceptual framework from *Longuet-Higgins and Parkin*

(1962): the maximum value of nearly 12×10^{-4} m s^{-1} was in the upper 5 cm of the sediment column, compared to values of less than 8×10^{-4} m s^{-1} in the underlying 45 cm.

Useful insights can also be obtained from the fluvial sediment transport literature. In a flume experiment involving mixtures of sand and gravel in unidirectional flow, *Wilcock et al.* (2001) observed orders of magnitude increases in gravel transport rates when sand was introduced, despite a decrease in the overall proportion of gravel. They observed maximum gravel transport rates when sand content was between 15 and 27%, and suggested that these ratios roughly corresponded to the transition from a framework- to a matrix-supported bed. This would provide support for the notion that well-sorted accumulations of coarse material are less likely to be mobilised.

Based on the above, the development of MSG cusps could progress in a sequence similar to the following (summarised in Fig. 5.12): During the swash uprush phase, the larger-sized tail of the grain size distribution is deposited first, preferentially near incipient topographic highs where the fluid velocity decreases most rapidly. Incipient accumulations of gravel and cobbles protrude from the bed and are hydraulically rough, diverting and slowing flow. The divergence of flow around coarse accumulations during uprush strengthens the return flow in incipient bays during downrush. Thus, the capacity of the flow to mobilise large grains is reduced at the horns (lower fluid velocity), and increased in the bays (higher fluid velocity). Large grains in the developing bays, more readily mobilised by the strengthened seaward flow, are transported to the step region seaward of the shorebreak, where they may become source material for continued horn development as the tide recedes. Finer material may remain in suspension, become trapped in the interstitial spaces between larger grains, or be deposited at the shoreward edge of the developing embayment (see sand overwash in Fig. 5.2).

In addition to preferential deposition at horns due to fluid deceleration, larger particles are more readily deposited amid accumulations of similarly sized grains due to higher angles of pivot required for mobilisation and a higher degree of grain interlocking (see selection/rejection/acceptance, overpassing: *Buscombe and Masselink*, 2006). This stabilising mechanism at the cusp horns, reinforced by the hydraulic feedbacks described in the Longuet-Higgins and Parkin framework above, is comparable to armouring phenomena described more generally for sediment sorting and zonation on gravel beaches, river beds, and spits (e.g., *Isla*, 1993). Conversely, coarse particles in the cusp bays remain mobile,

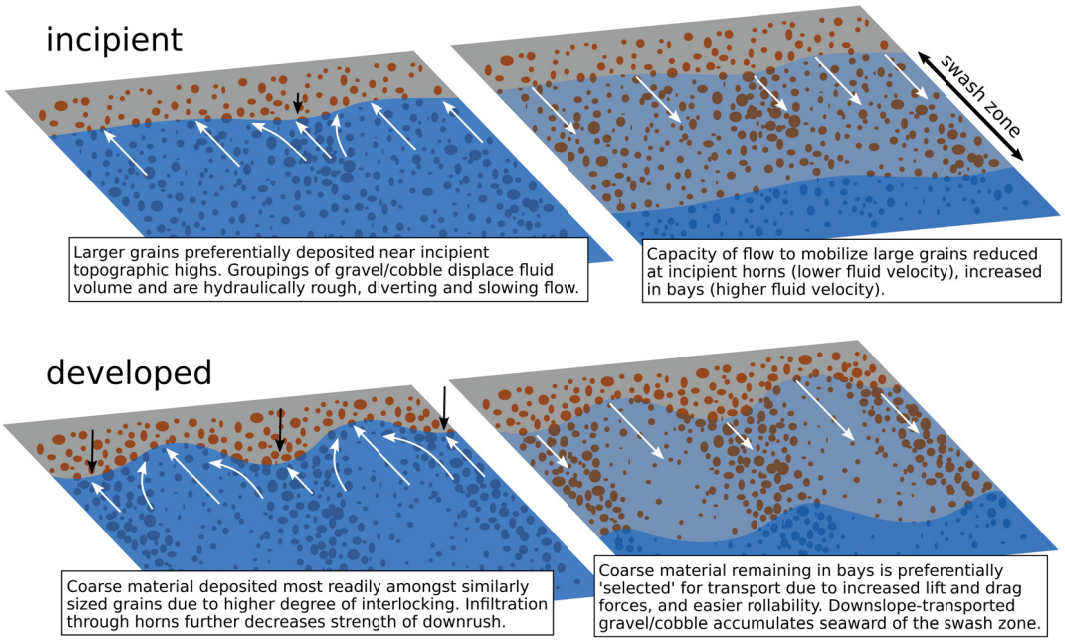

Figure 5.12: Proposed mechanisms of mixed sand-gravel cusp formation, shown for incipient cusps (upper) and developed cusps (lower). Downward directed black arrows represent infiltration. White arrows indicate swash front velocity.

being acted upon by larger lift and drag forces, and rejected by (i.e., overpassing) the finer substrate.

Though grain-size sorting between horns and bays has also been acknowledged in sand beach settings, the role of sorting in the process of sand cusp formation remains unclear. In one recent case, *van Gaalen et al.* (2011) found no statistically significant correlation between grain size and position between horn and embayment on a sandy beach on the Atlantic coast of Florida. Their suggestion that horn-coarsening and embayment-fining likely occur only after cusps have developed is in contrast to the result presented herein, and suggests a distinction between sand and mixed sand-gravel cusp formation.

5.6 Conclusions

This study makes use of video-based observations of beach cusp formation episodes to characterise timescales of mixed sand-gravel (MSG) cusp evolution subjected to fetch-limited wind waves and 10 m range tides. The observations document the evolution of cusp fields with higher temporal resolution than has been previously reported in the literature.

Cusp evolution at Advocate Beach occurred over timescales that are an order of magnitude shorter than those typically reported in the field literature. The transition from relict to newly formed cusp fields occurred over *ca*. 1 hour, with initial emergence and relict cusp decay timescales of 10-20 minutes. The general absence of cusps at mid-tide level on the beach face suggests a constraining formation timescale of $O(10)$ minutes, or $O(100)$ swash cycles, assuming nominal swash zone widths of 3-5 m at times of maximum rate of shoreline change. We provide evidence that timescale was influenced by the availability of larger grain sizes during formation, indicating the importance of the wide distribution of grain sizes to morpho-hydrodynamic feedbacks on MSG beaches. The cusp horn dynamics appeared to depend on the HWL and its location relative to any pre-existing cusp morphology. Horn accretion and embayment erosion were both shown to be important for at least one of the events, with local sediment volumes conserved.

Sediment grain size sorting within the beach cusps was pronounced, with gravel-sized material concentrated in the horns, and sand-sized sediments in the bays. The apparent sensitivity of cusp formation timescales to the local grain size distribution, particularly the presence of surficial gravel and cobble, suggests that size segregation is intrinsic to the process of mixed sand-gravel cusp evolution. MSG cusps appear to bear similarities to other patterned bed states (e.g., sorted bed forms, *Murray and Thieler*, 2004) whose formation depends upon grain-size distribution dependent transport properties. However, more directed study is needed in order to establish the role of sorting in MSG cusp formation (i.e., cause or effect).

CHAPTER 6

MORPHO-SEDIMENTARY DYNAMICS IN THE INTERTIDAL ZONE

6.1 Introduction

Mixed sand-gravel (MSG) beaches represent one of three geomorphic subtypes of gravel beach, the other two subtypes being pure gravel and composite gravel, as outlined by *Jennings and Shulmeister* (2002). MSG beaches are generally characterised by a swash-dominated hydrodynamic regime, and well-mixed sediments both across-shore and at depth. The need for improved understanding of MSG beach processes has been emphasised in the literature of the last two decades, given the relative stability of coarse grained beaches in the face of energetic conditions and rising sea levels, and the increasing usage of mixed-sized sediments in beach replenishment schemes (*Mason and Coates*, 2001).

Of particular note in understanding the evolution of MSG beaches is the relationship between beach surface texture, as determined by properties of the surficial grain size distribution, and the hydrodynamics, groundwater dynamics (hydraulics), and morphology. The morphodynamic model (*Wright and Thom*, 1977; *Buscombe and Masselink*, 2006), which for decades has been used to describe the evolution of sandy coastlines, cannot account for the changes in the morphological response that result from textural differences in bed state. Though linkages between bed texture and morphology have been discussed in the literature for decades (e.g., *Longuet-Higgins and Parkin*, 1962; *Moss*, 1962; *Isla*, 1993; *Carter and Orford*, 1993; *Sherman et al.*, 1993; *Masselink and Li*, 2001; *Buscombe and Masselink*, 2006; *Masselink et al.*, 2007; *Austin and Buscombe*, 2008; *van Gaalen et al.*, 2011; *Guest and Hay*, 2019), the relative importance of sedimentary feedbacks in

morphological evolution remains unclear. In their gravel beach review paper, *Buscombe and Masselink* (2006) proposed "morpho-sedimentary dynamics" (MSD) as a preferred framework within which to carry out future research on gravel beaches. The framework treats differences in bed texture resulting from variations in the characteristics of the surficial grain size distribution as an intrinsic component of the dynamics of morphological evolution.

Sediment transport on MSG beaches is governed by complex interactions between forcing by waves and tides (*Nordstrom and Jackson*, 1993), grains of different size and shape (*Stark et al.*, 2014; *Stark and Hay*, 2016), and hydraulic effects (in/exfiltration and groundwater response; *Horn*, 2006). Spatial and temporal variability in grain size properties, hydraulic conductivity, and mobilisation thresholds, along with transport regimes which may be characterised by conditions of fractional mobilisation of material (e.g., *Wilcock and Crowe*, 2003), or dependence of individual particle transport on the background substrate (*Carter and Orford*, 1993), pose a challenge for the incorporation of MSG transport in contemporary predictive models. Indeed, there are indications that the phenomenological response of MSG beach sediments to forcing may be fundamentally different from the response expected on a sand beach: Several authors reporting on MSG beach sedimentology (*Nordstrom and Jackson*, 1993; *Pontee et al.*, 2004; *Curtiss et al.*, 2009; *Miller et al.*, 2011; *Hay et al.*, 2014) have observed decreases in the mean grain size of beach surface sediments in response to energetic wave forcing, and surficial coarsening following fairweather conditions. On sandy beaches, the conventional understanding is of offshore transport of finer material during instances of increased wave height and steepness, due to swash velocity asymmetry, and onshore transport during low energy forcing, leading to differences in beach characteristics seasonally, or with differences in orientation (e.g., *Bascom*, 1951). The typically anticipated positive relationship between forcing and surficial grain size on sandy beaches is implicit in recent grain size response modelling efforts (see *Prodger et al.*, 2016), which have been shown to predict the mean surficial grain size with considerable skill.

There are few examples in the field literature of studies designed to investigate the correlation between morphological and sedimentary (hereafter, morpho-sedimentary) dynamics. Those studies that have sought signatures of correlation between bed level and grain size have had mixed results. *Masselink et al.* (2007) surveyed bed level and grain

size across the profile of a macrotidal sandy beach over a 20 day period. They reported changes in mean grain size and sorting that were mostly unrelated to the morphological response, with two exceptions wherein instances of erosion were associated with bed surface coarsening. *Austin and Buscombe* (2008) collected observations of bed level and grain size properties across the intertidal zone of a macrotidal gravel beach over the course of a tidal cycle. They reported some positive correlation between mean grain size and bed level change at the locations of the berm and the step, though distinct phases of morphological change were not otherwise evident in the sedimentary signal. Both *Masselink et al.* (2007) and *Austin and Buscombe* (2008) acknowledged their sampling strategies as a potential limitation on revealing clearer trends in the grain size measures.

Mixed substrates have been suggested to favour the formation of transient, secondary morphological features or patterns on the beach surface, including beach cusps (e.g., *Longuet-Higgins and Parkin*, 1962; *Guest and Hay*, 2019). The tendency for gravel (especially MSG) beach sediments to display heterogeneity in space and time, and to self-organise into sorted sediment structures with linkages to morphological features (e.g., *Sherman et al.*, 1993; *Austin and Buscombe*, 2008) makes MSG beaches well suited to investigations of the coevolution of morphology and grain size.

Here, results are presented from a 2018 field study of a MSG beach. The study made use of survey observations of beach surface elevation and mean surficial grain size sampled at low tides over a two-week period. The objective of this study is to investigate the coevolution of bed elevation and mean grain size, seeking insight into the phenomenological role of grain size in swash zone morphological evolution, and to discuss the observed and uncommon phenomenon of MSG beach surficial sediment fining immediately following energetic forcing events.

6.2 Methods

6.2.1 Experiment Overview

The field experiment was conducted between 14 and 27 October, 2018 at Advocate Beach, located in Nova Scotia at the head of the Bay of Fundy. The 27 tides spanned by the experiment are referred to throughout this chapter by their low tide index: tides 1 through 27.

Beach-scale monitoring of bed elevation and beach surface grain size was carried out

using RTK (real time kinematic) GPS and camera surveys. Local grid coordinates were defined in keeping with previous experiments at the site (Chapters 4 and 5), with the origin defined as the former position of a vertical pressure sensor array (see Chapter 4), approximately 20 m seaward of the nominal high tide shoreline. The coordinate system is such that x is alongshore, positive to the northwest, and y is positive offshore. A survey grid was established (see Fig. 6.1), consisting of one cross-shore beach transect spanning 90 m (y =-30 to 60 m in local grid coordinates) and two longshore transects spanning 75 m (x =-50 to 25 m), all sampled at 3 m intervals, and a more densely sampled grid consisting of six 24 m longshore transects spaced at 1 m intervals, and 2 m intervals across-shore (x =-24 to -1 m, y =-15 to -5 m). The cross-shore transect (hereafter referred to as CT) extended from the beach crest to the mean spring tide low water shoreline along the $x = 0$ m coordinate, though the number of surveyed points differed from tide to tide depending on the shoreline position at the time of the survey. The two longshore transects were positioned on the upper beach face, but seaward of the nominal high water line. The most seaward transect (LT1) was positioned at $y = -5$ m, and the more shoreward transect (LT2) at $y = -12$ m. The densely sampled grid (DG), and the larger grid layout in general, were designed to encompass the high tide shoreline, in order to emphasise high tide swash processes.

The survey grid was sampled every low tide from tide 14 to 27, an RTK GPS position and photograph being taken at each grid point. Photographs were taken using a 20 megapixel Canon Powershot Elph 190 camera, mounted to a tripod at fixed height. Prior to tide 14, different grid configurations were surveyed, and only one survey was conducted per day (i.e., once per two tides). Data collected prior to tide 14 are not included here.

The cross-shore coordinate of the high water line (HWL; herein defined as the cross-shore coordinate of the high tide swash runup maximum) for each tide was determined post-experiment using the survey photography, by identifying features associated with the maximum swash runup limit: seaweed or similar flotsam, the transition from wet to dry substrate, or clear boundaries in sediment size or shape. Thus, given the cross-shore spacing of stations in grid DG, the HWL coordinates are considered accurate to within ± 1 m.

An RBR Duo pressure sensor was deployed on a heavily weighted frame resting on the bed near the neap low water shoreline to observe the “offshore” wave climate. Due

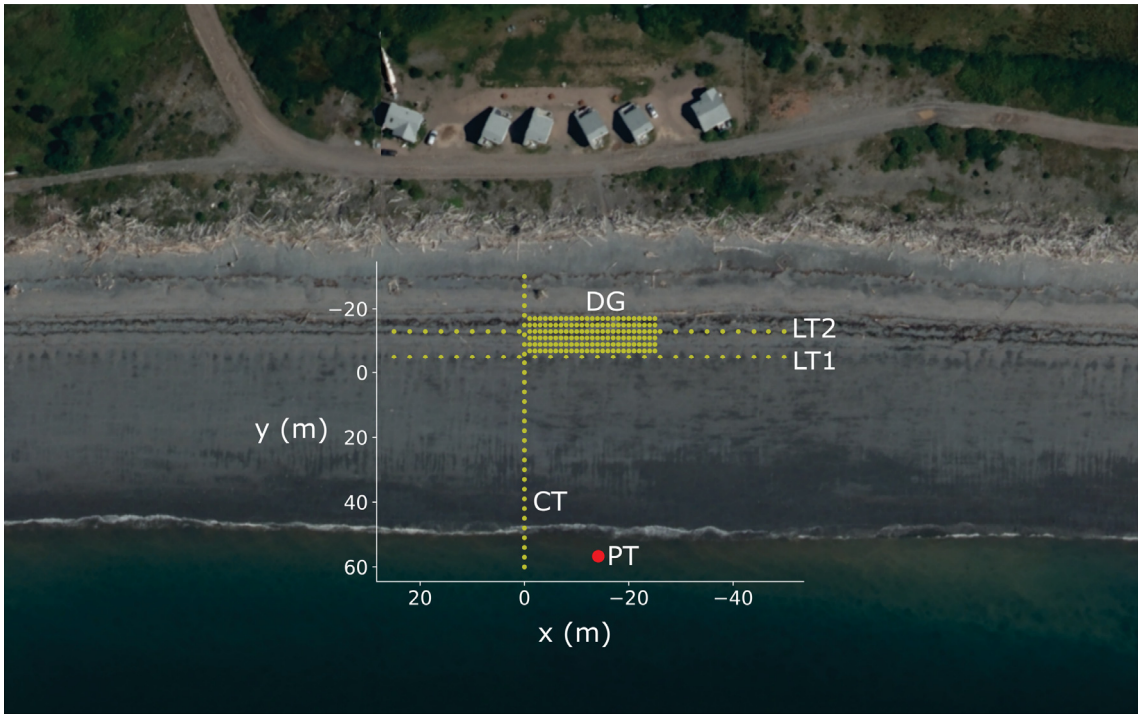

Figure 6.1: Aerial photograph of Advocate Beach, with the survey configuration overlaid. A GPS point and photograph were taken at each survey station (yellow dot), each low tide. The survey layout consisted of four subsets: one cross-shore transect (CT), two longshore transects (LT1 and LT2), and a more densely sampled grid (DG). The red dot indicates the position of the pressure transducer (PT).

to a prolonged period of high winds and energetic wave conditions at the outset of the experiment, the pressure sensor was not deployed until the sixth day of the experiment (prior to tide 10). Pressure data were recorded at 6 Hz.

The coevolution of beach morphology and sediment properties in the swash zone was investigated using an array of collocated ultrasonic range sensor and camera pairs, as well as an overhead camera used for monitoring tracer cobble transport. These data are presented in Chapter 7.

6.2.2 Digital Grain Sizing

A wavelet-based digital grain sizing (DGS) package (see *Buscombe*, 2013), implemented in Python, was used to estimate arithmetic grain size statistics from the camera imagery. The DGS algorithm does not require calibration, and takes as input a grain-resolving image containing only sediment.

The survey images were cropped to half width and height in the centre of each frame, corresponding to a field of view at the bed of 0.33×0.25 m, with the camera height set at *ca*. 0.3 m above the bed. Input parameters for the algorithm include a pixel to physical unit scaling, a maximum feature diameter to be resolved, and a dimensional scaling factor. The pixel to physical unit scaling was computed by photographing an object of known length and width. The same scaling was used for all survey images. The maximum feature diameter, defined as the inverse ratio of the pixel width of the frame to the width of the largest feature to be resolved, was set at 56 mm. The dimensional scale factor was set at 0.8. See Appendix B for a discussion of the choice of dimensional scale factor, as well as for more detailed descriptions of the remaining input parameters.

Though the algorithm is capable of returning a full grain size distribution, validation of the output against the distributions from both sieve and manual point count analyses (see *Barnard et al.*, 2007; *Buscombe et al.*, 2010, or Appendix B for a description of the point count method) indicated that only the lowest moment of the grain size distribution (mean grain size) was captured satisfactorily. The validation of the higher order moments (i.e., sorting, skewness, kurtosis) revealed that they were not well estimated by the algorithm, so only the mean grain size results are included here. We attribute the algorithm's poor representation of the higher order moments to the wide grain size distribution. See Appendix B for further discussion of the validation procedures.

6.2.3 Correlation Analysis

Pearson correlation coefficients were computed between measures of bed level, z, and mean grain size, MGS, both defined at a given set of space and time coordinates: e.g., $z = z_{ij}(t)$, where the indices i, j indicate the x, y (longshore, cross-shore) coordinates, and t is an integer low tide index. MGS and other, similar measures are equivalently defined. Changes in bed level and mean grain size from one tide to the next are denoted using Δ notation, e.g., $\Delta z = z_{ij}(t) - z_{ij}(t-1)$. Primed values denote observations associated with the previous time (i.e., tide) step, e.g., $z' = z_{ij}(t-1)$, and overbar notation is used where spatial averaging was done. That is, the spatial mean of the MGS observations for a survey transect with N stations is given by

$$\overline{\mathrm{MGS}}_j = \frac{\sum_{i=1}^{N} \mathrm{MGS}_{ij}(t)}{N}. \tag{6.1}$$

Spatial means were computed only over longshore survey transects (note the summation over i alone in equation (6.1)), since the observed properties – notably MGS – had a characteristic (i.e., non-Gaussian) structure in the across-shore. The subscript j, indicating the cross-shore coordinate associated with the transect over which the computation was made, is implicit in the equations below, but is hereafter omitted. The Pearson correlation coefficient for a given cross-shore coordinate associated with a given tide is

$$r = \frac{\sum_{i=1}^{N}(X_i - \overline{X})(Y_i - \overline{Y})}{\sqrt{\sum_{i=1}^{N}(X_i - \overline{X})^2 (Y_i - \overline{Y})^2}}, \tag{6.2}$$

where X and Y are the observed properties.

Correlation coefficients were computed between changes in bed elevation from the previous tide's survey (Δz) and: (1) the mean grain size (MGS), (2) the change in mean grain size from the previous survey (ΔMGS), (3) the mean grain size observed during the previous survey (MGS$'$), and (4) the change in bed elevation from the preceding time step ($\Delta z'$). Correlation coefficients between hydrodynamic parameters, bed level, and mean grain size were also computed. Statistical significance was evaluated based on whether confidence intervals contained zero at an $\alpha = 0.05$ significance level.

The Δz, $\Delta z'$ correlations were carried out based on the assumption that changes in bed level represent, on average, deviations from the mean profile. In other words, a positive Δz value is indicative of a topographic high at a given location, relative to the mean profile.

This correlation is susceptible to negative bias if noise levels are high relative to the actual topographic change. It can be shown using a synthetic series of Gaussian noise that the Pearson correlation coefficient of the series with itself at the previous index approaches -0.5 for a large number of samples. The RTK GPS is taken to be accurate to within ± 0.02 m in the z-direction. With the exception of points surveyed above the HWL, the distribution of Δz values for a given survey generally exceeded the expected distribution of values due to instrument inaccuracy alone. As verification, correlation coefficients between Δz and $\Delta z'$ were computed for stations landward of the HWL. These were found not to be significantly different from zero, suggesting that the potential for negative bias at stations seaward of the HWL – where the range of true Δz values would be expected to be larger – is low.

Because the distribution of mean grain sizes had a characteristic structure in the across-shore direction (coarser sediments at, and shoreward of, the berm region), only data from the longshore transects were cross-correlated (i.e., LT1, LT2, and each of the six rows of DG), to obtain meaningful correlations. In order to carry out correlations with large numbers of samples, Δz and ΔMGS observations for each longshore transect were combined, with their means removed at each tide step, and correlations carried out with the combined data sets. In other words, beach-scale changes in bed volume and mean grain size that may have resulted from, e.g., high energy forcing events, were removed, leaving only variations in longshore space relative to the mean of each transect.

Measures for which subtracting the longshore spatial mean would be less meaningful, i.e., MGS and MGS$'$, were correlated with Δz only for individual tides, and not combined. This treatment also omits large scale changes in bed level or mean grain size from tide to tide, instead emphasising spatial variations in the longshore direction.

Temporal correlations were carried out between bed level, grain size, and hydrodynamic parameters by averaging the values from individual tides. Only data from the longshore survey transects were used for the bed level and grain size data. Thus,

$$\hat{r} = \frac{\sum_{t=t_0}^{T} (\overline{X} - \langle \overline{X} \rangle)(\overline{Y} - \langle \overline{Y} \rangle)}{\sqrt{\sum_{t=t_0}^{T} (\overline{X} - \langle \overline{X} \rangle)^2 (\overline{Y} - \langle \overline{Y} \rangle)^2}}, \tag{6.3}$$

where the $\hat{\cdot}$ indicates temporal correlation, $\overline{X} = \overline{X}(t)$, the spatial mean of X at tide index t, t_0 and T are the indices of the first and last tides in the sequence, and $\langle \overline{X} \rangle$ is a temporal

mean, given by

$$\langle \overline{X} \rangle = \langle \overline{X(t)} \rangle = \frac{\sum_{t=t_0}^{T} \overline{X(t)}}{T - t_0}, \tag{6.4}$$

where $T - t_0 + 1$ is the total number of contiguous tides.

6.2.4 Wave Parameter Estimation

Data from the pressure transducer deployed near the neap low water line were processed in 12 min segments to compute standard wave statistics: significant wave height, H_s, computed as $4\sigma_p$ with σ_p being the square-root of the variance of the pressure time series; and the peak wave period, T_p, corresponding to the location in inverse frequency space of maximum spectral density in the pressure spectrum.

The 'deep water' wave steepness H_0/L_0 was computed to help draw a distinction between forcing states leading to an energetic shore break ($H_0/L_0 > 0.01$, $H_s > 0.5$ m) and more reflective conditions characterised by collapsing- or surging-type wave breaking ($H_0/L_0 < 0.01$) more typically associated with the formation of a berm, cusps, or other patterned bed states at Advocate Beach. In the wave steepness calculation, the deep water wave height, H_0, was taken to be equivalent to H_s, and the deep water wavelength, L_0, was computed using the linear surface gravity wave dispersion relation at the frequency of peak forcing ($= 1/T_p$).

6.3 Results

6.3.1 Overview of Forcing and Response

A summary of the forcing conditions during the Advocate 2018 experiment is presented in Fig. 6.2. The experiment was conducted during a transition from neap to spring tides, with the tidal range increasing from *ca*. 7.5 m at the outset to 11 m by the end of the experiment. The majority of tides were characterised by high steepness, wind-band incident waves leading to an energetic shorebreak. Sample energy spectra from high and low energy days are shown in Fig. 6.3.

The transition between neap and spring tides had important implications for the swash zone morpho-sedimentary processes: most notably, the presence of a coarse-grained high tide berm which persisted during fairweather conditions, migrating landward throughout

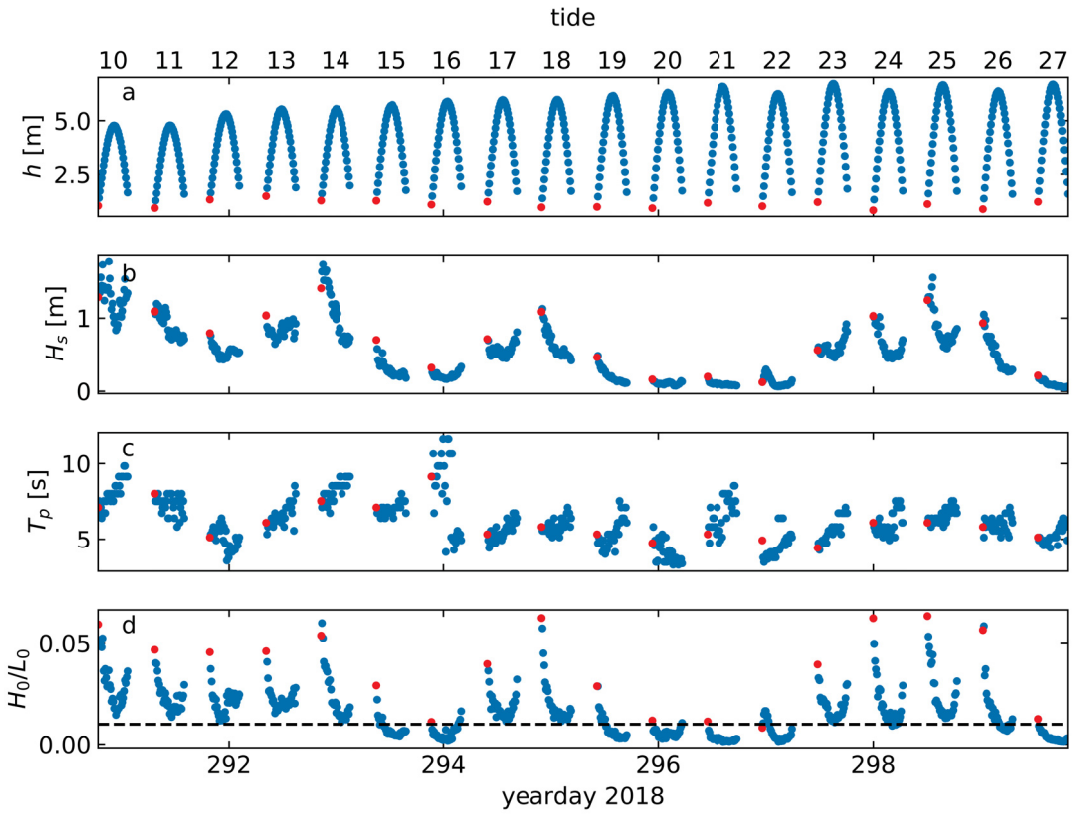

Figure 6.2: Summary wave data from the Advocate 2018 experiment. (a) Height of water, h, above the pressure transducer. (b) Significant wave height. (c) Peak wave period. (d) Wave steepness. The red dots indicate first data points of each tide.

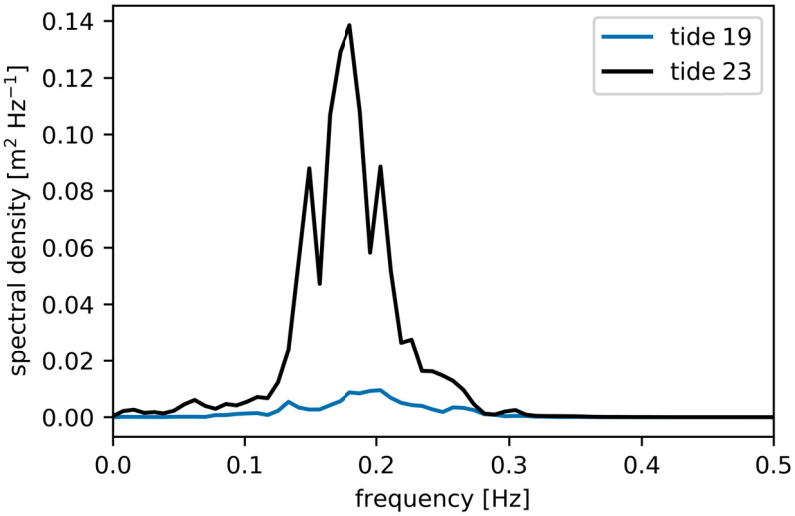

Figure 6.3: Sample energy spectra for characteristic low energy (tide 19; blue) and high energy (tide 23; black) forcing days, computed using pressure data from the low tide frame-mounted pressure transducer.

the experiment. A second, inactive spring tide berm was also present throughout the experiment (Fig. 6.4). Throughout this chapter, use of 'berm region' is in reference to the region extending from the high water line to the base of the seaward face of the active high tide berm, where a natural break in the morphological and sedimentary profiles (positive to near zero-valued Δz, and decreased MGS in Fig. 6.4) separated the berm from the remainder of the intertidal zone. The intertidal zone seaward of the berm region is hereafter referred to as the 'mid-intertidal zone'.

The beach surface sediments were generally coarser near, and landward of, the high tide shoreline, the coarsest sediments corresponding to the nominal position of the active berm (Fig. 6.5). On average, the mean grain sizes were finer in the intertidal zone seaward of the berm region. Note that the extent of the cross-shore profiles included in Figs. 6.4 and 6.5 represents only approximately one third of the full intertidal beach profile. In general, the grain size distribution became coarser near the low water shoreline, being characterised by a mixture of coarse sand and cobble- and boulder-sized material (not represented in the included data).

Fig. 6.4 shows the change in bed elevation and mean grain size for the cross-shore survey profile over all the tides that were surveyed consecutively (tides 14-27). The shoreward

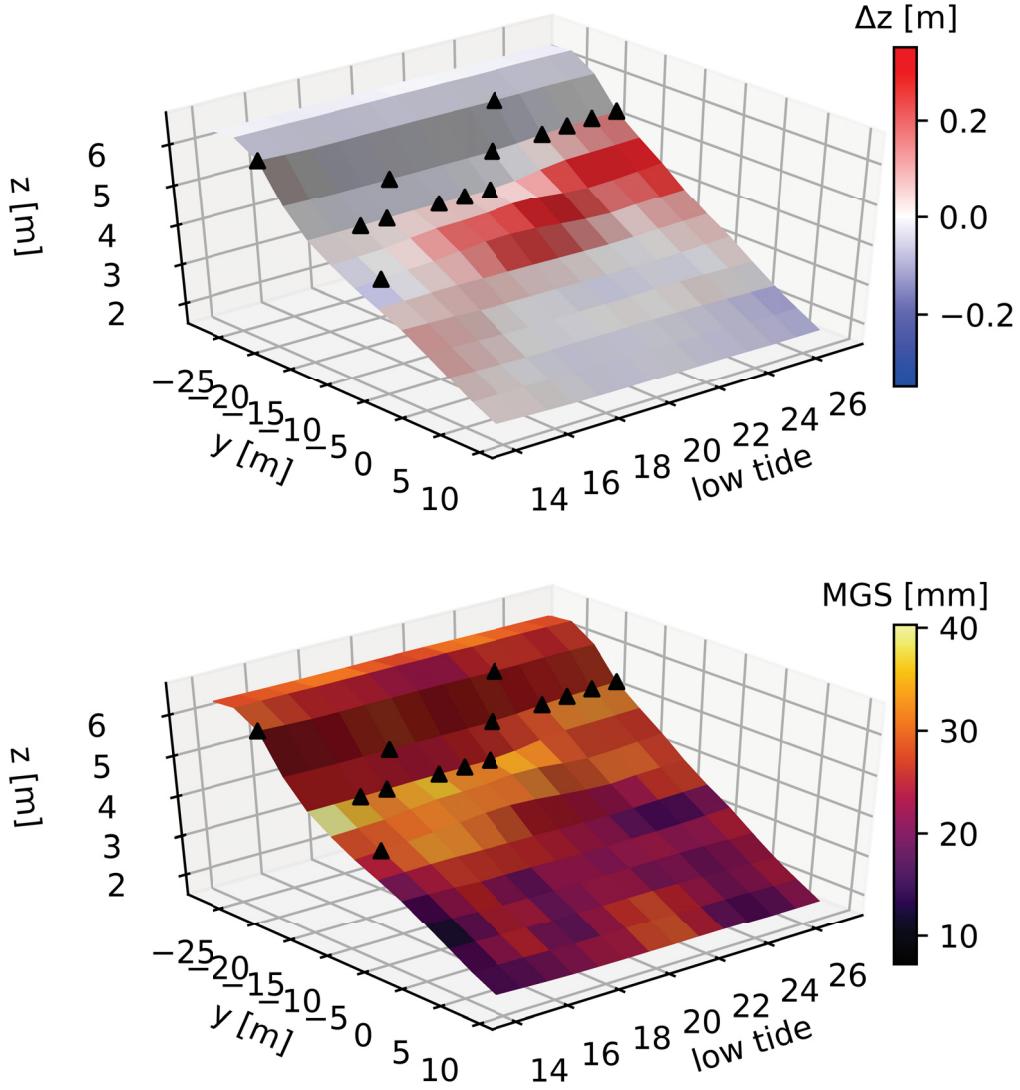

Figure 6.4: Beach morpho-sedimentary profile evolution, recorded each low tide between tides 14 and 27 on the cross-shore survey transect (CT). (a) Cumulative change in bed elevation from RTK GPS observations. (b) Mean grain size from photographs of the bed surface. Black triangles represent the estimated cross-shore coordinate of the high water line.

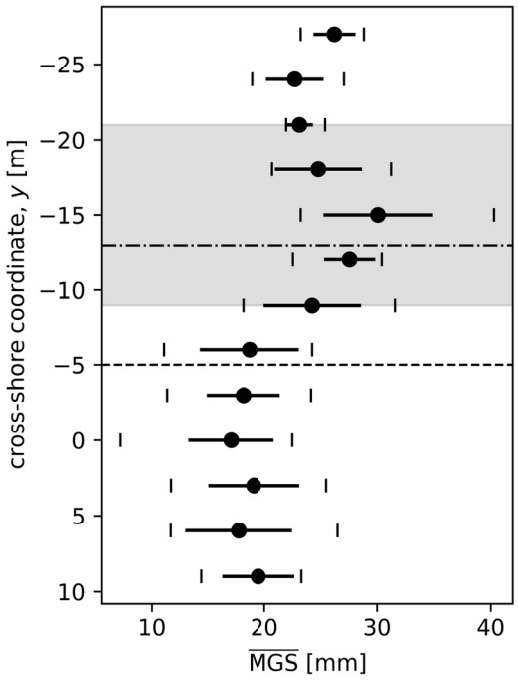

Figure 6.5: Profile of mean grain size, computed at each station in the cross-shore survey transect (CT) averaged over tides 14-27. The horizontal black lines indicate the standard deviation of the mean grain size over time, and the vertical lines indicate the minimum and maximum mean grain size at each cross-shore station. The grey-shaded region encompasses the range of high water line values during the experiment. The cross-shore coordinates of the two longshore survey transects, LT1 and LT2, are indicated by the dashed and dash-dotted lines, respectively.

migration of the high tide berm is visible, and shows the greatest morphological relief nearer the end of the experiment. Coarser grain sizes correspond to the landward extent of the high tide berm, which also generally corresponded to the HWL. The distribution of coarse and fine surficial sediments in the mid-intertidal zone displayed some spatial structure, though this structure did not persist from tide to tide. In the upper intertidal zone, within *ca*. 10 m seaward of the HWL, coarse and fine sediment 'patches' occasionally appeared to persist for longer (i.e., multiple tides). Unlike the previous experiments at Advocate Beach, there were no instances of well-defined cusp formation during the 2018 field experiment.

A wide variety of features were observed within the mid-intertidal zone. In general, the features had low morphological relief (*ca*. 5 cm maximum), and were more identifiable as coherent but disorganised sedimentary structures, which manifested as irregular alternating bands of coarse- and fine-grained sediments along- or across-shore, grain size 'patchiness', or larger undulations in morphology and grain size along- or across-shore. Some examples of these features are shown in Fig. 6.6.

6.3.2 Correlation Results

The mean grain size data from the mid-intertidal zone beach face are strongly anti-correlated with significant wave height, with wide-scale beach fining being observed following energetic wave conditions. Time series of the mean significant wave height and spatially-averaged mean grain size, $\overline{\mathrm{MGS}}$, for each tide are shown in Fig. 6.7 using grain size values from the most seaward longshore survey transect, LT1. The Pearson correlation coefficients computed between the mean grain size and mean wave statistics are listed in Table 6.1. The spatially averaged mean grain sizes are highly correlated with both the significant wave height ($\hat{r} = -0.79$) and the deep water wave steepness ($\hat{r} = -0.84$). Scatter plots of the spatially-averaged mean grain size versus the mean significant wave height and mean wave steepness, shown in Fig. 6.8, indicate that both relationships are well-described as linear under low to moderate energy forcing conditions (e.g., $H_s < 0.5$ m, $H_0/L_0 < 0.017$), but with an apparent threshold forcing value above which the spatially averaged mean grain size exhibits greater variability. The values of the correlation coefficients for both $\overline{\mathrm{MGS}}$ and mean significant wave height, and $\overline{\mathrm{MGS}}$ and mean wave steepness are not significant at the $\alpha = 0.05$ level if computed using data from the more shoreward survey transect, LT2.

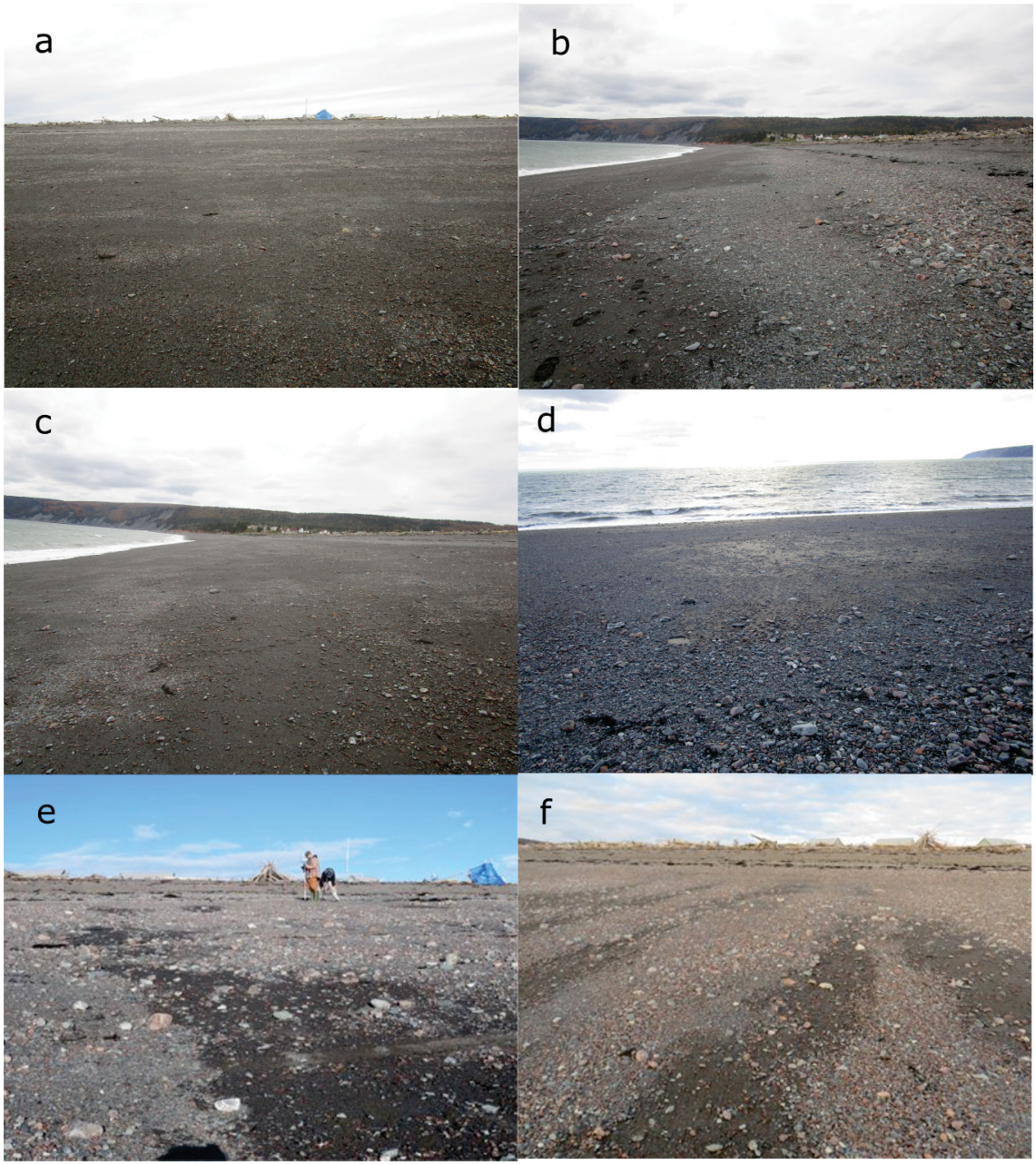

Figure 6.6: Photographs of features exhibiting grain size segregation at Advocate Beach during low tide 11 (a,b,c), 16 (d), 17 (e), and 19 (f).

Table 6.1: Temporal correlation coefficients, $\hat{r}$, between spatial averages of mean grain size along the indicated transect, $\overline{\mathrm{MGS}}$, and wave forcing parameters.

correlates	survey transect	$\hat{r}$	95% confidence interval
$\overline{\mathrm{MGS}}$, $4\sigma_p$	LT1	-0.79*	(-0.39, -0.94)
$\overline{\mathrm{MGS}}$, T_p	LT1	0.04	(-0.55, 0.60)
$\overline{\mathrm{MGS}}$, H_0/L_0	LT1	-0.84*	(-0.51, -0.95)
$\overline{\mathrm{MGS}}$, $4\sigma_p$	LT2	-0.24	(-0.70, 0.36)
$\overline{\mathrm{MGS}}$, T_p	LT2	0.08	(-0.60, 0.49)
$\overline{\mathrm{MGS}}$, H_0/L_0	LT2	-0.24	(-0.70, 0.36)

* Statistically significant at the $\alpha = 0.05$ level.

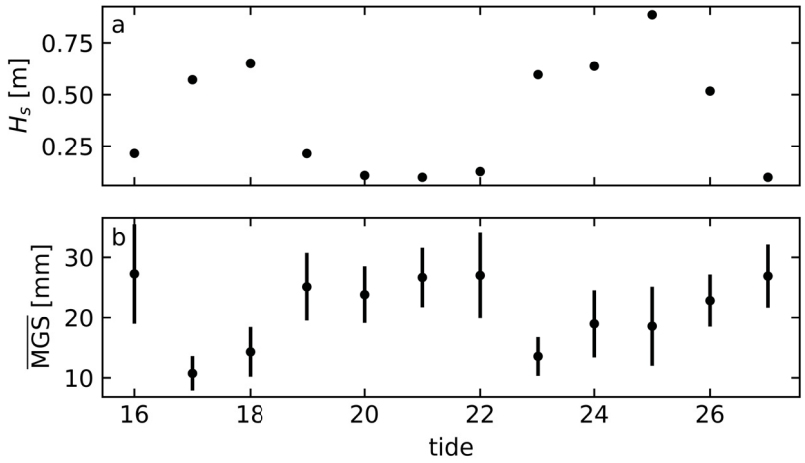

Figure 6.7: Time series of mean significant wave height and $\overline{\mathrm{MGS}}$ for transect LT1.

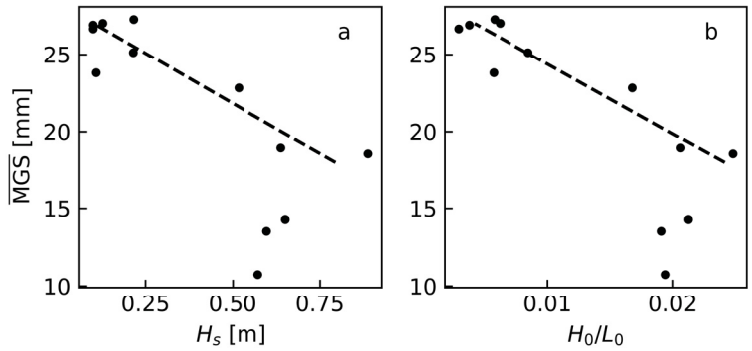

Figure 6.8: Scatter plots of the spatially averaged mean grain size $\overline{\mathrm{MGS}}$, computed over the seaward-most longshore survey transect LT1 for each of the surveyed tides, versus (a) the mean significant wave height H_s and (b) the deep water wave steepness H_0/L_0.

Table 6.2: Spatial correlations, r, between changes in bed level, Δz, and changes in mean grain size, ΔMGS.

survey transect	r	95% confidence interval
LT1	0.37*	(0.27, 0.47)
LT1 ($H_0/L_0 < 0.01$)	0.36*	(0.22, 0.49)
LT1 ($H_0/L_0 >= 0.01$)	0.39*	(0.25, 0.52)
LT2	0.16*	(0.05, 0.26)
LT2 ($H_0/L_0 < 0.01$)	0.06	(-0.08, 0.21)
LT2 ($H_0/L_0 >= 0.01$)	0.30*	(0.15, 0.44)

* Statistically significant at the $\alpha = 0.05$ level.

Fig. 6.9 shows scatter plots of all bed level change, Δz, and mean grain size change, ΔMGS, observations between tides 14 and 27, for LT1, the most seaward longshore transect, and LT2, the longshore transect roughly corresponding to the mean position the high tide berm. A positive correlation is apparent in the LT1 data ($r = 0.37$). Little visually discernible correlation is evident from the LT2 data ($r = 0.16$), though the correlation increases significantly if only examining tides characterised by high steepness waves. A summary of the spatial correlations between changes in bed level and mean grain size is presented in Table 6.2. The correlation output for the LT2 data is nearly identical if stations landward of the HWL are omitted from the analysis (true only for tide 16; see Fig. 6.4).

A summary of the correlation coefficients between Δz and ΔMGS for each of the longshore transects is shown in Fig. 6.9. The correlation values increase positively with increasing distance to seaward. The strongest correlations are associated with LT1 – the seaward-most longshore transect. The correlation coefficient values are not significantly different from zero for transects located landward of the nominal HWL.

Correlation coefficients associated with data from individual tides are shown in Fig. 6.10, for LT1 and LT2. Since these correlations were limited by the number of samples in the survey transect, few of the results are statistically significant at the $\alpha = 0.05$ level; however, there are some notably consistent trends. Similar to the correlation results above, higher correlations are evident for data from the seaward-most survey transect. From the LT1 data, the correlation coefficients between Δz and MGS, and between Δz and ΔMGS were consistently positive, having centroid values that are commensurate with the longer-term correlation results (Fig. 6.9), which have higher degrees of statistical significance. With two exceptions, the correlation coefficients between Δz and the mean grain size observed at the previous low tide, MGS$'$, were negative, having a centroid value of $r \approx -0.2$. The

Table 6.3: Average mean grain size (MGS) for three different classes of bed-level change: accretion, no change, and erosion associated with the most seaward longshore survey transect, LT1. The number of occurrences for each class, N, is also indicated.

bed state	mean size (mm)	N
accretion	25.7 ± 6.7	57
no change	20.7 ± 7.5	165
erosion	19.6 ± 7.5	90

correlation of Δz with Δz from the previous low tide, $\Delta z'$, was consistently negative, with a centroid value of $r \approx -0.5$. The centroid values of the correlation coefficients associated with LT2 exhibit similar trends, though are closer to zero and have a higher degree of variation.

With the exception of the strong anticorrelation between $\overline{\mathrm{MGS}}$ and the significant wave height, comparisons between $\overline{\Delta z}$, $\overline{\mathrm{MGS}}$, and mean wave forcing parameters (wave height, peak period, sea-band wave energy, and steepness) did not yield any statistically significant temporal correlations or clear visual trends. The potential influence of the wave forcing on the spatial correlation between Δz and ΔMGS (Fig. 6.9) was investigated using data from LT1 by separating tides characterised by high wave steepness forcing, $H_0/L_0 > 0.01$, from those characterised by low steepness forcing, $H_0/L_0 < 0.01$, and carrying out the correlation computations on each. A steepness value of 0.01 is often used to demarcate accretive from erosive conditions (e.g., *Masselink et al.*, 2007). The correlation coefficients are nearly identical for both datasets: $r = 0.39$ with a 95% confidence interval of (0.25, 0.52) for the high steepness set, and $r = 0.36$ in (0.22, 0.49) for the low steepness set. The result is comparable when a significant wave height threshold is used instead (threshold values of $H_s = 0.5$ m and 0.2 m were tried).

The data from LT1 were also analyzed following the method of *Masselink et al.* (2007) to facilitate comparison with their results. Bed level change (Δz) at each survey station was classed as accretion ($\Delta z \geq 0.02$ m), no change ($-0.02 < \Delta z < 0.02$ m), or erosion ($\Delta z \leq -0.02$ m). The mean and standard deviation of the MGS associated with the Δz instances were computed for each of the three categories. The results are listed in Table 6.3. The trend of change in MGS was examined by tabulating the proportion of fining ($\Delta\mathrm{MGS} < 0$) versus coarsening ($\Delta\mathrm{MGS} > 0$) instances within the accretion and erosion categories. As summarised in Table 6.4, surficial sediment coarsening occurred during 86% of the instances of accretion, and fining occurred during 56% of the erosion instances.

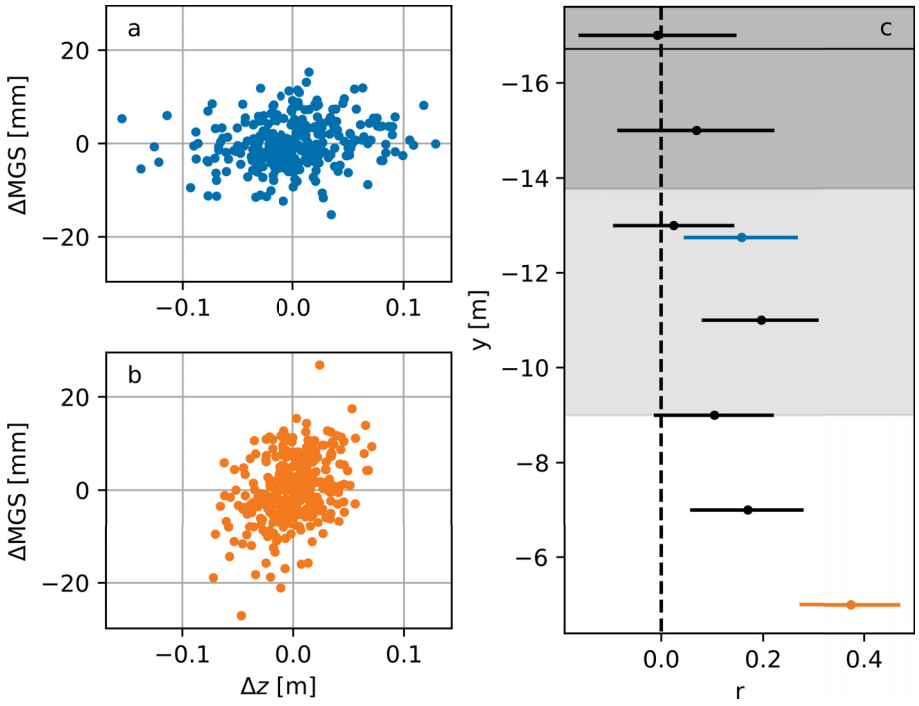

Figure 6.9: Scatter plots of the change in bed level (Δz) versus the change in mean grain size (Δ MGS) using data from: (a) longshore survey transect LT2, corresponding roughly to the time-averaged cross-shore location of the high tide berm ($r = 0.17$, with a 95% confidence interval of (0.06, 0.27)); and (b) longshore survey transect LT1, the most seaward survey transect, positioned down-slope of the nominal berm location, in the mid-intertidal zone ($r = 0.38$, 95% confidence interval of (0.28, 0.47)). The data from all consecutively surveyed low tides are shown, with the mean subtracted from both Δz and ΔMGS for each tide time step. (c) Pearson correlation coefficients for Δz and ΔMGS for all of the longshore survey transects, i.e., LT1 (yellow), LT2 (blue), and each of the six longshore transects comprising the densely surveyed grid, DG (black). The correlations are based on all samples collected on each of the eight longshore transects throughout the experiment, with tide-specific means removed. The tails indicate 95% confidence intervals. The horizontal black line, dark grey-shaded region, and light grey-shaded region indicate the respective mean, standard deviation, and range of the cross-shore coordinate of the high water line over the 13 tides. Note that the $y = -13$ m coordinate was sampled twice: i.e., both LT2 and the third-most shoreward transect of DG.

Table 6.4: Occurrence counts and occurrence ratios, in parentheses, between morphological response and change in mean sediment size for the accretion and erosion classes of bed level change associated with the most seaward longshore survey transect, LT1.

bed state	finer	coarser	N
accretion	8 (0.14)	49 (0.86)	57
erosion	50 (0.56)	40 (0.44)	90

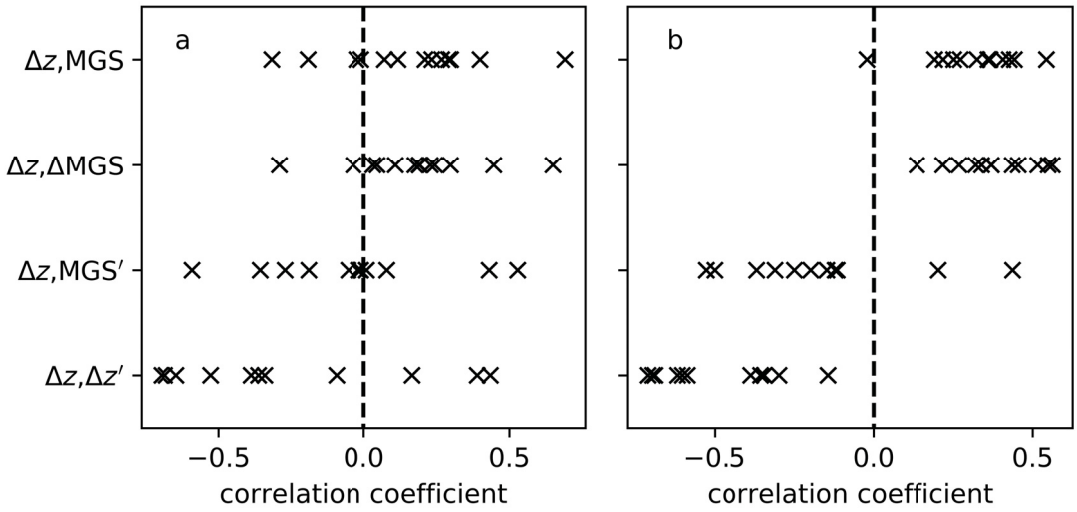

Figure 6.10: Pearson correlation coefficients, r, associated with longshore survey transects (a) LT2, and (b) LT1. The correlations are between bed elevation change (Δz) and: mean grain size (MGS), the change in mean grain size (ΔMGS), the mean grain size observed during the previous survey (MGS$'$), and the change in bed elevation observed during the previous survey ($\Delta z'$). Each 'x' represents the correlation coefficient for data from the given survey transect for a single tide.

6.4 Discussion

The morpho-sedimentary evolution of a mixed sand-gravel beach was investigated over 14 consecutive tidal cycles at the scale of the intertidal zone (O(10-100) m), through bed level and photographic grain size sampling over a fixed survey grid during low tide when the intertidal zone was exposed. The forcing conditions were dominated by steep, wind-band incident waves leading to an energetic shore break, interspersed by periods of low steepness wave incidence and berm building (Figs. 6.2 and 6.4).

6.4.1 Response of Surficial Sediments to Varying Wave Forcing

The time series of spatially-averaged surficial sediment grain size in the mid-intertidal zone indicates a clear dependence on the significant wave height and wave steepness (Fig. 6.7). High wave energy conditions resulted in surficial sediment fining across the intertidal zone, and low energy conditions resulted in bed surface coarsening. This result is counter-intuitive in the context of our broader understanding of (especially sand) beach response to changes in forcing (e.g., *Bascom*, 1951; *Masselink et al.*, 2007). However, this response has been previously observed at Advocate Beach (*Hay et al.*, 2014), as well as at other MSG sites reported on in the literature (*Nordstrom and Jackson*, 1993; *Pontee et al.*, 2004; *Curtiss et al.*, 2009; *Miller et al.*, 2011). Typical forcing conditions and beach characteristics for each of the sites reported in the literature are summarised in Table 6.5. Like Advocate, all of these beaches are steep, with slopes of at least 1:10.

Table 6.5: Summary of studies from the mixed sand-gravel beach literature reporting fining of beach surface sediments during periods of high energy wave forcing.

study	location	tide range	slope ($\tan \beta_s$)	wave height; period
Nordstrom and Jackson (1993)	Delaware Bay, USA	1.6 m	0.11	> 0.5 m (high energy); NA
Pontee et al. (2004)	3 sites in East Anglia, UK	2-3 m	0.10-0.15	0.4-0.5 m (annual); *ca.* 6 s
Curtiss et al. (2009)	Puget Sound, WA, USA	3.5 m	0.14-0.20	0.10-0.24 m (during 4 storms); 1-3 s
Miller et al. (2011)	Juan de Fuca Strait, WA, USA	1.4 m	0.12-0.13	0.47 m (6 month); 4 s (wind)
Hay et al. (2014)	Advocate Beach, NS, CA	10 m	0.12	0.3-0.5 m; 4-6 s

The relationship between wave forcing and mean surface grain sizes is far from clear. For example, though *Pontee et al.* (2004) observed an inverse correlation between mean grain size and wave height in general, they only claimed statistical significance of the result at one of their three study sites, and in some cases observed an opposite response. It is interesting to note that all of the sites described above experience some degree of wave energy limitation; the sites studied by *Pontee et al.* are the only ones which face the open ocean, though the wave energy is limited by a series of offshore sand bars. The sites listed in Table 6.5 span a wide range of tide regimes, from micro- to megatidal. The similarities and differences between the sites may provide some insight into the mechanisms for fining during more energetic wave forcing, about which a range of explanations have been proposed: *Pontee et al.* suggested that onshore transport of sand from the nearshore region during periods of post-storm swell could explain the sandy characteristics of post-storm profiles at two of their beaches. They also suggested that intertidal fining could be a result of larger particles being concentrated in the berm and step. *Curtiss et al.* noted that the observed surficial fining during storm conditions is consistent with a 'reverse winnowing' process, wherein larger particles are selectively removed from the bed as a result of enhanced mobility. *Miller et al.* noted that the increase in sand visible at the bed surface following high waves was suggestive of thorough mixing of the beach substrate. At Advocate Beach, during highly energetic wave conditions and on the rising tide, *Hay et al.* observed the formation of metre-scale wave orbital ripples with ripple crests built of fine sediments and ripple troughs containing a coarse sediment lag. These ripples were not present on the exposed beach face after the subsequent ebb tide, the beach surface instead being both planar and covered with a thin layer of fine material. *Hay et al.* attributed this fining of the beach face sediment to the ripple crests being planed off by the swash during the falling tide, burying the coarser-grained material in the troughs.

Past observations of the grain size distribution at Advocate Beach have indicated that the sediments beneath the surficial layer remain well-mixed, regardless of the forcing conditions, suggesting that the surf and swash zones can be approximately considered as a closed sedimentary unit. Thus, the mechanisms suggested by *Pontee et al.*, and *Curtiss et al.*, involving removal of sediments from the beach face to the nearshore, or vice versa, do not seem likely at the Advocate site. The factor of 10 differences among the tidal ranges listed in Table 6.5 suggests, given the factor of only 2 differences in slope, that cross-shore

translation of the shoreline may not be a requirement for beach surface fining in response to energetic waves. The implication is that beach surface fining in response to energetic waves is primarily a swash zone process. The process may be influenced by, while not being dependent upon, morphodynamic processes in the surf zone, as required for the *Hay et al.* ripple planing mechanism.

The following alternative mechanism is proposed (see the accompanying schematic in Fig. 6.11): During periods of high energy wave forcing, the swash zone increases from its characteristic width of O(1 m) during fairweather forcing to a width of O(10 m). Mobilisation of all grain sizes occurs following bore collapse at the shorebreak; gravel- and cobble-sized particles, which are typically transported through rolling, sliding, or occasional saltation (*Carter and Orford*, 1984), are deposited earlier in the uprush phase, making them susceptible to remobilisation during the downrush phase. The sand size-fraction is transported shoreward as suspended load. The lower settling velocity of sand-sized particles in suspension contributes to a larger settling lag – the time required for suspended particles to settle to the bottom through slowly flowing water (*Masselink and Puleo*, 2006) – meaning the finer particles are deposited later in the swash uprush phase. Increased infiltration near the landward edge of the swash zone, due to the swash surpassing the water table exit point, contributes to the deposition of any material still in saltation or suspension. The result is the deposition of a layer of finer-grained material near the shoreward-edge of the swash zone, atop the more well-mixed substrate. During fairweather forcing, the shorebreak and swash zone are more closely coupled. Mobilisation of most grain sizes occurs following bore collapse, with gravel- and cobble-sized particles being transported primarily through rolling. The coarse-grained particles may remain mobile due to rejection by the finer substrate leading to overpassing, or may be deposited near the landward- or shoreward edge of the swash zone. The sand-sized fraction may be transported via saltation and some suspended load. Unlike in the energetic forcing case, the characteristic transport range of the coarser particles is of the same order as the swash zone width, meaning the settling leg mechanism for surficial fining is not effective (note Fig. 5.2 in Chapter 5 as an exception to this, where fine-grained material was deposited landward of cusp bays during fairweather forcing). The tendency for gravel- and cobble-sized particles to propagate shoreward due to swash velocity asymmetry has been acknowledged elsewhere (*Carr*, 1983). The sequences described above are independent of shoreline

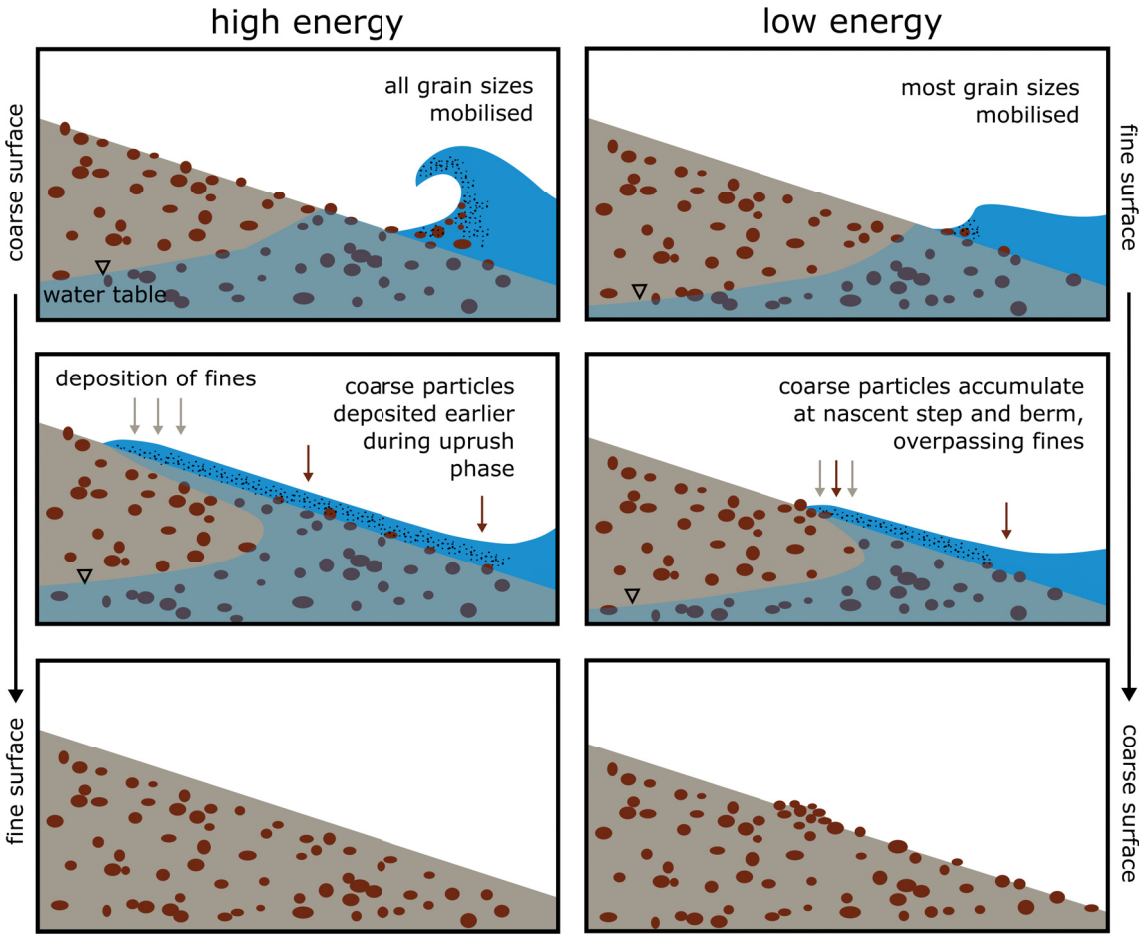

Figure 6.11: Schematic description of the proposed mechanisms leading to surficial sediment fining during energetic wave forcing (left) and surficial sediment coarsening during fairweather wave forcing (right).

translation induced by tides. However, tides may serve to visually reinforce the signatures of the mechanisms described above on the beach face, since the beach surface coarsening or fining associated with the leading edge of the swash is spread over the subaerial intertidal zone following the translation of the shoreline during ebb tide. Furthermore, the presence of a nascent coarse-grained beach step during fairweather forcing, or metre-scale wave orbital ripples with fine-grained crests during energetic forcing (see *Hay et al.*, 2014), may provide source regions of coarse-grained and fine-grained particles, respectively, during ebb tide. Note also that the surficial fining and coarsening mechanisms proposed above are a result of local processes, i.e., they do not require an exchange of material between the surf- and swash zones.

The proposed surficial fining mechanism is similar to the beach recovery mechanism described by *Bramato et al.* (2012) on a MSG beach following a storm-associated erosion event, in which, during periods of accumulation, the longer suspension time of the finer sediments causes them to be deposited in a layer atop the coarser sediments. However, their mechanism is associated with fairweather forcing, offshore transport of sand and beach surficial coarsening being associated with erosive storm conditions.

The data presented in Fig. 6.8 are suggestive of a threshold set of forcing conditions, below which the relationships between the spatially averaged mean grain size and both the significant wave height and the wave steepness appear linear, and above which the mean grain size displays a higher degree of variability. Two potential explanations are suggested: (1) The stranding of coarse-grained material at the leading edge of the swash zone, i.e., the proposed surficial sediment coarsening mechanism associated with fairweather forcing, is a more effective and consistent grain size sorting mechanism than the surficial fining process associated with energetic forcing. In other words, the continued presence of coarse-grained particles on the beach surface following energetic forcing conditions, despite the fining of the beach surface sediments in a mean sense, results in a broader surficial grain size distribution following energetic forcing that is more variable in space for a given tide, and consequently also exhibits more variation among different tides. (2) The low variability of spatially averaged mean grain size estimates following fairweather forcing and the higher variability associated with energetic forcing is an artefact of the digital grain sizing methodology. The validated best-fit parameter set used in the digital grain sizing algorithm underestimates mean grain sizes above *ca.* 20 mm (see Appendix B). This may result in an effective 'ceiling' on the mean grain size estimates causing the larger grain size estimates to appear more closely grouped than the finer mean grain size estimates.

There may be other site-specific mechanisms which depend upon a complicated time history of antecedent morphology, grain size, and forcing. It would be of interest to carry out a full sedimentological investigation at a MSG site that includes high resolution sampling in space (vertical and horizontal), at tidal time scales, in order to further constrain the potential mechanisms.

6.4.2 Morpho-Sedimentary Correlation at the Beach Scale

The results from Section 6.3.1 clearly indicate that a spatial correlation exists between changes in bed level and mean surface grain size. Though the existence of this correlation

is perhaps unsurprising given the acknowledged influence of bed texture on near-bed hydrodynamics and the prevalence of grain size sorting and pattern formation on MSG beaches, it has been difficult to establish in other cases. Indeed, similar studies by *Masselink et al.* (2007) and *Austin and Buscombe* (2008) found little evidence of correlation between morphological and grain size responses on coarse sand and gravel beaches, respectively. *Masselink et al.* sampled bed elevation and grain size over a *ca*. 100 m cross-shore transect, over 40 tidal cycles. In most cases, they reported no correlation between bed level change and mean grain size or sorting, with the exceptions of coarse sediment patches near the beginning and end of their study which were associated with net erosion (i.e., correlations with opposite sign to those presented here) and decreases in sorting. In their gravel beach study, *Austin and Buscombe* (2008) collected coincident observations of bed level, using manual surveying, and grain size from imaging methods. They observed some positive correlation between bed level change and mean grain size at the position of the berm and beach step, though a clear relationship was not otherwise observed.

A notable difference between Advocate Beach and the sites investigated by *Masselink et al.* (2007) and *Austin and Buscombe* (2008) is the much wider grain size distribution at Advocate: i.e., from less than 1 mm to greater than 200 mm at Advocate compared to coarse sand, $0.5 <$ MGS < 1.0 mm; and pure gravel, $5 <$ MGS < 20 mm. The presence of combined sand and gravel fractions has dynamical implications for sediment transport (e.g., *Wilcock and McArdell*, 1993, 1997; *Wilcock and Crowe*, 2003), and may enhance morpho-sedimentary feedbacks leading to pronounced size-segregated pattern formation (e.g., *Longuet-Higgins and Parkin*, 1962; *Guest and Hay*, 2019).

The correlation coefficients are highest for data sampled farthest to seaward of the high water line. There are two reasons why this might have been the case. The first is that five of the eight longshore survey transects were above the HWL for at least one survey. Omitting above-HWL data does little to change the correlation results, indicating that sediments at or near the HWL (interpreted as the swash runup maximum) were not acted upon by sufficient swash energy for a signal to emerge. This is supported by the notable increase in the correlation coefficient between Δz and ΔMGS at the more shoreward LT2 transect during high wave steepness forcing, when the swash zone width would have been greater. A different shoreline metric, e.g., the mean swash runup limit, might therefore be a more appropriate boundary. The second reason is that the beach surface near the nominal high

water shoreline was typically characterised by the coarse sediments – gravel and cobbles – associated with the berm region. This coarse material near the HWL persisted through time (see Fig. 6.4), migrating with the high tide shoreline during the neap-spring tide cycle. Conversely, the beach surface in the mid-intertidal zone, seaward of the berm region, was typically finer-grained with a greater degree of temporal variability. It seems likely that the inherent short-term variability of the bed level and mean grain size in the mid-intertidal zone, along with the presence of a more well-mixed surficial grain size distribution, was more conducive to the emergence of an observable signal.

6.4.3 Feedback Mechanisms

At Advocate Beach, and on steep energetic beaches in general, the shorebreak does considerable reworking of the surficial sediments. This serves as a mechanism for morphological 'smoothing', wherein features in the intertidal sediments are eradicated, particularly during periods of moderate- to high-energy wave forcing. The morphological smoothing implied by the negative correlation between changes in bed elevation from one tide to the next (Δz and $\Delta z'$) is therefore unsurprising (consider, for instance, footprints in intertidal sand). More interesting is that the smoothing response of the mean grain size is similar – the correlation between changes in bed elevation and the mean grain size from tide to tide (Δz and MGS$'$) also being negative – suggestive of the close linkage between spatial changes in morphology and grain size.

The positive correlations between changes in bed level and mean grain size (Δz and MGS) and changes in bed level and changes in mean grain size (Δz and ΔMGS) at the beach surface can be explained in terms of mutually reinforcing feedbacks between flow, morphology, and the surficial grain size distribution. In the ebb-tide swash zone, emerging coarse patches enhance deposition: of fine material through kinetic sieving (effectively removing the fine particles from the beach surface), and of coarse material through grain interlocking and increased angles of pivot required for mobilisation. Away from the berm region, where sediments tend to remain coarse, it is logical that where grain sizes are large, there has been an increase in mean grain size (e.g., from the time-averaged mean). Conversely, coarse-grained topographic highs or fine-grained lows which form on the mid-intertidal beach face during the previous ebb tide are subjected to the destructive influence of the translating shorebreak during the subsequent flood. The result is the formation of transient morpho-sedimentary features throughout the mid-intertidal zone

that form in the ebb tide swash, but which do not persist for longer than one tide. These transient features might manifest as grain size 'patchiness', or alternating bands of coarser- and finer-grained sediments with long- or cross-shore structure (see Fig. 6.6). *Buscombe and Masselink* (2006) described similar features as 'textural mosaics' which act as textural surrogates to morphological bedforms, the effect of texture on the nearbed flow being considered in terms of its 'hydraulic equivalence' to morphological patterning.

Stations surveyed near the HWL may be associated with different morpho-sedimentary processes (e.g., berm, cusp formation) than the mid-tide beach face, and may not be acted upon by the translating shorebreak. At the high tide shoreline, the mechanism for mobilising and transporting accumulations of coarse grains (i.e., swash) is weakened through hydraulic drag and infiltration, increasing the likelihood that a morphological feature would persist through successive tides.

6.4.4 Implications for Cusp Formation

The conspicuous lack of well-developed beach cusps during the 2018 Advocate Beach experiment is in contrast to previous experiments at Advocate Beach. It is proposed that the reason for this is related to the timing of the experiment within the spring-neap cycle: i.e., the range of days over which data were collected corresponded to the transition from neap to spring tides (see the water column heights registered by the pressure sensor, Fig. 6.2), as noted in Section 6.4.2. As a result, a coarse-grained high tide berm consistently coincided with the high water line (see Fig. 6.4) – at least during tides characterised by low- to moderate energy wave forcing, when cusps might have otherwise been expected to emerge. The coarse-grained berm migrated shoreward with the translation of the high tide shoreline.

As suggested by the results of the correlation analysis, the coarse-grained berm region was less conducive to the evolution of spatially correlated morphological and sedimentary features than the more well-mixed mid-intertidal zone. A wide surficial grain size distribution promotes the rapid emergence of beach cusps; where a narrower range of surficial grain sizes exists, the variation in space of textural feedbacks on the flow is less pronounced, and the emergence timescale of features is much longer, or features may not form at all (Chapter 5). A well-mixed substrate was also suggested by *Longuet-Higgins and Parkin* (1962) to favour the formation of beach cusps through feedback mechanisms:

the relatively high permeability of incipient accumulations of coarse grains enhances deposition through the loss of swash energy, whereas the lower permeability of a sand-gravel mixture promotes the transport of overlying particles, since less swash energy is lost to infiltration.

6.5 Conclusions

The morpho-sedimentary evolution of a mixed sand-gravel beach was investigated at the scale of the beach profile, through the sampling of bed level and mean grain size at *ca*. 2500 points collected over 14 tidal cycles. The forcing conditions were dominated by large (˜10 m) tides and steep, wind-band incident waves leading to an energetic shore break, interspersed by periods of low steepness wave incidence and berm building.

A pronounced negative correlation between wave height and mean surficial grain size was observed. Though at odds with the prevailing understanding of sand beach grain size change in response to forcing, a similar inverse correlation has been observed at other mixed sand-gravel beach sites, under a range of forcing and tide conditions. All the studies of which the author is aware that report fining of beach surface sediments under energetic wave forcing were conducted on steep MSG beaches experiencing some degree of wave energy limitation, though the tidal regimes varied from micro- to megatidal. The large differences in tidal range among these MSG beaches suggest that interplay between surf- and swash zone processes may not be of principal importance, and the dominant mechanism may be swash-related. However, given the relative scarcity of field studies at MSG beach settings which include concurrent observations of grain size and forcing conditions over timescales of several weeks, and the implications for the prediction of sediment dynamics in these environments, this suggestion warrants further investigation.

A persistent positive spatial correlation was observed between tide-to-tide changes in bed level in the intertidal zone, and both the mean grain size and mean grain size change. Negative spatial correlations were established between bed level change and both the mean grain size observed during the previous tide, and the change in bed level observed during the previous tide. Both the positive and negative correlations were more evident in the mid-intertidal zone, seaward of the region typically occupied by the active berm. The correlation results were attributed to the formation of ephemeral morpho-sedimentary features in the ebb tide swash zone through mutually reinforcing feedbacks, and the

subsequent destruction of the features through shore-break and surf zone morphological smoothing during the following flood tide. The sign of the correlation between bed level change and mean grain size is opposite to the phenomenological relationship expected on other beach types (e.g., *Masselink et al.*, 2007). The lack of significant temporal correlations between bed level and grain size (from one tide to the next) may indicate that the sampling interval was not sufficiently short to resolve time-coherent processes that occur over timescales which are commensurate with the forcing ($O(10)$ s), or with the evolution of the morpho-sedimentary features ($O(1000)$ s).

The persistent correlation between bed level and mean grain size changes supports the suggestion that sediment characteristics reinforce morphological change (see *Buscombe and Masselink*, 2006), at least over tidal time scales.

CHAPTER 7

SWASH ZONE MORPHO-SEDIMENTARY DYNAMICS

7.1 Introduction

Inter-relationships between bed level change and sediment properties in the swash zone are difficult to establish due to the challenges inherent in obtaining observations of bed level and sediments at the time scale of the swash forcing. The application of novel *in situ* sensing techniques – based on multi-element conductivity insertion probes – has led to major advances in our understanding of swash zone sediment transport on sandy beaches (*Puleo et al.*, 2013; *Lanckriet et al.*, 2013). However, such methods are not suitable for coarse-grained beaches, where energetic shorebreaks capable of mobilising gravel- and cobble-sized grains pose a major hazard to instrumentation. Remote sensing methods provide a potential alternative. The recent application of remote sensing methods to the swash zone, including acoustic range sensors for observing bed level change (e.g., *Turner et al.*, 2008) and image-based methods capable of estimating sediment grain size (e.g., *Rubin*, 2004; *Buscombe*, 2013), has also led to some important advances in our understanding of sediment transport processes in swash flows. However, previous efforts have been largely limited to pure sand or gravel beach types, with mixed sand-gravel beaches receiving little or no attention, particularly with regard to sediment properties.

The use of ultrasonic range sensors to obtain remote observations of bed level in the swash zone has provided insight into the dynamics of beach profile change. An important result borne of swash timescale bed level monitoring throughout the last 15 years is that of the inter-swash timescale of net bed level change, wherein a tendency toward a dynamic

equilibrium profile (see *Dean*, 1991) is achieved via a balance between onshore and offshore sediment fluxes over many swash events (e.g., *Horn and Walton*, 2004; *Turner et al.*, 2008; *Masselink et al.*, 2009; *Russell et al.*, 2009; *Blenkinsopp et al.*, 2011). This is contrary to the previously prevailing notion that beach face equilibrium is the result of a balance between individual uprush and downrush events (i.e., intra-swash timescales). The use of arrays of bed level sensors has allowed for more comprehensive investigations of volume change across the beach profile, including the swash zone, than was previously possible (*Masselink et al.*, 2009; *Blenkinsopp et al.*, 2011). Studies of bed level change at swash or near-swash timescales on MSG beaches are few: *Kulkarni et al.* (2004) used a manual post-and-ruler surveying method to examine bed level change on a MSG beach at time intervals of minutes; *Horn and Walton* (2004) used a similar post-and-ruler method to measure bed level every 10-25 seconds over a three hour period encompassing high tide. They reported increases in bed elevation on the rising tide and decreases on the falling tide, with high frequency (i.e., one time step) bed level variations being nearly as large as the overall amount of bed level change. No MSG beach studies exist, to the author's knowledge, that make use of ultrasonic bed level sensors – providing sub-swash timescale observations of bed level and swash height.

Digital grain sizing methods enable the collection of grain size data non-intrusively with high temporal resolution. There are many automated methods for estimating a grain size distribution from imagery. Under the scheme proposed by *Buscombe et al.* (2010), digital grain sizing methods can be broadly classified as 'geometrical' or 'statistical'. Geometrical methods (e.g., *Chang and Chung*, 2012) employ image processing techniques (e.g., segmentation, thresholding) to identify major and minor axis lengths of individual grains. Statistical methods (e.g., *Rubin*, 2004; *Warrick et al.*, 2009; *Buscombe*, 2013) make use of time series analysis techniques (e.g. autocorrelation and Fourier or wavelet transforms) in the space domain to characterise texture in the image without attention to individual grains. Recent statistical methods (*Buscombe et al.*, 2010; *Buscombe*, 2013), which characterise the grain size distribution in terms of Fourier or wavelet derived power spectra, do not require calibration specific to a sediment population. Wavelet-based methods have the benefit of not requiring the image to be stationary or spatially homogeneous, making the method less sensitive to the number of grains in the image, their orientation, or the presence of voids (i.e., pore spaces between grains). These benefits

make the wavelet method more suitable for applications involving images of poorly sorted sediments (*Buscombe*, 2013).

Though digital imaging techniques have been applied widely across the geological sciences, few studies have applied such methods to the swash zone. The only study to do so that the author is aware of is that of *Austin and Buscombe* (2008), who used the *Rubin* (2004) method on images captured in the subaerial swash zone of a meso-macrotidal pure gravel beach. *Austin and Buscombe* used mean grain size data, collected at a minimum of 5 minute sampling intervals from both digital imagery (subaerial) and physical, grab-sampled sediments (subaqueous) to compare with bed level change from a manual, *in situ* surveying method. The extent to which the image-derived grain size data were used in their analysis is unclear. Theirs is also the only study the author is aware of in the gravel beach literature which includes simultaneous observations of bed level and sediment properties in the swash zone. Their cross-shore bed level and sediment sampling transects were separated by 2 m alongshore. *Austin and Buscombe* observed that temporal changes in the grain size signal at several locations on the beachface were related to the morphological response: sediment coarsening being associated with accretion at the berm and step crest, and fining associated with accretion seaward of the step. They note, however, that distinct phases of the observed morphological change were not generally reflected in the grain size signal.

Lagrangian tracers have a long history of use for characterising sediment dynamics on beaches. In the gravel beach literature, particle tagging with fluorescent paint (*Nordstrom and Jackson*, 1993; *Ciavola and Castiglione*, 2009; *Stark and Hay*, 2016), or radio frequency identification tags (RFID; *Osborne*, 2005; *Allan et al.*, 2006; *Curtiss et al.*, 2009; *Dickson et al.*, 2011; *Miller et al.*, 2011; *Miller and Warrick*, 2012; *Bertoni et al.*, 2012; *Grottoli et al.*, 2015, 2019) has lead to improved characterisations of transport dynamics on tide-to-tide timescales. No studies, to the author's knowledge, have made use of cobble-sized tracers to investigate transport at the shorter timescale of swash flows on a coarse-grained or MSG beach.

Here, results are presented from a field study at Advocate Beach, Nova Scotia. The study made use of collocated observations of bed level elevation using ultrasonic range sensors, and mean surficial grain size using digital imagery in the swash zone, at subsecond to several seconds resolution. The digital imagery and observations of bed level were both

obtained using low-cost, commercially available sensing equipment. The observations are presented in the context of berm formation and evolution over two high-tide cycles. The objectives of this chapter are: (1) to investigate the coevolution of bed level and mean surficial grain size, seeking insight into the phenomenological role of grain size on swash zone morphological evolution, (2) to investigate the dynamics of individual particles in swash flows using video-based Lagrangian particle tracking, and (3) to assess the utility of low cost range sensing and video-based methods for quantifying bed level and mean grain size change in the sub-aerial swash zone.

7.2 Methods

7.2.1 Experiment Overview

A field experiment was conducted between 14 and 27 October, 2018 at Advocate Beach, Nova Scotia. The experiment spanned 27 tides, which are hereafter referred to by their low tide index within the experiment, i.e., 1 though 27. The focal point of the experiment was to investigate the coevolution of bed level and mean surficial grain size, with an emphasis on processes in the swash zone. Data were collected using a four-element array of collocated ultrasonic range sensors and cameras, along with an overhead camera used for tracking the movements of tracer cobbles in the swash. Both systems were movable, and mounted over the swash zone during periods of low to moderate energy forcing conditions, in anticipation of cusp formation (Chapter 5). Beach-scale surveying of bed level and grain size was carried out on a tide-to-tide basis. Results from the survey component are presented in Chapter 6.

Coincident evolution of beach morphology and sediment properties in the swash zone was investigated using an array of collocated Maxbotix MB7384 ultrasonic range sensors (range resolution of *ca*. 1 mm) and 5 megapixel Raspberry Pi cameras (Fig. 7.1). The array consisted of four downward-facing range sensor/camera pairs, cantilevered approximately 2 m horizontally over the swash on an instrument frame that could be moved as shoreline position changed with the tide. The pairs were separated by 0.9 m alongshore (i.e., having a total longshore span of 2.7 m), and had a nominal elevation of 0.75 m above the bed. The range data were sampled at 6 Hz, and the images at 0.2 Hz. Each of the four array element pairs were controlled by a Raspberry Pi single board computer, which also served as the data logger. A wireless router, connected to the Raspberry Pis via ethernet, enabled Wi-Fi

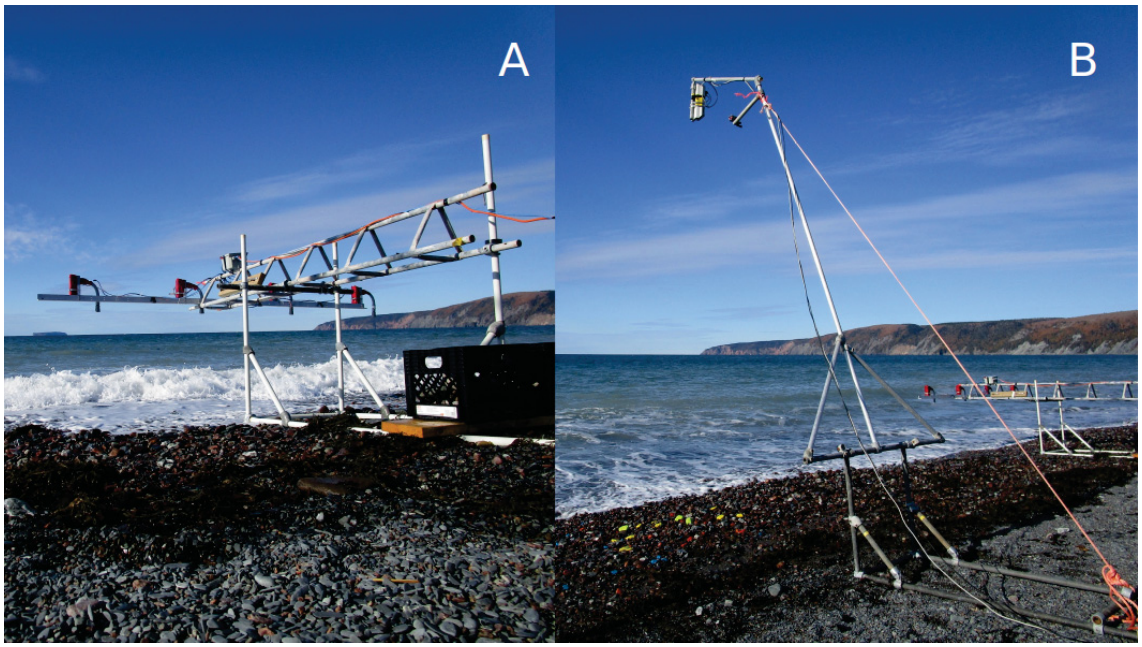

Figure 7.1: Instrument frames used during the 2018 experiment at Advocate Beach. (A) The array frame, with its four ultrasonic range sensor and camera pairs used to observe bed level change and grain size, respectively, in the swash zone. Each pair was separated by 0.9 m in the alongshore from its nearest neighbour, at a nominal elevation of 0.75 m above the bed. (B) The overhead camera frame, from which a downward-looking camera was suspended in order to monitor the transport of painted tracer cobbles in the swash. The camera was elevated approximately 3 m above the bed.

communication with the Pis to initiate and terminate data logging. The four computers were time-synchronised using network time protocol (NTP), and powered from a 12 V marine battery. The instrument frame was assembled near the high water line and data were collected at 3 to 5 "stations" during late flood tide, high tide, and early ebb. At each flood tide station, sampling was initiated prior to the maximum swash runup position passing beneath the array, and continued until the bed was fully obscured by water (i.e., the swash zone was no longer in the instruments' field of view). At ebb stations, the frame was positioned so that the transition from full water cover to fully-exposed bed could be captured. The longest sampling periods corresponded to high tide, when the array stations could be held through the shoreline's advance and retreat, from late flood into early ebb. The position of each array element was recorded using RTK (real time kinematic) GPS at each station.

An overhead Raspberry Pi camera – also network-connected and serviceable via the wireless router – was used for monitoring tracer cobble transport in the swash zone. The

camera was mounted to a second instrument frame, consisting of a semi-stationary base which could be moved with the changing shoreline position, and a moveable arm which supported the camera, allowing it to view the swash zone from a height of *ca*. 3 m without the frame base being in the image. The image field of view at the beach surface was approximately 2.4 by 4.3 m (longshore by cross-shore). During low to moderate wave energy conditions, the overhead camera frame occupied 3 to 5 stations near the high water line (HWL). A minimum of three ground control points were captured at each station using RTK GPS to provide a scaling between pixel and ground coordinates. Prior to deployment, cobbles were sieved into three different size classes: 22.4 to 31.5 mm, 31.5 to 45 mm, and 45 to 63 mm. The cobbles in these size classes were painted blue, orange, and yellow, respectively. The camera frame stations were typically chosen to capture cobble transport during high tide and early ebb, so the cobbles could be retrieved and redeployed after the shoreline had retreated. The frame held a station until the camera's field of view no longer contained the mean shoreline position. Video was recorded continuously throughout.

The alongshore orientation of the four range sensor-camera elements on the array frame was chosen to capture the development of beach cusps, or other three-dimensional morphology in the alongshore. The geometries of both instrument frames (i.e., their fields of view in relation to their bases, which were in contact with the beach surface) were chosen so that the mid-swash zone could be sampled without the bases of the instrument frames interfering either with the data collection, or with the swash processes being observed. This limited the use of the frames to 'fairweather' conditions, during which the maximum swash runup distance was less than approximately 4 m, favourable for cusp formation (Chapter 5). The majority of tides were characterised by high steepness incident waves leading to an energetic shorebreak. There were three periods of fairweather forcing characterised by low amplitude, low steepness waves during which the swash array frame could be deployed: tides 15-16, tides 19-22, and tide 27.

Local grid coordinates were defined in keeping with previous experiments at the site (Chapters 4 and 5), with the origin defined as the former position of a vertical pressure sensor array (see Chapter 4), approximately 20 m seaward of the nominal high tide shoreline. x is alongshore, positive to the northwest, and y is positive offshore.

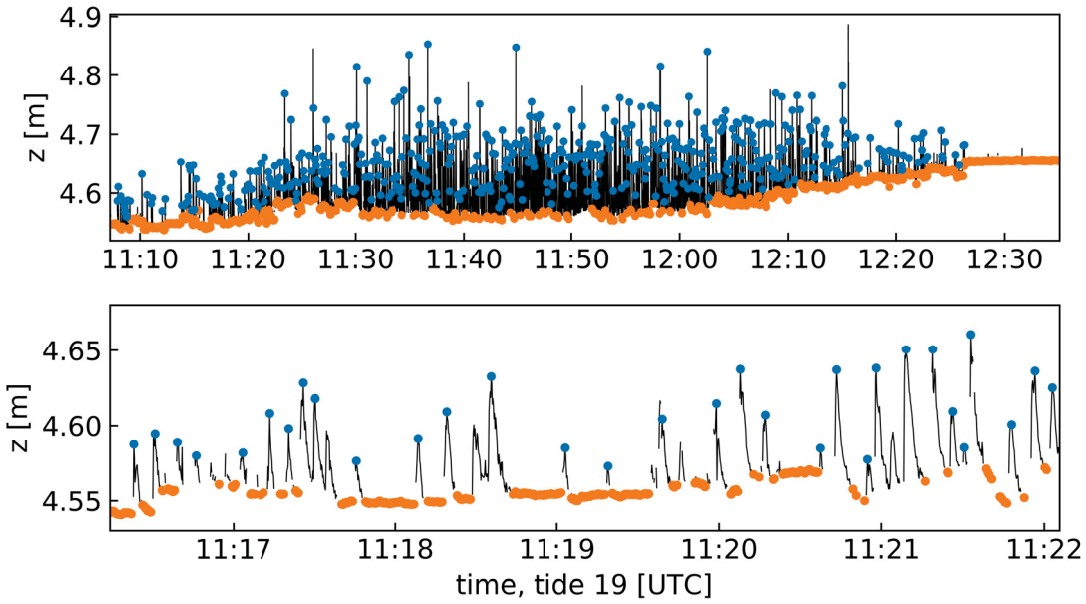

Figure 7.2: Time series of elevation data, collected during high tide by the southmost array element. Orange dots represent the extracted bed level, and blue dots represent swash height maxima. Tide 19.

7.2.2 Bed Level and Swash Analysis

The data from the ultrasonic range sensors represent first returns (i.e., the distance to the nearest object within the $O(10$ cm) radius beam pattern), which were either from the exposed beach surface in the absence of swash, or from the elevation of the water surface when swash was present. Processing of the range time series was carried out to isolate the bed level and swash signals. Spurious returns of 0.5 and 5 m – the sensors' minimum and maximum sensing distances – made an additional processing step necessary. The spurious returns were attributed to diminished or scattered acoustic reflections from aerated swash at leading edge of the swash front. No return, or returns not within the 0.5-5 m sensing range of the instruments, result in range output of 0.5 or 5 m.

The bed level was extracted from the range data time series by identifying sequences of N samples in which no sample differed from the first sample in the sequence by more than some predefined range threshold. The time threshold was set to 9 samples (1.5 seconds), and the range threshold set to 5 mm. For analysis applications requiring a uniformly sampled bed level time series, gaps in the series associated with swash were filled via linear interpolation.

The swash thickness was extracted from the range time series by isolating all values at ranges less than the range to the interpolated bed level, minus a buffering threshold of 2 mm to eliminate spurious low amplitude peaks due to instrument noise. The isolated segments were defined to be swash events if they had a minimum duration of 5 samples (0.83 s) and a local maximum at least 15 mm above the bed that did not exist at either endpoint of the segment. These criteria were implemented to exclude spurious events in the swash time series that did not exhibit the anticipated shape of a runup event (i.e., a sequence of increase, maximum, and decrease in swash height). A sample elevation time series, with the extracted bed level and swash height maxima, is shown in Fig. 7.2.

Bed level change between swash runup events was computed by differencing the final values in each bed level segment in the (non-interpolated) bed level signal, where a segment consisted of contiguous points meeting the exposed bed criteria described above. This definition of bed level change was chosen to be conceptually consistent with the definition proposed by *Blenkinsopp et al.* (2011).

7.2.3 Digital Grain Sizing

A wavelet-based digital grain sizing (DGS) package (see *Buscombe*, 2013), implemented in Python, was used to estimate grain size statistics from the camera array imagery. The DGS algorithm does not require calibration, and takes as input a grain-resolving image containing only sediment.

The image sets from the four array-frame cameras were manually curated to include only those images with fully exposed bed in the region of the image used for analysis. Each image was cropped to half width and height in the centre of the frame, corresponding to a field of view at the bed of 1.42×0.85 m, for a 0.75 m camera height above the bed. Input parameters for the algorithm include a pixel to physical unit scaling, a maximum feature diameter to be resolved, and a dimensional scaling factor. The bed-level signal extracted from the range sensor time series was used, along with the camera's known field of view specifications, to establish the pixel to physical unit scale factor for each image. The bed level signal was smoothed to eliminate short period changes in bed level attributable to individual grain movements. The maximum feature diameter, defined as the inverse ratio of the pixel width of the frame to the width of the largest feature to be resolved, was also dynamically assigned to maintain a maximum feature resolution of 56 mm – a value chosen to balance output resolution at both small and large grain sizes. The

dimensional scale factor was set as 0.8. See Appendix B for a discussion of the choice of dimensional scale factor, as well as for more detailed descriptions of the remaining input parameters.

Though the algorithm is capable of returning a full grain size distribution, validation of the output against distributions from both sieve and manual point count analyses (see *Barnard et al.*, 2007; *Buscombe et al.*, 2010, or Appendix B for a description of the point count method) indicated that only the lowest moment of the grain size distribution (mean grain size) was captured satisfactorily. We attribute the algorithm's poor representation of the higher order moments to the wide grain size distribution. See Appendix B for further discussion of the validation procedures.

7.2.4 Cobble Tracking

Cobble trajectories were manually extracted from the video image sets captured by the overhead camera. To mitigate the difficulties posed by the partial or full occlusion of cobbles by bubbles and foam in the swash, pixels with high white content (red, green, and blue channel intensity values all exceeding 175 out of 255) were subtracted from each image, then each image was averaged with the 10 preceding images. The resulting composite images showed a partially reconstructed bed, with more tracer cobbles being visible than in the original images. Due to the regular occlusion of the cobbles by swash, the extracted trajectories are assumed to be accurate to within the timescale of the swash forcing (*ca.* 6 s), i.e., any transport occurring while the cobbles were submerged was not captured. The 45-63 mm (yellow) size class was most easily identified in the images. Reduced visibility of the other size classes meant that cobble identities could not be maintained with confidence between instances of occlusion. Thus, only trajectory data from the 45-63 mm size class is presented in this chapter. Tracking of the cobbles began immediately after they were deposited in the swash. Tracking was stopped when cobbles were buried or transported out of the field of view.

7.3 Results

7.3.1 Swash Zone Morpho-Sedimentary Dynamics

The frame bearing the range sensor and camera arrays was deployed during five high tides over the course of the experiment, each characterised by low to moderate energy forcing

conditions. During tides 19 and 27, the array was favourably positioned relative to the HWL such that intermittent swash height and bed exposure could be observed for periods longer than one hour without moving the frame. For these cases, time series of the swash thickness, bed level, and image-derived mean grain size are available. During both tides 19 and 27, a pronounced berm developed near the HWL.

Applying the digital grain sizing algorithm to the images captured by the Raspberry Pi cameras enabled the examination of the coevolution of bed level and mean grain size at the bed beneath each array element. Figs. 7.3 and 7.4 show time series of the bed level and mean grain size for the periods of high tide data collection during tides 19 and 27. The grain size data are inherently noisy, so the individual data points are less valuable than the trends revealed by large numbers of data points. In both cases, the morphological context was the formation – and in the latter case the formation and shoreward translation – of a high tide berm. Visual inspection of the time series indicates that the bed level and mean grain size measures tend to co-vary.

During tide 19, coarse material accumulated near the HWL, initially in a mound directly beneath the north-most array element ($x = -15.5$ m in Fig. 7.3). The mound initially resembled a large cusp horn, though its alongshore extent widened over the following tens of minutes, becoming steeper in the offshore direction and more berm-like. An incipient topographic low existed beneath the southmost array element ($x = -18.2$ m). By early ebb tide, a more uniform berm had formed, with irregular undulations in amplitude alongshore. The berm beneath the array sloped downward to the south (note the elevation differences between the array element at $x = -15.5$ and $x = -18.2$ m), with a maximum amplitude of nearly 20 cm, immediately beneath the northmost array element. The grain size time series are noisy, and sparsely sampled, especially at high tide (i.e., between 11:30 and 12:00) due to the more frequent swash events. However, common trends can be noted: namely, the upward trend in mean grain size as the swash zone first reached the sampling region (11:10-11:20), which precedes the onset of the upward trend in the bed level time series. The apparent fining of the surficial sediments at $x = -18.2$ m following the initial coarsening trend is also evident, and corresponds to a similar, but lagged, trend in the bed level time series.

During tide 27, a berm began to form seaward of the HWL (note the increase in z in Fig. 7.4, 13:50-14:10). As the swash zone migrated landward, coarse material was pushed

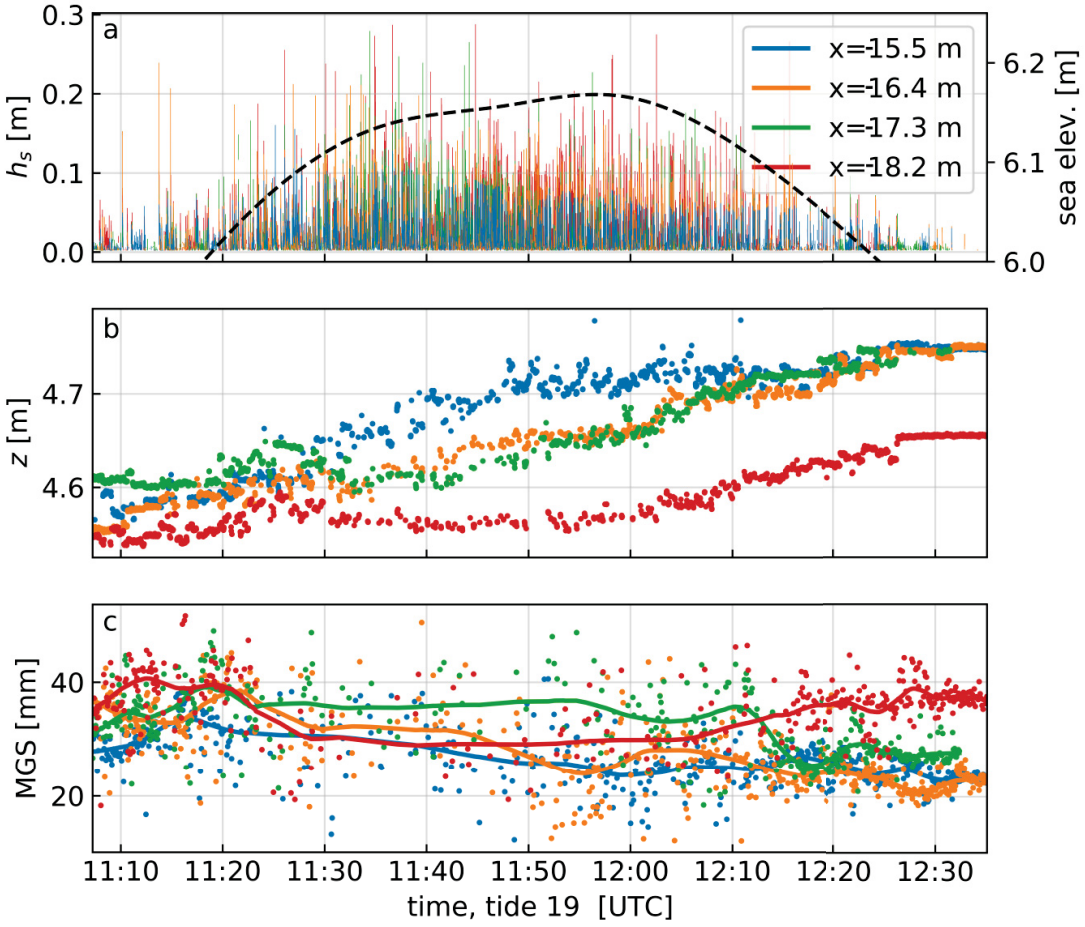

Figure 7.3: Morpho-sedimentary time series during high tide for tide 19, recorded by the four range sensor-camera array elements. (a) Swash height. (b) Bed level. (c) Mean grain size. The solid line is a locally weighted (loess) regression using a *ca.* 10 min averaging window.

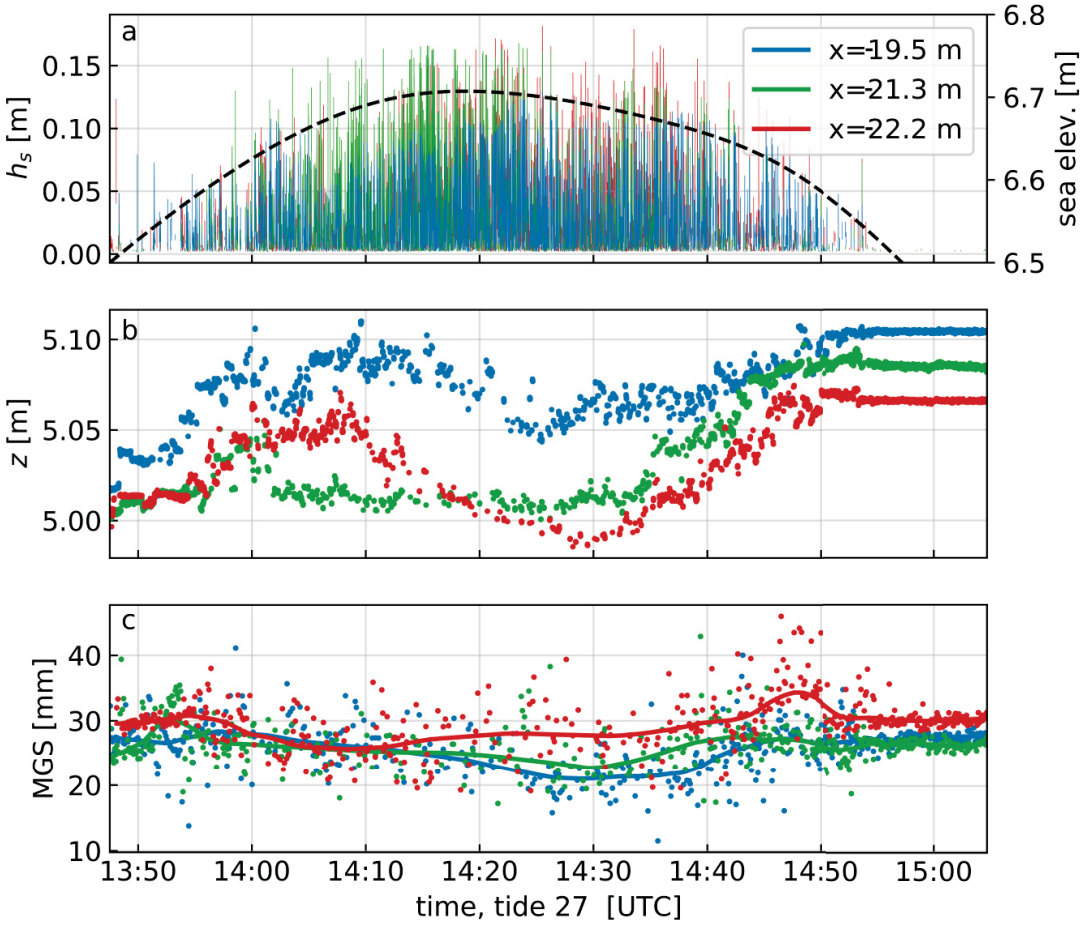

Figure 7.4: Morpho-sedimentary time series during high tide for tide 27, recorded by the four range sensor-camera array elements. (a) Swash height. (b) Bed level. (c) Mean grain size. The solid line is a locally weighted (loess) regression using a *ca.* 10 min averaging window.

over the berm crest, leading to a shoreward migration of the berm by roughly 2 m. The decrease in bed elevation between 14:10 and 14:30 is a result of this berm translation. During early ebb tide, coarse material began to accrete on the seaward face of the berm, leading to the bed elevation increase observed between 14:30 and 14:50. The mean grain size was initially coarse (*ca.* 30 mm) in all three of the sampled locations, but shows a downward trend in two of the three cases. Fining occurred in all cases after the initiation of berm growth seen in the bed level time series. In all cases, the minimum mean grain size occurred at or just after high tide, when the sampling location was near the mid-swash zone, and also nearest the base of steep berm face. Bed surface coarsening coincided with the increase in bed level on the seaward face of the berm during early ebb tide.

A phenomenon that was often observed, both visually and in the grain size time series, was the shoreward migration of a band of coarse material at the top of the swash zone during late flood tide (see Figs. 7.3, 7.4: 'bumps' in the mean grain size time series). Similarly, a coarsening of the substrate was generally observed at the seaward edge of the swash zone during early ebb tides. Surficial fining was generally observed nearer the mid-swash zone. This fining is apparent in both Figs. 7.3 and 7.4.

The distribution of bed level changes (Figs. 7.5 and 7.6) shows that the majority of changes between swash events were near zero, with larger changes – both positive and negative – that are loosely approximated by a Gaussian distribution, though with higher kurtosis values (kurtosis of 5.1 and 5.4 for tides 19 and 27, respectively, relative to a value of 3 for a Gaussian distribution). This finding is consistent with similar analyses in the literature (e.g., *Horn and Walton*, 2004; *Turner et al.*, 2008; *Masselink et al.*, 2009; *Blenkinsopp et al.*, 2011), which have demonstrated that bed level change over the course of a tidal cycle is the result of the cumulative effect of many instances of small accretion and erosion. The joint probability distributions of the swash height and changes in bed level between swash events do not indicate a clear relationship between the two.

Fig. 7.7 shows time series of swash height, bed elevation, and the change in bed elevation during the high tide data collection of tide 27. In general, the envelope of bed elevation change is largest when bed elevation was higher (i.e., near the beginning and end of the time series). This may be due to the larger mean grain sizes associated with coarse lag at the leading edge of the swash during flood tide, and the accretion of coarse material on the seaward face of the berm during flood.

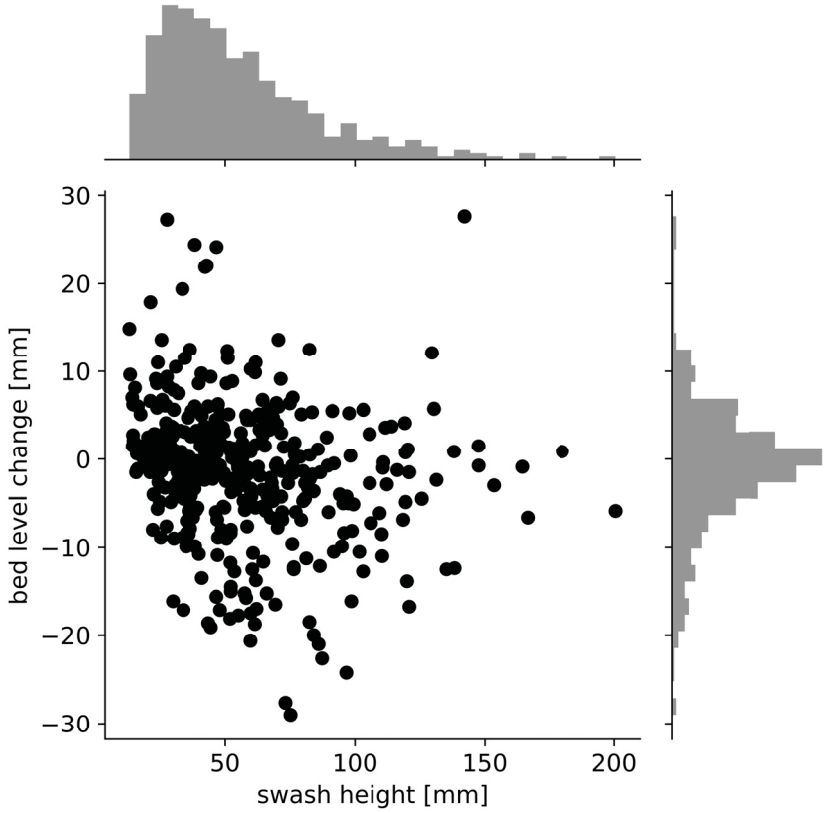

Figure 7.5: Joint distribution of bed level change between swash events and swash height from the high tide data collection run of tide 19 (see Fig. 7.3). Data from all four sensors are included.

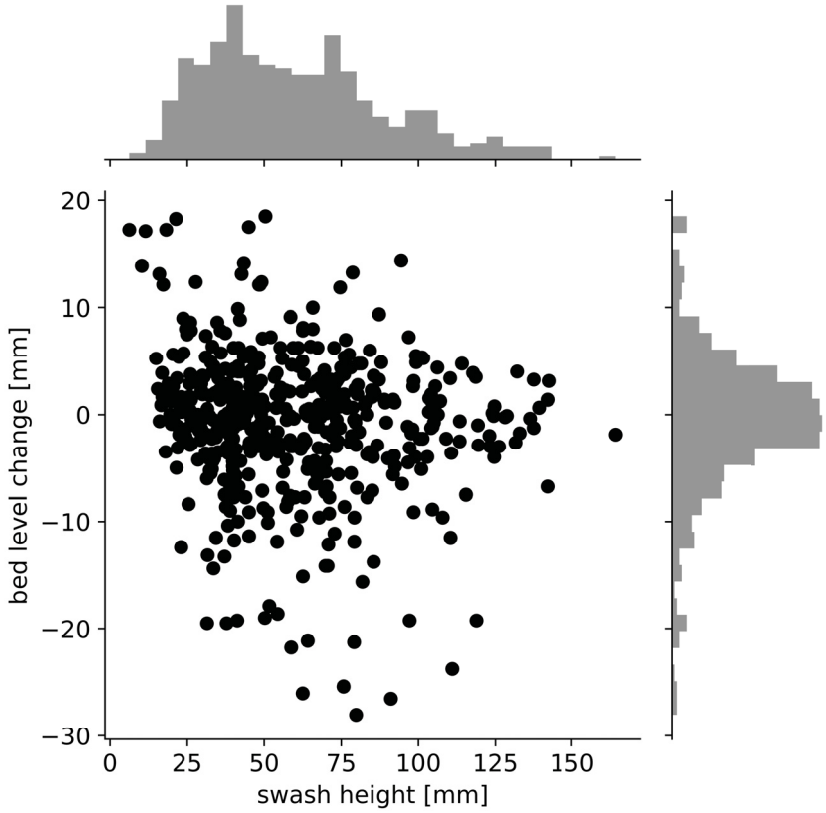

Figure 7.6: Joint distributions of bed level change between swash events and swash height from the high tide data collection run of tide 27 (see Fig. 7.4). Data from three sensors are included.

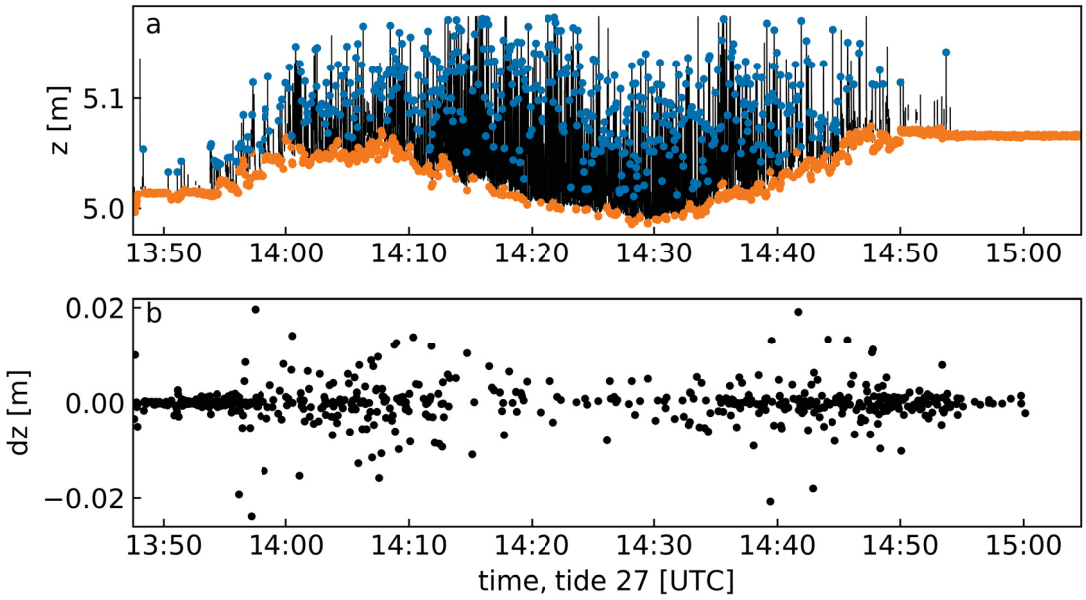

Figure 7.7: (a) Time series of swash height and bed level during tide 27 at the $x = -22.2$ m alongshore array element, and (b) the corresponding change in bed level, dz.

7.3.2 Cobble Dynamics

Cobble trajectory statistics were computed from data associated with tide 19. Video datasets of cobble transport in the swash zone were collected at four locations in the cross-shore (i.e., four distinct mean shoreline positions) during high tide and early ebb:

- Station 1: at high tide, when the shoreline position was nearest to the HWL. Here, the tracer cobbles were deployed atop the coarse berm material. The camera's cross-shore field of view spanned $y \approx$ -14.5 to -11 m in local grid coordinates, and contained almost entirely coarse berm material.

- Station 2: 45 min after high tide. The shoreline and swash zone coincided with the region immediately seaward of the coarse berm. Coarse berm material was present in the landward one third of the camera's field of view, which spanned from $y \approx$ -9.5 to -6 m (i.e., 5 m seaward of station 1). The cobbles were deployed in the mid-swash, over a combination of the coarse seaward face of the berm and the finer material farther seaward.

- Station 3: 75 min after high tide. The swash zone no longer coincided with any coarse-grained berm material, and the substrate was predominantly fine-grained and

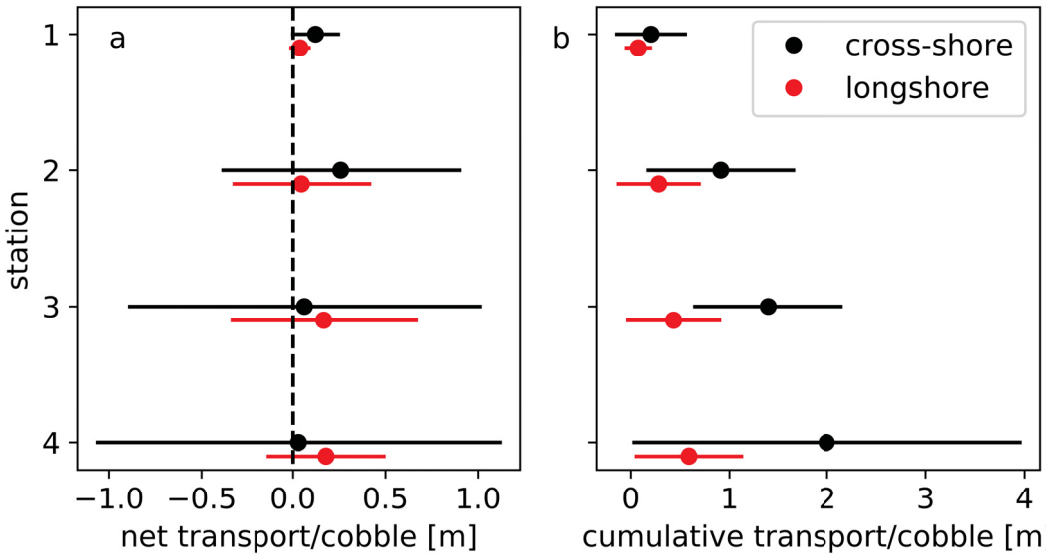

Figure 7.8: Mean and standard deviation of the (a) net and (b) cumulative cobble transport. Positive is shoreward.

uniform. The cobbles were deployed near mid-swash and mid-camera frame. The camera field of view spanned $y \approx$ -5.5 to -2 m across-shore (9 m seaward of station 1).

- Station 4: 85 min after high tide, with the bed conditions and the cobble deployment being similar to those described for location 3. The cross-shore field of view of the camera in this location was $y \approx$ -2.5 to 1 m (12 m seaward of station 1).

The net and cumulative transport statistics for all four stations are summarised in Fig. 7.8. The net cobble transport was shoreward at stations 1 and 2, where the substrate consisted wholly or in part of coarse-grained berm material. At stations 3 and 4, where the bed surface was predominantly fine-grained, the net transport was near zero, but with a high degree of variation between individual cobbles. The cumulative transport of cobbles increased to seaward (i.e., cobbles were more mobile where the mean shoreline position was farther to seaward), corresponding to a decrease in coarse-grained material in the swash zone substrate. The longshore component of transport was small in comparison to the cross-shore transport at all the stations, consistent with previous observations at Advocate Beach (e.g., *Stark and Hay*, 2016).

Closer inspection of the transport characteristics within each station reinforces the

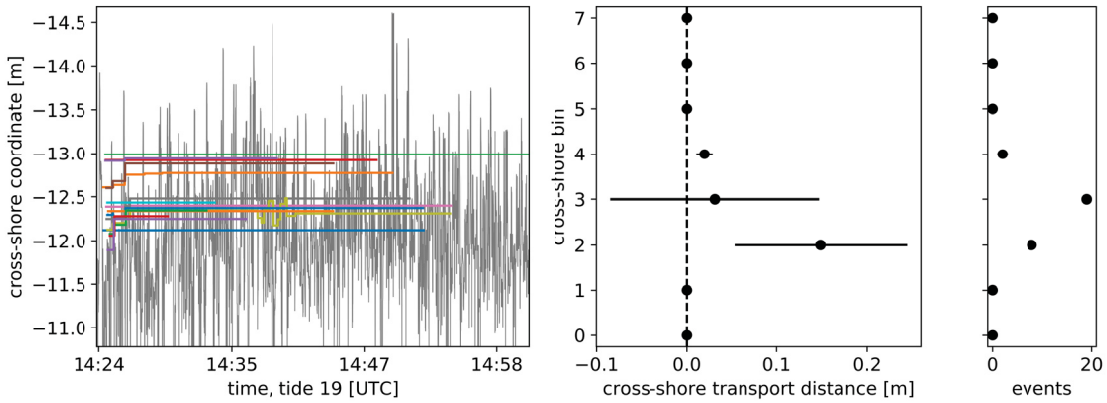

Figure 7.9: Cross-shore cobble transport trajectories and transport distances at station 1 during tide 19. The bed composition was coarse-grained, leading to net onshore transport and low transport rates. (a) Time series of the cross-shore component of all the cobble trajectories. The grey line indicates the time-varying position of the swash front. Landward is up. (b) Mean and standard deviation of the cross-shore transport distance in each each of eight bins corresponding to the the cross-shore coordinates in (a). The transport distance was assigned a bin based on its starting point. (c) Number of transport events used in the calculations of the means and standard deviations in (b).

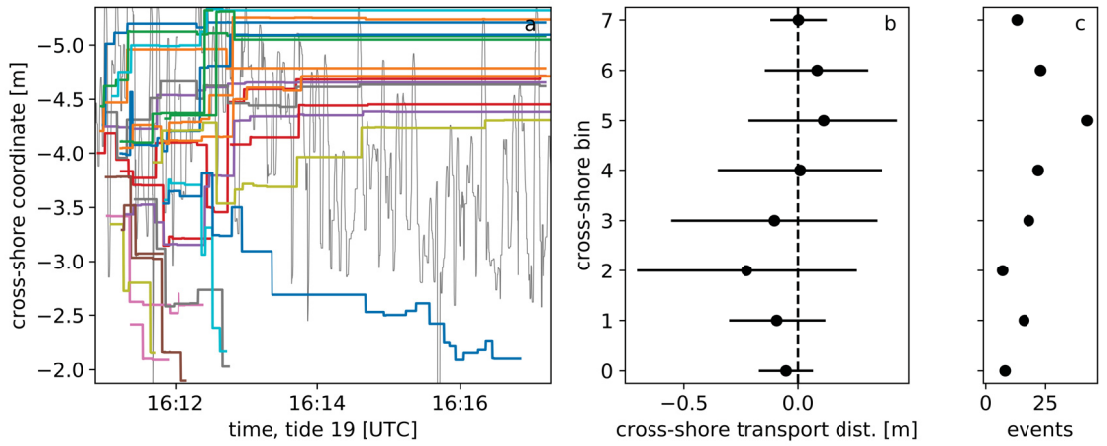

Figure 7.10: Cross-shore cobble transport trajectories and transport distances at station 3 during tide 19. The bed composition was predominantly fine-grained, leading to higher transport rates than at other stations. (a) Time series of the cross-shore component of all the cobble trajectories. The grey line indicates the time-varying position of the swash front. Landward is up. (b) Mean and standard deviation of the cross-shore transport distance in each each of eight bins corresponding to the the cross-shore coordinates in (a). The transport distance was assigned a bin based on its starting point. (c) Number of transport events used in the calculations of the means and standard deviations in (b).

finding of low cumulative transport and net onshore transport of cobbles in the presence of the coarse-grained berm material. For example, data from station 1 are shown in Fig. 7.9. At the more seaward stations, a general trend of divergence of the cobbles away from the mid-swash zone is observed: shoreward transport above the mid-swash level, and seaward transport below. This was true in particular for stations 2 and 3, for which the swash zone was well-centred in the camera's field of view, and the surficial sediments were predominantly fine-grained. Data from station 3 illustrating this divergence are shown in Fig. 7.10.

7.4 Discussion

The morpho-sedimentary evolution of a mixed sand-gravel beach was investigated at the swash scale ($O(10^{-2} - 10^{0})$ m) through point observations of bed level and grain size with temporal resolution on the order of seconds. Data were collected during selected tides characterised by low steepness wave incidence and berm building.

The bed level and mean grain size signals displayed qualitative similarities. Point observations during berm formation and evolution were captured by the ultrasonic range sensor and camera pairs. In general, accretion at the berm corresponded to surficial sediment coarsening, though finer structure in the grain size signal was also apparent, particularly as the leading edge of the swash zone passed beneath the instrument array on flood tide (Figs. 7.3 and 7.4), and during the observed instance of shoreward berm translation during tide 27 (Fig. 7.4).

The shoreward migration of a coarse band of sediments with the leading edge of the swash appeared to precede any substantial changes in bed elevation during tides 19 and 27. This precursor to berm formation has been reported in the literature (e.g., *Austin and Buscombe*, 2008; *Duncan Jr*, 1964), and has been attributed to the temporary stranding of coarse material at the landward edge of the swash. At high tide, the slowdown and arrest of the swash zone's shoreward translation leads to continued accretion at the leading edge. The berm crest migrates shoreward during periods of berm overtopping, wherein the coarsest mobile fraction is saltated, or 'thrown', over the crest. This is followed by accretion on the seaward face of the berm during the seaward regression of the shoreline during early ebb tide, leading to an increase in berm width (e.g., *Pontee et al.*, 2004; *Austin and Masselink*, 2006). The array data are consistent with this conceptual model. They

indicate that the coarsest sediments correspond to the berm crest, nascent or developed, with fining occurring on the seaward face of the berm. Note also that the peak in mean grain size associated with the berm in the Fig. 6.4b profiles generally appears one station shoreward of the Δz peak in Chapter 6, Fig. 6.4a, and appears to be more closely aligned with the HWL.

The above results and interpretation of the swash zone bed level and mean grain size signals are supported by the cobble tracer results. The divergence of the cobbles from the mid-swash toward the seaward and shoreward edges of the swash zone is consistent with the formation of a coarse deposit that migrates with the leading edge of the swash zone, as well as with the observed fining of the surficial material in the mid-swash zone in many cases. Though not verifiable with the observations here, it is likely that seaward transported material accumulated in the beach step region associated with bore collapse at the shore break, which also likely migrated with the cross-shore translating swash zone. The beach step has been demonstrated elsewhere to play an important role in controlling wave breaking on steep beaches, and has also been shown to migrate with the translating swash zone (*Austin and Buscombe*, 2008). The net shoreward transport of cobbles in the vicinity of the berm (Fig. 7.8, stations 1 and 2) suggests that the beach profile at high tide was in disequilibrium with the forcing in this case.

The cobble transport results highlight the influence of the substrate on the transport dynamics of coarse particles; transport is favoured on a fine substrate, where low angles of pivot and higher exposure to lift and drag forces cause the coarse particles to overpass the finer ones. Transport is inhibited where the substrate is coarse, due to higher angles of pivot required for mobilisation and decreased return flow velocities resulting from increased infiltration and hydraulic roughness.

The low-cost ultrasonic range sensors, though yielding a lower resolution data product than similar sensors used in other studies, were capable of characterising bed level changes with probability distributions that are comparable to those reported elsewhere (e.g., *Turner et al.*, 2008; *Blenkinsopp et al.*, 2011), including at least one gravel beach (*Russell et al.*, 2009): namely, having a quasi-Gaussian distribution that is indicative of an inter-swash timescale for profile evolution, where net changes to the profile are a result of time integration of small changes in bed elevation (both positive and negative) over many swash cycles. The ultrasonic range sensors used in this study would be less suitable where

resolution finer than $\pm$ 1 mm is required (e.g., in a pure sand setting where average grain sizes are less than 1 mm).

The high kurtosis of the bed level change probability distributions (kurtosis of 5.1, 5.4 for tides 19 and 27, respectively) relative to a Gaussian distribution (kurtosis value of 3) may be attributable to the 'armouring' effect of the coarse bed: low energy swash events, i.e., small runup events having low velocities, may not have lead to mobilisation or deposition in the range sensor sampling region, resulting in a bed level change probability distribution more heavily zero-weighted than a Gaussian distribution. This is in contrast to a sandy bed, where some degree of bed level change might be expected with each swash event due to the higher mobility of sand grains. Instances of greater bed level change associated with the transport of gravel- or cobble-sized grains into or out of the sampling region may also have contributed to a higher kurtosis value through increased weighting of the tails of the bed level change distribution.

The Raspberry Pi cameras were adequate for capturing images and video of the bed for digital grain sizing and cobble tracking. The difficulties resolving higher order moments of the grain size distribution (see Appendix B) can more likely be attributed to the wide grain size distribution at Advocate Beach, which spans three orders of magnitude.

7.5 Conclusions

The morpho-sedimentary evolution of a mixed sand-gravel beach was investigated at the swash zone scale, through point observations of bed level and mean grain size with temporal resolution on the order of seconds. Data were collected near high tide during periods of fairweather forcing characterised by low steepness wave incidence and berm building. The shoreline position changed rapidly due to the large (*ca.* 10 m) tidal range.

Point observations of swash zone bed level and mean grain size at the timescale of the swash forcing displayed qualitatively similar trends. In general, increases in bed level (e.g., during berm building) corresponded to increases in mean grain size. Finer structure in the grain size signals was also observed. The largest mean grain sizes were generally associated with the leading edge of the mean swash front, and the smallest sizes with the mid-swash zone. This was interpreted as cross-shore divergence of gravel and cobble-sized material out of the mid-swash zone.

The tracer cobble trajectory results support the above interpretation. Cobbles initially

positioned above the mid-swash zone were generally transported shoreward, and those positioned below the mid-swash were transported seaward. The shoreward transport in the upper part of the swash zone is consistent with the formation of a coarse-grained deposit, or incipient berm, at the leading edge of the swash. The downslope-transported cobbles were likely deposited near the seaward edge of the swash zone, contributing to the formation of a transient coarse-grained beach step. The step would then serve as a source of coarse material, which would be reintroduced to the swash zone during the ebb-tide seaward translation of the shoreline, contributing to the coarsening of the beach surficial sediments during fairweather forcing (Chapter 6). The substrate composition affected the magnitude of transport: tracer cobbles were less mobile, but experienced net shoreward transport in the vicinity of the coarse berm material.

The low-cost, commercially available range sensors used in this study were successful in resolving signals of morpho-sedimentary change in the subaerial swash zone. This finding suggests great potential for the use of close-range remote sensing techniques to examine the coevolution of bed level and grain size in response to swash processes, at least in macrotidal mixed sand-gravel settings. More precise instrumentation would reduce the need for added processing, and would be required where a greater proportion of the grain size distribution is less than *ca*. 1 mm.

In considering future work, it would be of interest to make similar measurements with greater spatial coverage, particularly in the cross-shore, in order to better resolve the fine-scale grain size and bed level changes associated with incipient berm formation at the leading edge of the swash. More sensors in an across-shore configuration would also allow for the consideration of volume change in the swash region; e.g., is positive bed level change at the berm balanced by erosion from the mid-swash, or must material be sourced from the step region as well? The step has been shown to have an important influence on swash processes via its control on wave breaking, and has been suggested to be an important source of coarse material for swash zone morpho-sedimentary evolution in MSG settings. However, the methods employed for this study are not capable of directly observing processes at the step. To the knowledge of the author, no non-intrusive methods have been used to study the step in a field setting.

Given the acknowledged influence of the full grain size distribution on mixed sediment transport dynamics (e.g., the increased mobility of gravel-sized particles in the presence

of a large sand fraction; *Wilcock et al.*, 2001), quantifying higher order moments of the grain size distribution is also of interest. It is possible that improvements upon the digital grain sizing results presented in this chapter could be obtained using a calibration-based approach (e.g., *Warrick et al.*, 2009). Other properties of the grains, namely particle shape, have also been demonstrated to play an important role in particle transport dynamics. The ability to digitally quantify particle shape at wave forcing timescales would be valuable, particularly in the context of coarse particle transport in swash flows.

CHAPTER 8

CONCLUSIONS

This thesis presents observations of hydrodynamics, morphodynamics, grain size, and sediment dynamics at Advocate Beach, Nova Scotia – a steep (1 in 10 slope), megatidal, mixed sand-gravel (MSG) beach. The beach is positioned near the head of the Bay of Fundy, and is generally fetch-limited, being forced by steep, locally generated waves with mean periods of 4-7 s, leading to an energetic shore break. The mean tide range is 10 m. The large tide range, steep slope, and broad, generally well-mixed grain size distribution make Advocate Beach advantageous as a study site for reasons both practical and scientific. The intertidal beach can be accessed during each low tide to deploy, retrieve, or maintain *in situ* instrumentation. The selective transport properties of heterogeneous sediments lead to spatially and temporally varying sedimentation patterns often manifesting as complex three-dimensional morphologies (e.g., beach cusps) accompanied by grain size sorting. The large tide range leads to a reduction in the force applied per unit of beach surface area and to a heightened potential for observable morpho-sedimentary signals. However, because of the typically energetic shorebreak at Advocate Beach and at coarse-grained beaches in general, where impulsive wave forcing and large mobile grains impose a hazard to instrumentation, conventional *in situ* sampling methods employed at sandy beaches are not suitable.

The observations were obtained during two field campaigns. The first campaign (Chapter 3.2) made use of beach-scale video monitoring and arrays of buried pressure sensors to observe beach cusp dynamics and the vertical pore pressure response of the bed under oscillatory and hydrostatic loading due to waves and tides. The second campaign (Chapter 3.3) employed GPS and image-based surveying to observe bed level and mean surficial

grain size change on the scale of the intertidal zone, ultrasonic range sensors and digital imagery to obtain changes in bed level and mean grain size in the swash zone, and video-based Lagrangian tracking of natural cobble tracers in swash flows. The purpose of these studies was to gain insight into morpho-sedimentary, hydrodynamic, and hydraulic processes on mixed sand-gravel beaches on sub-tidal timescales. The datasets were used to address the following objectives: (1) characterise the depth dependence of oscillatory pore water pressures in intertidal sediments induced by surface gravity waves; (2) investigate the morpho- and hydrodynamical processes associated with mixed sand-gravel beach cusp evolution; and (3) investigate the coevolution of bed level and grain size in the swash and intertidal zones.

8.1 Key Findings

1. **Pore-trapped air plays a key role in the dynamics of pressure transmission through the sediment column at Advocate Beach.**

   During the Advocate 2015 field campaign, large and persistent phase lags and high degrees of attenuation of wave-induced pore pressure signals with depth in the upper 50 cm of the beach surface sediments were observed (Chapter 4). The analytical poro-elastic bed response model from *Yamamoto et al.* (1978) provided a good fit to the data. The saturation parameter, defined as the fractional volume of air in the interstitial fluid, was shown to be of first-order importance in determining the pressure response properties of the porous medium. Interstitial air contents of $O(10\%)$ by pore volume were required to recreate the observed pore pressure attenuation and phase profiles. Variations in the hydraulic conductivity, resulting from disturbance of the sediment following instrument burial and subsequent reworking by storms, were also shown to influence the modelled pore pressure response. The persistence of the phase and attenuation properties suggests that pore-trapped air remains in the bed throughout both individual and spring-neap tidal cycles.

2. **Hydrostatic pressure alone does not serve to restore disturbed intertidal beach sediments to equilibrium, at least not on time scales of O(1 week).**

   The burial of the vertical pressure sensor array (Chapter 4) coincided with a 4-day period of low energy wave forcing. The disturbance of the beach sediments

associated with burying the pressure sensor array resulted in a prolonged factor-of-two difference in the oscillatory pore pressure phase and attenuation response. Though the array was subjected to 3-5 m of hydrostatic pressure at high tides throughout this time, the pore pressure response profiles did not return to their apparent 'natural' state until the arrival of a storm event. The pore pressure response prior to the reworking of sediments by storm waves was characterised by reduced attenuation and phase shifting with depth in the sediment, suggesting that the disturbed sediments were more hydraulically conductive, and thus less effective at entrapping air.

3. **Beach cusp dynamics and their location in the cross-shore are strongly influenced by the tide range via the shoreline position and its rate of change.**

   The formation of beach cusps observed during the Advocate 2015 field campaign was strongly influenced by the tides. Formation was favoured during high tide and early ebb, with no cusps being observed at the mid- or low-tide levels. During two instances of cusp field emergence that were examined in detail in Chapter 5, the transition from relict to newly formed cusp fields occurred over *ca*. 1 hour, with initial emergence and relict cusp decay timescales of 10-20 minutes, both visually and in an e-folding sense. The general absence of cusps at the mid-tide level on the beach face suggests a minimum formation timescale of $O(10)$ minutes, or $O(100)$ swash cycles, assuming nominal swash zone widths of 3-5 m at the times when the rate of shoreline translation was largest – as much as 0.007 m s^{-1} at mid-tide at Advocate Beach. The location and dynamics of cusp horns (i.e., erasure/re-emergence versus branching/merging/shifting) appeared to depend on the high water line and its location relative to any pre-existing cusp morphology.

4. **Timescales associated with the emergence of beach cusps on Advocate Beach are dependent on the beach surface grain size distribution.**

   Beach cusps at Advocate Beach are generally characterised by striking differences in grain size between the cusp horns (gravel-cobbles) and bays (sand). During one cusp event analysed in detail in Chapter 5, the emergence of new cusps at high tide appeared to be inhibited by the lack of coarse material present on the beach surface. Cusp emergence occurred shortly after, during early ebb, where the

beach surface consisted of a higher proportion of gravel and cobbles. Persistent correlations observed between changes in bed level and mean grain size (Chapter 6), which suggest a sedimentary feedback component to morphological change, support this finding.

5. **A strong negative correlation exists between the mean surface grain size in the mid-intertidal zone and the forcing energy.**

   During the Advocate 2018 field campaign, the mean surficial grain size on the intertidal beach exhibited fining in response to energetic waves, and coarsening in response to fairweather forcing (Chapter 6). This is the opposite of the expected grain size response on sand beaches. A similar response was previously observed at Advocate Beach by *Hay et al.* (2014), as well as by other authors in the mixed sand gravel beach literature (*Nordstrom and Jackson*, 1993; *Pontee et al.*, 2004; *Curtiss et al.*, 2009; *Miller et al.*, 2011).

6. **A positive correlation exists between changes bed level and mean grain size in the intertidal zone on tide-to-tide timescales.**

   A persistent positive correlation was observed between changes in bed level and changes in the mean surface grain size from one low tide to the next during the Advocate 2018 field campaign (Chapter 6). The correlation was independent of the wave steepness or significant wave height. Though some correlation was apparent at the position of the characteristically coarse-grained high tide berm, the correlation was largest in the mid-intertidal zone – the region seaward of the berm, typically characterised by a broader surficial grain size distribution.

7. **Signals of bed level and mean grain size change with timescales of seconds to minutes are observable using acoustic bed level sensors and digital grain sizing in the intermittently exposed subaerial swash zone.**

   Coincident observations of bed level and mean grain size at timescales commensurate with the swash forcing (Chapter 7) revealed signals providing insights into the morpho-sedimentary dynamics. A positive qualitative correlation was observed over timescales on the order of hours. Finer-scale structure in the signal was observable over timescales of minutes, including signatures of bands of coarse-grained material

that migrated shoreward with the leading edge of the swash prior to high tide berm formation.

8. **The direction and magnitude of cobble transport in swash flows depended upon the cross-shore position of the cobble within the swash zone, as well as the composition of the underlying bed.**

   Lagrangian tracking of natural cobbles in swash flows was carried out using video imagery (Chapter 7). The net transport of cobbles was shoreward, with the smallest cumulative transport at stations where the substrate was predominantly coarse-grained, i.e., in the presence of the berm. When the substrate was predominantly fine-grained, i.e., at stations seaward of the coarse berm, the cobble tracers diverged from the mid-swash zone, being transported either to the shoreward edge of the swash zone, or seaward toward the step. The cumulative transport was greatest where the substrate was fine-grained, and the net transport was near zero. The longshore component of transport was small in comparison to the cross-shore component.

8.2 Implications and Insights

Relative to pure sand or gravel beach settings, few field observations of mixed sand-gravel (MSG) beach dynamics exist in the literature, especially with regard to dynamics in the swash zone. A sound understanding of MSG beach phenomenology is required to inform meaningful parameterisations, and to improve our ability to predict the physical responses of MSG beaches to forcing. This thesis contributes to an observational basis of MSG beach dynamics from which a broader understanding of processes can be drawn. Some notable contributions include (1) observations of the vertical structure of the MSG bed at Advocate Beach as a poro-elastic medium, including the depth-dependent pressure response, grain size distribution, porosity, and hydraulic conductivity. Reported values of the hydraulic conductivity, in particular, of natural sand-gravel mixtures in the literature are few, despite the acknowledgement by *Mason and Coates* (2001) of hydraulic conductivity as a leading order influence on the characteristics of MSG sediment transport; (2) observations of MSG beach cusps, about which few, if any, dynamical observations exist in the literature, but which display notable differences from cusps on sand beaches, namely, the important role played by the process of size segregation in cusp formation on MSG beaches; and (3)

observations of morpho- and sedimentary dynamics at multiple scales in space and time, which to date are also largely unavailable in the MSG beach literature, particularly with regard to grain size dynamics.

In addition to the contributed observations, many of which may be of interest in their own right, the results of this thesis have provided insights into the hydro/morphodynamics and sediment dynamics in the intertidal zone at Advocate Beach. The inferred presence of a large and persistent trapped air component ($O(10\%)$ by pore volume) in the upper 0.5 m of the sediment column has important implications for beach stability and potential mechanisms for sediment mobilisation: Rapid attenuation attributed to the presence of pore-trapped air limits the effects of cyclic pressure loading by wave action to a region near the bed surface. However, the presence of large phase lags in the oscillatory pore pressure signal with sediment depth may lead to instances of momentary sediment liquefaction, wherein vertical pressure gradients associated with the passage of wave troughs periodically oppose the local gravity vector, with magnitudes sufficient to overcome the static gravitational equilibrium of the bed. Whether, or to what extent, momentary sediment liquefaction is important as a sediment mobilisation mechanism is not known.

In practice, due to the large and variable phase lags and high attenuation through the bed, attempts to obtain measurements of surface gravity wave kinematics using pressure sensors buried in intertidal sediments should include sediment-free passage between the sensors and the sediment-water interface (e.g., using rigid, perforated pipe). Phase coherent multi-sensor vertical arrays and poro-elastic bed response modelling are otherwise required. This may be true for a range of beach types, including pure sand (*Michallet et al.*, 2009), where sediments are intermittently aerated as a result of tidal action.

This thesis presents evidence of the morphodynamical importance of sedimentary feedbacks in the swash zone, leading to spatially correlated morpho-sedimentary features which may be highly organised (e.g., cusps) or irregular (textural 'patchiness' described in Chapter 6), but which have observable signatures that persist regardless of the forcing conditions. The feedbacks manifest most strikingly through the persistent coevolution of morphology and grain size in space. However, multiple other findings support the role of feedbacks as a causative mechanism: (1) the apparent influence of the surface grain size distribution on the timing (i.e., cross-shore position) and/or timescale of beach cusp emergence; (2) the presence of relict cusp horns on the positioning of emergent cusps in

the longshore; (3) the apparent lead time of the mean grain size maximum associated with the shoreward edge of the swash zone, relative to positive bed level change as a precursor to berm formation (see Chapter 7, Figs. 7.3 and 7.4); and (4) the substrate-dependent transport characteristics of individual cobbles in the swash zone.

The spatial correlations observed between changes in bed level and grain size are a result of processes in the swash zone during ebb tide. The ebb tide swash processes necessarily act over short timescales governed by the swash zone width and the rate of change of the mean shoreline position. The forcing associated with the passage of the shorebreak, surf zone, and flood tide swash zone leads to prolonged periods of sediment redistribution, resulting in spatial 'smoothing' of relict morphological and sedimentary features in the intertidal zone, at least when observed with a sampling resolution of once per tide. The lack of significant temporal correlations between bed level and grain size (from one tide to the next) may only indicate that the sampling interval was not sufficiently short to resolve time-coherent processes that occur over timescales which are commensurate with the forcing (O(10) s), or with the evolution of the morpho-sedimentary features (O(100-1000) s).

The emphasis in this thesis on correlating with subaerial observations means that it is much more difficult to observe signatures of feedbacks occurring either in the flood tide swash or seaward of the swash zone. However, the persistent spatial correlations between bed level and grain size that are associated with ebb tide swash processes give a strong indication that sedimentary feedbacks are morphodynamically important in the swash zone. Processes associated with the shorebreak and surf zone may still exhibit characteristics of morpho-sedimentary correlation, as in the cases of, for example, the beach step (*Austin and Buscombe*, 2008), and wave orbital-scale ripples (*Hay et al.*, 2014), though the mechanisms responsible for the formation of these features may not depend on a wide surficial grain size distribution.

The role of sedimentary feedbacks on longer-term beach morphological responses (i.e., longer than a single tide) is unclear. However, swash-generated morpho-sedimentary features of the beach profile have been shown in some cases to influence the longer-term response, as demonstrated in Chapter 5, under fairweather forcing, via the influence of relict cusps on the positioning of emergent cusp fields; as well as by *Orford and Carter* (1984), who reported that the locations of barrier overwash fans on a pure gravel beach during

storm events were influenced by the locations of relict cusps on the upper beach. Given the inference from Advocate Beach that the surf and swash zones can be approximated as a closed sedimentary unit (Chapter 6, based on anecdotal evidence from *Hay et al.*, 2014), it might be expected that coarse surficial sediments, in addition to one or more active or relict berms, would influence the response of the beach profile (e.g., the slope) to storm waves through the increased proportion of coarse particles. However, observations in support of this are not available from the current study.

Some insight into the nature of the morpho-sedimentary feedbacks is also evident from the results of this thesis: namely, that pattern formation and coherent morpho-sedimentary change are heavily influenced by the coarse tail of the grain size distribution on the beach surface, or at least that the presence of a wide surficial grain size distribution, containing both fine and coarse material, is most likely to lead to observable correlations, and to the formation of cusps and cusp-like features. In the correlation analysis of Chapter 6 (Table 6.4), an increase in the mean surficial grain size occurred during 86% of the observed instances of positive bed level change (where bed level increased by greater than two centimetres) in the mid-intertidal zone. Bed fining corresponded to negative bed level change in only 56% of cases. Similarly, in Chapter 5, the presence of coarse material at the beach surface accelerated (or, potentially, made possible) the emergence of beach cusps, as outlined above.

The apparent dynamical importance of the coarse tail of the grain size distribution is in contrast to results from the sand beach literature, at least for the case of beach cusps, where variations in grain size associated with morphological pattern formation have been suggested not to be mechanistically important in the formation process (*van Gaalen et al.*, 2011). With regard to the coevolution of bed level and grain size on MSG beaches, it seems likely that conditions of fractional transport, wherein the coarsest component of the grain size distribution experiences a diameter-dependent likelihood of mobilisation, or no mobilisation at all, is important, as opposed to conditions of equal mobility, under which particles experience equivalent probabilities of mobilisation regardless of particle diameter. In other words, it is likely important that the threshold mobilisation shear stress for the coarsest grains is of the same order of magnitude as the bed shear stress under swash forcing.

The presence of persistently observed correlations between bed level and grain size is

supportive of the 'intermediate case' of the morpho-sedimentary dynamics hypothesis, as described by *Buscombe and Masselink* (2006). In relation to the limiting cases, i.e., (1) that changes in grain size in dynamic sedimentary environments do not remain correlated through time or (2) that there does exist a temporal correlation or 'persistence' in sedimentary data, *Buscombe and Masselink* describe the intermediate case as morphological change resulting in spatial variability in grain size displaying temporal persistence, but with variations which are stochastic, centred around a time-averaged grain size distribution. The intermediate case allows grain size characteristics to have a role in the morphodynamic response of the beach.

MSG beaches are well-suited to morpho-sedimentary dynamical studies, their high degrees of grain size variability leading to relatively strong and observable sedimentary signals. Though morpho-sedimentary feedbacks undoubtedly influence the dynamics of pure gravel beaches as well, the narrower grain size distributions – paired with the inherent variability of grain size estimates based on digital imaging methods – may make it more difficult to observe sedimentary signals (see *Austin and Buscombe*, 2008; *Masselink et al.*, 2007). Even on MSG beaches, constant redistribution of sediments by surf and swash action leads to the loss of time-coherent signals if the observation frequency is too low, i.e., much lower than the frequency of the forcing. Improvements in analysis strategies, particularly ones leading to the ability to more fully characterise broad and variable grain size distributions, may make observing meaningful morpho-sedimentary signals possible for a wider range of beach types in the future.

8.3 Future Work

Despite substantial advances in observation techniques and the predictive skill and capacity of beach profile response models over the past several decades – particularly when applied to pure sand or gravel beaches – significant barriers to the predictability of physical beach processes remain. State of the art modelling efforts are not yet capable of reproducing mixed sand-gravel transport dynamics in the surf and swash zones. The confounding influences of inter-granular interactions, e.g., grain interlocking and sheltering by neighbouring grains leading to complex mobilisation characteristics, and the effects of spatial and temporal heterogeneity of grain size distributions on in/exfiltration and groundwater dynamics, in addition to near-bed turbulence from wave breaking and grain-scale roughness are difficult

to parameterise, and represent substantial barriers to first principles-type modelling of mixed sand-gravel transport in swash flows. More field and laboratory data are required, for a broader range of beach types and forcing conditions, to guide our understanding of the fundamental phenomenological responses of mixed sand-gravel sediments at the shoreline. Based on the results of this thesis, there are several avenues for future research that would be of interest.

A logical and timely starting point would be the undertaking of a review of MSG beach dynamics, in order to supplement the informative MSG beach review papers by *Kirk* (1980), *Mason and Coates* (2001), and *Pontee et al.* (2004), as well as the gravel beach review paper by *Buscombe and Masselink* (2006), with the advances of the past 15-20 years, particularly regarding remote sensing methods.

With regard to pore pressure and the hydraulic and groundwater responses of mixed sand-gravel beach sediments, it seems likely that the $O(10\%)$ trapped air component by pore volume inferred through the application of the *Yamamoto et al.* (1978) poro-elastic bed response model should influence percolation processes and sediment stability at Advocate Beach. Though it is not possible to directly observe the bulk air content in the bed, it would be of interest to validate the $O(10\%)$ air content estimate through the use of arrays of soil moisture sensors, which have been used elsewhere (e.g., *Heiss et al.*, 2015) to infer volumes of pore-trapped air through gravimetric or volumetric water content. Multi-element coherent arrays of soil moisture and pressure sensors, buried at multiple locations both across-shore and vertically, could be used to better characterise spatial and temporal variability in the bulk compressibility of the sediment-fluid medium, and its influence on bed stability via mass mobilisation events. Multiple (vertical) observations of pressure and air content would enable the testing of a threshold criterion for momentary sediment liquefaction (e.g., *Qi and Gao*, 2015), helping to assess the relative importance of sediment mobilisation mechanisms under oscillatory or impulsive wave loading.

The finding that the mean beach surface grain size is closely correlated with the forcing, the wave height and steepness in particular (the mean grain size decreasing roughly 13 mm per metre of increased significant wave height at Advocate Beach, at least for mean grain sizes ranging from 15-25 mm), warrants testing with longer time series, and in a broader range of MSG settings. The analysis by *Prodger et al.* (2016), which made use of time histories of disequilibrium wave steepness, led to the prediction of mean surface

grain sizes at a number of sand beach sites with considerable skill. It seems likely that a similar – though perhaps fundamentally opposite – relationship could be established for MSG beaches.

This thesis provides compelling evidence that mixed sand-gravel morphodynamics and grain size dynamics are intrinsically linked through feedback processes, with implications for beach morphological evolution, at least under swash forcing. In considering future work, it would be of interest to make similar measurements with greater spatial coverage, particularly in the cross-shore, in order to better resolve the fine-scale grain size and bed level changes associated with incipient berm formation at the leading edge of the swash, as well as other processes related to the response of the beach profile. This study has demonstrated that low cost commercial range sensors are capable of identifying swash-timescale changes in bed level, at least in a coarse-grained setting. More precise instrumentation would reduce the need for added processing, and would be required where a greater proportion of the grain size distribution is less than *ca*. 1 mm. More sensors in an across-shore configuration would also allow for the consideration of volume change in the swash region; e.g., is positive bed level change at the berm balanced by erosion from the mid-swash, or must material be sourced from the step region as well?

The lack of observations of other components of the grain size distribution (of comparable quality to the mean grain size), namely, a sorting parameter or other indication of the range of particle sizes present at a given time, represents a substantial shortcoming of the sedimentary datasets in this thesis. Given the acknowledged influence of the full grain size distribution on mixed sediment transport dynamics (e.g., the increased mobility of gravel-sized particles in the presence of a large sand fraction; *Wilcock et al.*, 2001), quantifying higher order moments of the grain size distribution would be of interest. Other properties of the grain size distribution, namely particle shape, have also been demonstrated to play an important role in particle transport dynamics. The ability to digitally quantify particle shape at wave forcing timescales would be valuable, particularly in the context of coarse particle transport in swash flows. However, this problem remains to be solved.

Based on the findings in this thesis, future field studies attempting to observe signals of morphological and sedimentary coevolution should give close consideration to the site. In comparison to pure gravel beaches, the space- and time-varying surficial grain size distributions found on MSG beaches appear well-suited to the emergence of detectable

signals. The presence of a large tide range is also beneficial, at least in terms of improved access to the intertidal zone, and likely also in terms of the improved signal-to-noise ratio resulting from decreased forcing duration per unit width of the beach. It would be of interest to conduct field studies similar to those outlined in Chapters 6 and 7 at mixed sand-gravel settings under a range of different tidal regimes. The presence of a large tide range is also useful for comprehending the phenomenological response of the beach: clear 'before' and 'after' bed states are separated by shorter timescales, especially near the high water line. Tide-to-tide changes in the morphology and sedimentary patterning of the bed in response to changes in forcing are therefore easier to observe – often strikingly so.

APPENDIX A

APPROXIMATE SOLUTION TO THE *Yamamoto et al.* (1978) PRESSURE EQUATION

Additional relations among the parameters in the Yamamoto et al. model are:

$$\omega' = a\omega, \tag{A.1}$$

$$a = \frac{\gamma}{k_c}\left[n\beta' + \frac{1-2\nu}{2(1-\nu)G}\right], \tag{A.2}$$

$$\omega'' = \kappa(\omega'/\tilde{k}^2), \tag{A.3}$$

$$\kappa = (1-\nu)/(1-2\nu), \tag{A.4}$$

$$\tilde{k}'' = (\tilde{k}' - \tilde{k})/\tilde{k}. \tag{A.5}$$

Equation (4.6) can be rewritten as

$$\tilde{k}' = \tilde{k}\left\{1 + \frac{i\omega a}{\tilde{k}^2}\right\}^{1/2}, \tag{A.6}$$

with $a \simeq 2.9$ using parameter values within our best-fit regime: $\gamma \simeq 10^4$ kg m^{-2} s^{-2}, $k_c = 7.6 \times 10^{-4}$ m s^{-1}, $n = 0.22$, $\beta' \simeq 10^{-6}$, $\nu = 0.33$, and $G = 4 \times 10^8$ Pa. The coefficient of i in (A.6), with $\omega/\tilde{k} = c = (gh)^{1/2} \simeq 3$ m s^{-1} the phase speed of 0.1 Hz

waves in $\approx$ 1 m water depth, is approximately 45. This value being much greater than 1, and the argument of $1 + i\omega a/\tilde{k}^2$ therefore being $\simeq \pi/2$, yield the approximation

$$\tilde{k}' \simeq (a\omega)^{1/2} \exp(i\pi/4). \tag{A.7}$$

Note that the $\pi/4$ value of the argument of $\tilde{k}'$ in equation (A.7) is consistent with the nearly equal real and imaginary parts from the full solution in Figure 4.1. Furthermore, since m $\simeq 200 >> 0$, the first term in equation (4.1) drops out and the solution obtained using the simplified p equation (4.7) applies, with $\tilde{k}'$ given by equation (A.7). This is essentially the Yamamoto et al. result for $G\beta' >> 0$. While the results from the full system equations are plotted in Figure 4.13, those from the approximate equations are visually indistinguishable from the full solution at this scale.

With the e-folding scale with sediment depth, $\tilde{k}'$, fixed by the observations (i.e. for fixed a and ω), we can differentiate β' in equation (A.2) with respect to k_c to obtain

$$\frac{d\beta'}{dk_c} = a/(\gamma n), \tag{A.8}$$

or, expanding β' = $\beta'(S)$, we have

$$\frac{dS}{dk_c} \simeq -Pa/(\gamma n) < 0, \tag{A.9}$$

since P, a, γ, and n are positive.

APPENDIX B

DIGITAL GRAIN SIZING VALIDATION

The *Buscombe* (2013) digital grain sizing (DGS) method used in Chapters 6 and 7 applies wavelet analysis to space-series transects of greyscale pixel intensities in the image(s) being processed. For the algorithm to function as intended, the images must contain only sediment, and individual grains must be resolvable by eye (i.e., have minimum grain diameters of 3-4 pixels). The output is a distribution of grain diameters characterised by information from the wavelet-derived power spectrum, i.e., using a statistical characterisation of each pixel transect, rather than characterisations of individual grains. Unlike earlier statistical methods, the *Buscombe* (2013) method does not require a site- or sediment population-specific calibration. The method is therefore described as 'transferable'. In comparison to earlier methods, the transferable wavelet method is more applicable to poorly sorted sediment populations.

The DGS method requires a suite of input parameters: (1) a density parameter, which determines the spacing between pixel rows in the input image to be processed; (2) a pixel to physical unit scale factor; (3) a filtering boolean, which applies a Savitzki-Golay high-pass 'flattening' filter if set to 'True'; (4) a 'notes' parameter, which defines the number of notes per octave to consider in the continuous wavelet transform; (5) an inverse pixel-to-frame-width ratio indicating the maximum diameter of grains to be resolved, in order to scale the maximum width of the 'mother' Morlet wavelet; and (6) a conversion constant required to enable comparability of the output with distributions obtained in a different dimensional space. See *Buscombe* (2013) or *Cuttler et al.* (2017) for more detailed summaries of the parameters. With the exception of the pixel to physical unit scaling parameter, the pixel-to-frame-width ratio, and the dimensional conversion constant,

the default parameter values were used in processing all images.

A validation analysis was carried out to ensure the most suitable parameter values were selected. Twenty-four surface sediment samples taken from the beach were transported to the laboratory, where grain size distributions were computed by sieving, a manual image-based point-counting approach, and the wavelet-based DGS method. The mean sample mass was 1.28 kg. The samples were prepared and sieved following the method of *Ingram* (1971) to obtain volume-by-weight grain size distributions. The point counting method is a standard validation technique for image-based grain sizing, in which an $n \times m$ uniformly spaced grid (9×9, in the case of this study) is overlaid on the image, and the widths of the grains beneath each grid vertex manually extracted to produce a grid-by-number type grain size distribution (e.g., *Barnard et al.*, 2007; *Buscombe et al.*, 2010).

To implement the point-counting and wavelet methods, each sample was placed in a tray and photographed using a tripod-mounted, downward-oriented Canon Powershot Elph 190, i.e., the same setup used for the survey photography in Chapter 6. 3-5 images were captured for each sample, with the sediments being redistributed between each photograph. Each photograph was cropped so only sediment was visible in the image. The cropped images were digitally flatted in the process of implementing the DGS algorithm.

Since the output of the DGS algorithm is a distribution of line-by-number grain diameters (see *Kellerhals and Bray* (1971); *Church et al.* (1987) for descriptions of the types particle size distributions), a conversion factor is needed in order for the DGS output to be comparable to (i.e., dimensionally consistent with) output from a sieve-type analysis. A commonly used conversion formula is (e.g. *Kellerhals and Bray*, 1971; *Diplas and Sutherland*, 1988; *Cuttler et al.*, 2017):

$$p_{2,i} = \frac{p_{1,i} D_i^x}{\Sigma p_{1,i} D_i^x}, \tag{B.1}$$

where $p_{1,i}$ is the known proportion of the ith size fraction obtained using the input measure, $p_{2,i}$ is the proportion of the ith size fraction in units consistent with the desired output measure, D_i is the grain diameter of the ith size fraction, and the exponent x is a conversion constant whose value is empirically dependent upon the grain size distribution. Eq. (B.1) is based on the voidless cube model from *Kellerhals and Bray* (1971), which assumes a porosity of zero. The *Kellerhals and Bray* conversion is based on purely dimensional arguments, and does not depend upon an idealisation of the material. Thus, though

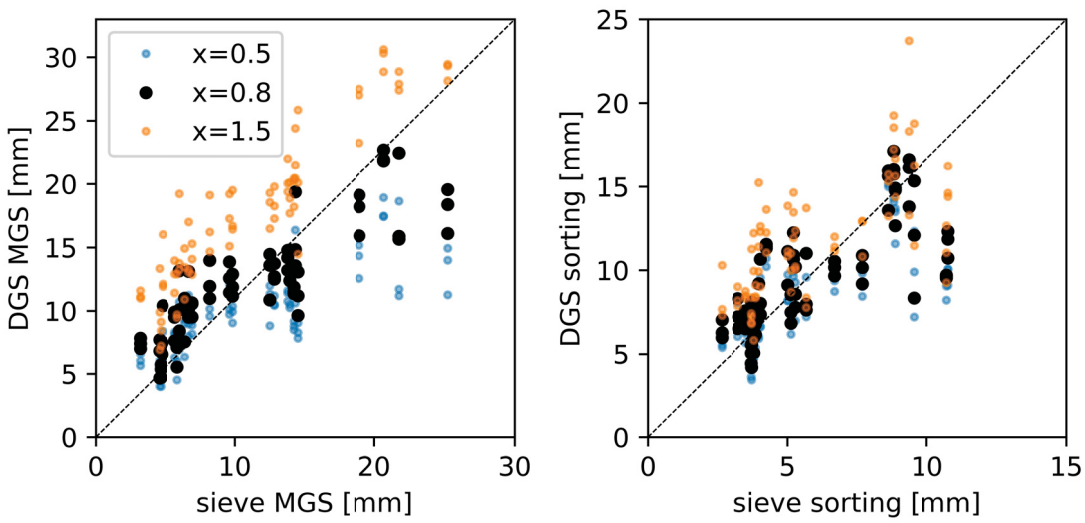

Figure B.1: Mean grain sizes (left) and sorting parameters (right) computed using the wavelet-based DGS method, plotted against values obtained from sieve analysis, for values of the dimensional scaling parameter x ranging from 0.5 to 1.5.

the parameter x can be theoretically defined based only on knowledge of the input and output measures, it is best employed as an empirically defined tuning parameter. For example, *Diplas and Sutherland* (1988) suggested a value of $x = -0.47$ for converting from an area-by-number to volume-by-number type sample using natural sediments with 33% porosity, though the voidless cube model would indicate a conversion constant of $x = -1$. Theoretically correct values of x for a given conversion can be found in Table 2 of *Kellerhals and Bray* (1971). The same exponent values can be deduced using dimensional arguments. For example, converting from a grid-by-number type measure $(O(D^0)/O(D^0))$ to a volume-by-number measure $(O(D^3)/O(D^0))$ requires a conversion factor of

$$\frac{O(D^0)/O(D^0)}{O(D^3)/O(D^0)} = O(D^{-3}). \tag{B.2}$$

For the output from the wavelet method to be theoretically comparable to output from the sieve analysis, a conversion factor of $O(D^1)$ is required. Note that the same conversion is used for comparing output from the wavelet method to output from the manual point counting method, since the sieve method (volume-by-weight) and the point counting method (grid-by-number) share an $O(D^0)$ equivalence.

For the validation analysis, x values in the range of 0.5 through 1.5 were tested. RMS

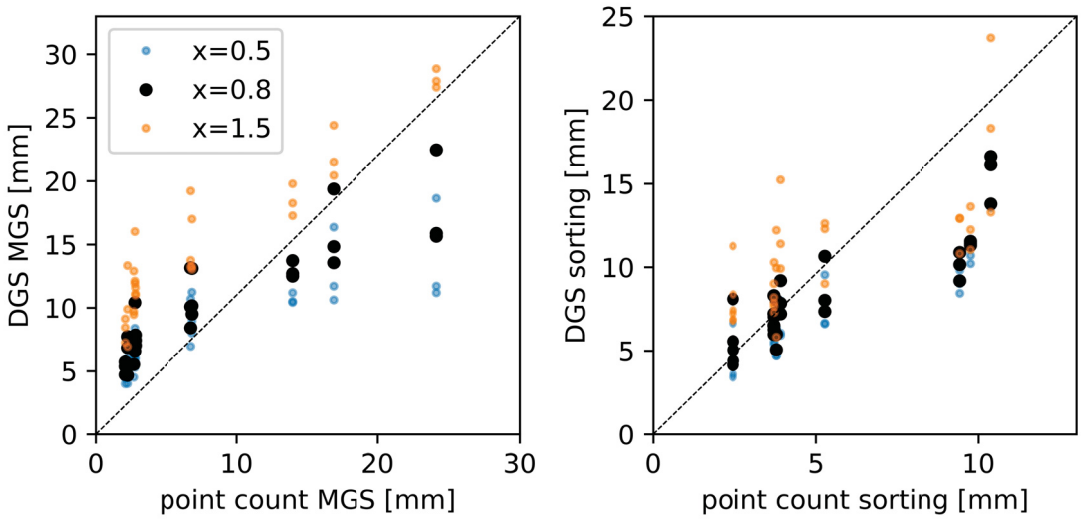

Figure B.2: Mean grain sizes (left) and sorting parameters (right) computed using the wavelet-based DGS method, plotted against values obtained using the manual point counting method, for values of the dimensional scaling parameter x ranging from 0.5 to 1.5.

Table B.1: Root mean square errors (RMSE) of the DGS and sieve-derived mean grain size data for the validation analysis.

x	DGS-sieve RMSE (mm)	DGS-point count RMSE (mm)
0.5	4.11	4.63
0.7	3.43	4.36
0.8	3.35	4.39
0.9	3.48	4.55
1.0	3.81	4.83
1.2	4.90	5.71
1.3	5.71	6.27
1.5	7.08	7.56

errors associated with all the x values tested are summarized in Table B.1, and results for a subset of the values are plotted in Figs. B.1 and B.2 for the sieve and point count method comparisons, respectively. The best result in a minimised root mean square error sense was obtained using $x = 0.8$ (RMSE=3.35 mm). Though the higher values for x arguably lead to a more linear (though positively offset) relationship (see $x = 1.5$ in Fig. B.1), this comes at the expense of the ability to differentiate grain sizes in the low- to mid range – i.e., the 10-20 mm mean grain size range – which accounts for a large proportion of the grain size distribution.

Other parameter values were held constant. The inverse pixel-to-frame-width ratio was set as 5.3, for a maximum resolved feature scale of 56 mm, given a cropped image frame with of 2453 pixels, and a pixel to metric scaling parameter value of 0.12. The inverse pixel-to-frame-width ratio of 5.3 was chosen so the maximum feature scale was consistent with the scale used to process the field survey images, which were cropped to different dimensions. Though this feature scale was not sufficient to resolve the largest grains in the distribution, it was deemed an acceptable compromise in the interest of optimising the representation of both the small and large diameter grains.

Though an acceptable level of agreement was obtained between the mean grain sizes computed using the DGS method and the validation methods, higher order moments of the grain size distribution, namely, the grain size sorting parameter (i.e., the standard deviation of the grain size distribution), the grain size skewness, and the kurtosis, were not reproduced with the same quality. This was attributed to the broad and variable grain size distribution within a given image, and throughout the image set. Consequently, the measures of grain size other than the mean were omitted from any analyses.

BIBLIOGRAPHY

Allan, J. C., R. Hart, and J. V. Tranquili, The use of Passive Integrated Transponder (PIT) tags to trace cobble transport in a mixed sand-and-gravel beach on the high-energy Oregon coast, USA, *Marine Geology*, *232*, 63–86, 2006.

Almar, R., G. Coco, K. R. Bryan, D. Huntley, A. Short, and N. Senechal, Video observations of beach cusp morphodynamics, *Marine Geology*, *254*, 216–223, 2008.

Almeida, L. P., G. Masselink, P. Russell, M. Davidson, R. McCall, and T. Poate, Swash zone morphodynamics of coarse-grained beaches during energetic wave conditions, *Coastal Engineering Proceedings*, *1*, 35, 2014.

Antia, E., Preliminary field observations on beach cusp formation and characteristics on tidally and morphodynamically distinct beaches on the Nigerian coast, *Marine Geology*, *78*, 23–33, 1987.

Austin, M. J., and D. Buscombe, Morphological change and sediment dynamics of the beach step on a macrotidal gravel beach, *Marine Geology*, *249*, 167–183, 2008.

Austin, M. J., and G. Masselink, Observations of morphological change and sediment transport on a steep gravel beach, *Marine Geology*, *229*, 59–77, 2006.

Baird, A. J., T. E. Mason, D. P. Horn, and T. E. Baldock, Monitoring and modelling ground water behaviour in sandy beaches as a basis for improved models of swash zone sediment transport, in *Coastal Dynamics-Proceedings of the International Conference*, pp. 774–783, ASCE, 1997.

Barnard, P. L., D. M. Rubin, J. Harney, and N. Mustain, Field test comparison of an autocorrelation technique for determining grain size using a digital beachball camera versus traditional methods, *Sedimentary Geology*, *201*, 180–195, 2007.

Bascom, W. N., The relationship between sand size and beach-face slope, *Eos, Transactions American Geophysical Union*, *32*, 866–874, 1951.

Bertoni, D., G. Sarti, G. Benelli, A. Pozzebon, and G. Raguseo, Transport trajectories of "smart" pebbles on an artificial coarse-grained beach at Marina di Pisa (Italy): Implications for beach morphodynamics, *Marine Geology*, *291*, 227–235, 2012.

Biot, M. A., General theory of three dimensional consolidation, *Journal of Applied Physics*, *12*, 155–164, 1941.

Blenkinsopp, C., I. Turner, G. Masselink, and P. Russell, Swash zone sediment fluxes: Field observations, *Coastal Engineering*, *58*, 28–44, 2011.

Bonjean, D., P. Foray, I. Piedra-Cueva, H. Michallet, P. Breul, Y. Haddani, M. Mory, and S. Abadie, Monitoring of the foundations of a coastal structure submitted to breaking waves: Occurrence of momentary liquefaction, *Proceedings, 14th ISOPE Conference*, *2*, 585–592, Toulon, France, 2004.

Bourgault, D., Shore-based photogrammetry of river ice, *Canadian Journal of Civil Engineering*, *35*, 80–86, 2008.

Bramato, S., M. Ortega-Sánchez, C. Mans, and M. A. Losada, Natural recovery of a mixed sand and gravel beach after a sequence of a short duration storm and moderate sea states, *Journal of Coastal Research*, *28*, 89–101, 2012.

Breul, P., and R. Gourvès, On site characterization and air content evaluation of coastal soils by image analysis to estimate liquefaction risk, *Canadian Geotechnical Journal*, *45*, 1723–1732, 2008.

Buscombe, D., Transferable wavelet method for grain-size distribution from images of sediment surfaces and thin sections, and other natural granular patterns, *Sedimentology*, *60*, 1709–1732, 2013.

Buscombe, D., and D. Conley, Effective shear stress of graded sediments, *Water Resources Research*, *48*, 2012.

Buscombe, D., and G. Masselink, Concepts in gravel beach dynamics, *Earth-Science Reviews*, *79*, 33–52, 2006.

Buscombe, D., D. Rubin, and J. Warrick, A universal approximation of grain size from images of noncohesive sediment, *Journal of Geophysical Research: Earth Surface*, *115*, 2010.

Carr, A. P., *13 Shingle beaches: aspects of their structure and stability*, pp. 97–104, Thomas Telford Publishing, 1983.

Carter, R., and J. Orford, Coarse clastic barrier beaches: A discussion of the distinctive dynamic and morphosedimentary characteristics, *Marine Geology*, *60*, 377 – 389, 1984, hydrodynamics and Sedimentation in Wave-Dominated Coastal Environments.

Carter, R., and J. Orford, The morphodynamics of coarse clastic beaches and barriers: A short-and long-term perspective, *Journal of Coastal Research*, *126*, 158–179, 1993.

Chang, F.-J., and C.-H. Chung, Estimation of riverbed grain-size distribution using image-processing techniques, *Journal of Hydrology*, *440*, 102–112, 2012.

Church, M. A., D. McLean, and J. Wolcott, River bed gravels: Sampling and analysis, Sediment Transport in Gravel-Bed Rivers, CR Thorne, JC Bathurst, RD Hey, eds., 43–88, 1987.

Ciavola, P., and E. Castiglione, Sediment dynamics of mixed sand and gravel beaches at short time-scales, *Journal of Coastal Research*, pp. 1751–1755, 2009.

Ciriano, Y., G. Coco, K. R. Bryan, and S. Elgar, Field observations of swash zone infragravity motions and beach cusp evolution, *Journal of Geophysical Research: Oceans*, *110*, 1–10, 2005.

Coco, G., and A. B. Murray, Patterns in the sand: From forcing templates to self-organization, *Geomorphology*, *91*, 271–290, 2007.

Coco, G., T. O'Hare, and D. Huntley, Beach cusps: A comparison of data and theories for their formation, *Journal of Coastal Research*, *15*, 741–749, 1999.

Coco, G., D. Huntley, and T. O'Hare, Investigation of a self-organization model for beach cusp formation and development, *Journal of Geophysical Research: Oceans*, *105*, 21991–22002, 2000.

Coco, G., T. K. Burnet, B. T. Werner, and S. Elgar, The role of tides in beach cusp development, *Journal of Geophysical Research: Oceans*, *109*, 1–12, 2004.

Craig, R. F., *Soil Mechanics*, Van Nostrand Reinhold, Wokingham, Berkshire, England, 1974.

Curtiss, G. M., P. D. Osborne, and A. R. Horner-Devine, Seasonal patterns of coarse sediment transport on a mixed sand and gravel beach due to vessel wakes, wind waves, and tidal currents, *Marine Geology*, *259*, 73–85, 2009.

Cuttler, M. V., R. J. Lowe, J. L. Falter, and D. Buscombe, Estimating the settling velocity of bioclastic sediment using common grain-size analysis techniques, *Sedimentology*, *64*, 987–1004, 2017.

Davidson, M. A., P. A. Bird, G. N. Bullock, and D. A. Huntley, Wave reflection: field measurements, analysis and theoretical developments, in *Coastal Dynamics '94*, pp. 642–655, ASCE, 1994.

Dean, R. G., Equilibrium beach profiles: characteristics and applications, *Journal of Coastal Research*, pp. 53–84, 1991.

Dean, R. G., and R. A. Dalrymple, *Water Wave Mechanics for Engineers and Scientists*, vol. 1, Prentice-Hall International, Inc., London, 1984.

Dickson, M. E., P. S. Kench, and M. S. Kantor, Longshore transport of cobbles on a mixed sand and gravel beach, southern Hawke Bay, New Zealand, *Marine Geology*, *287*, 31–42, 2011.

Diplas, P., and A. J. Sutherland, Sampling techniques for gravel sized sediments, *Journal of Hydraulic Engineering*, *114*, 484–501, 1988.

Dodd, N., A. M. Stoker, D. Calvete, and A. Sriariyawat, On beach cusp formation, *Journal of Fluid Mechanics*, *597*, 145–169, 2008.

Duncan Jr, J. R., The effects of water table and tide cycle on swash-backwash sediment distribution and beach profile development, *Marine Geology*, *2*, 186–197, 1964.

Elgar, S., T. Herbers, and R. Guza, Reflection of ocean surface gravity waves from a natural beach, *Journal of Physical Oceanography*, *24*, 1503–1511, 1994.

Garnier, R., M. Ortega-Sánchez, M. A. Losada, A. Falqués, and N. Dodd, Beach cusps and inner surf zone processes: growth or destruction? A case study of Trafalgar Beach (Cádiz, Spain), *Scientia Marina*, *74*, 539–553, 2010.

Gomez, B., Temporal variations in bedload transport rates: the effect of progressive bed armouring, *Earth Surface Processes and Landforms*, *8*, 41–54, 1983.

Grottoli, E., D. Bertoni, P. Ciavola, and A. Pozzebon, Short term displacements of marked pebbles in the swash zone: Focus on particle shape and size, *Marine Geology*, *367*, 143–158, 2015.

Grottoli, E., D. Bertoni, and P. Ciavola, Short-and medium-term response to storms on three Mediterranean coarse-grained beaches, *Geomorphology*, *295*, 738–748, 2017.

Grottoli, E., D. Bertoni, A. Pozzebon, and P. Ciavola, Influence of particle shape on pebble transport in a mixed sand and gravel beach during low energy conditions: Implications for nourishment projects, *Ocean & Coastal Management*, *169*, 171–181, 2019.

Guest, T. B., and A. E. Hay, Vertical structure of pore pressure under surface gravity waves on a steep, megatidal, mixed sand-gravel-cobble beach, *Journal of Geophysical Research: Oceans*, *122*, 153–170, 2017.

Guest, T. B., and A. E. Hay, Timescales of beach cusp evolution on a steep, megatidal, mixed sand-gravel beach, *Marine Geology*, *416*, 105984, 2019.

Guza, R. T., and A. J. Bowen, On the amplitude of beach cusps, *Journal of Geophysical Research*, *86*, 4125–4132, 1981.

Guza, R. T., and D. L. Inman, Edge waves and beach cusps, *Journal of Geophysical Research*, *80*, 2997–3012, 1975.

Hay, A. E., L. Zedel, and N. Stark, Sediment dynamics on a steep, megatidal, mixed sand-gravel-cobble beach, *Earth Surface Dynamics*, *2*, 117–152, 2014.

Heiss, J. W., J. A. Puleo, W. J. Ullman, and H. A. Michael, Coupled surface-subsurface hydrologic measurements reveal infiltration, recharge, and discharge dynamics across the swash zone of a sandy beach, *Water Resources Research*, *51*, 8834–8853, 2015.

Holland, K., and R. Holman, Field observations of beach cusps and swash motions, *Marine Geology*, *134*, 77–93, 1996.

Holland, K. T., Beach cusp formation and spacings at Duck, USA, *Continental Shelf Research*, *18*, 1081–1098, 1998.

Holland, K. T., R. A. Holman, T. C. Lippmann, J. Stanley, and N. Plant, Practical use of video imagery in nearshore oceanographic field studies, *IEEE Journal of Oceanic Engineering*, *22*, 81–92, 1997.

Holman, R., and A. Bowen, Bars, bumps, and holes: models for the generation of complex beach topography, *Journal of Geophysical Research: Oceans*, *87*, 457–468, 1982.

Holman, R. A., and J. Stanley, The history and technical capabilities of Argus, *Coastal Engineering*, *54*, 477–491, 2007.

Horn, D. P., Measurements and modelling of beach groundwater flow in the swash-zone: a review, *Continental Shelf Research*, *26*, 622–652, 2006.

Horn, D. P., and S. M. Walton, Sediment-level oscillations in the swash zone of a mixed sand and gravel beach, in *Proceedings, 29th International Conference on Coastal Engineering*, vol. 3, pp. 2390–2402, World Scientific Publishing Co, New Jersey. ASCE, 2004.

Horn, D. P., T. E. Baldock, A. J. Baird, and T. E. Mason, Field measurements of swash induced pressures within a sandy beach, *Journal of Coastal Engineering*, pp. 2812–2825, 1998.

Huntley, D. A., R. T. Guza, and E. B. Thornton, Field observations of surf beat 1. Progressive edge waves, *Journal of Geophysical Research*, *86*, 6451–6466, 1981.

Ingram, R. L., Sieve Analysis. In R. E. Carver (Ed.), *Procedures in Sedimentary Petrology*, Wiley Interscience, New York, pp. 49–67, 1971.

Isla, F. I., Overpassing and armouring phenomena on gravel beaches, *Marine Geology*, *110*, 369–376, 1993.

Ivamy, M. C., and P. S. Kench, Hydrodynamics and morphological adjustment of a mixed sand and gravel beach, Torere, Bay of Plenty, New Zealand, *Marine Geology*, *228*, 137–152, 2006.

Jeng, D. S., Wave-induced sea floor dynamics, *Applied Mechanics Reviews*, *56*, 407–429, 2003.

Jennings, R., and J. Shulmeister, A field based classification scheme for gravel beaches, *Marine Geology*, *186*, 211–228, 2002.

Kellerhals, R., and D. I. Bray, Sampling procedures for coarse fluvial sediments, *Journal of the Hydraulics Division*, *97*, 1165–1180, 1971.

Kirk, R., Aspects of surf and runup processes on mixed sand and gravel beaches, *Geografiska Annaler: Series A, Physical Geography*, *57*, 117–133, 1975.

Kirk, R., Mixed sand and gravel beaches: morphology, processes and sediments, *Progress in Physical Geography*, *4*, 189–210, 1980.

Komar, P. D., Observations of beach cusps at Mono Lake, California, *Geological Society of America Bulletin*, *84*, 3593–3600, 1973.

Kulkarni, C. D., F. Levoy, O. Monfort, and J. Miles, Morphological variations of a mixed sediment beachface (Teignmouth, UK), *Continental Shelf Research*, *24*, 1203–1218, 2004.

Lanckriet, T., J. A. Puleo, G. Masselink, I. L. Turner, D. Conley, C. Blenkinsopp, and P. Russell, Comprehensive field study of swash-zone processes. ii: Sheet flow sediment concentrations during quasi-steady backwash, *Journal of Waterway, Port, Coastal, and Ocean Engineering*, *140*, 29–42, 2013.

Leighton, T. G., *The Acoustic Bubble*, Academic Press, San Diego, California, 1994.

Levoy, F., E. J. Anthony, O. Monfort, and C. Larsonneur, The morphodynamics of megatidal beaches in Normandy, France, *Marine Geology*, *171*, 39–59, 2000.

Longuet-Higgins, M., and D. Parkin, Sea waves and beach cusps, *The Geographical Journal*, *128*, 194–201, 1962.

López de San Román-Blanco, B., T. T. Coates, P. Holmes, A. J. Chadwick, A. Bradbury, T. E. Baldock, A. Pedrozo-Acuña, J. Lawrence, and J. Grüne, Large scale experiments on gravel and mixed beaches: Experimental procedure, data documentation and initial results, *Journal of Coastal Engineering*, *53*, 349–362, 2006.

Lorenz, E. N., Deterministic nonperiodic flow, *Journal of the Atmospheric Sciences*, *20*, 130–141, 1963.

Madsen, O. S., Wave-induced pore pressures and effective stresses in a porous bed, *Geotechnique*, *28*, 377–393, 1978.

Mason, T., and T. T. Coates, Sediment transport processes on mixed beaches: a review for shoreline management, *Journal of Coastal Research*, *17*, 645–657, 2001.

Massel, S. R., Gravity waves propagated over permeable bottom, *Journal of the Waterways, Harbors, and Coastal Engineering Division, ASCE*, *102*, 111–121, 1976.

Masselink, G., and L. Li, The role of swash infiltration in determining the beachface gradient: a numerical study, *Marine Geology*, *176*, 139–156, 2001.

Masselink, G., and J. A. Puleo, Swash-zone morphodynamics, *Continental Shelf Research*, *26*, 661–680, 2006.

Masselink, G., B. J. Hegge, and C. B. Pattiaratchi, Beach cusp morphodynamics, *Earth Surface Processes and Landforms*, *22*, 1139–1155, 1997.

Masselink, G., N. Auger, P. Russell, and T. O'Hare, Short-term morphological change and sediment dynamics in the intertidal zone of a macrotidal beach, *Sedimentology*, *54*, 39–53, 2007.

Masselink, G., P. Russell, I. Turner, and C. Blenkinsopp, Net sediment transport and morphological change in the swash zone of a high-energy sandy beach from swash event to tidal cycle time scales, *Marine Geology*, *267*, 18–35, 2009.

Matthews, E. R., Measurements of beach pebble attrition in Palliser Bay, southern North Island, New Zealand, *Sedimentology*, *30*, 787–799, 1983.

McLean, R. F., Variations in grain-size and sorting on two Kaikoura beaches, *New Zealand Journal of Marine and Freshwater Research*, *4*, 141–164, 1970.

Mei, C. C., and M. A. Foda, Wave-induced responses in a fluid-filled poro-elastic solid with a free surface – a boundary layer theory, *Geophysical Journal of the Royal Astronomical Society*, *66*, 597–631, 1981.

Michallet, H., M. Mory, and I. Piedra-Cueva, Wave-induced pore pressure measurements near a coastal structure, *Journal of Geophysical Research: Oceans*, *114*, 2009.

Miche, M., Le pouvoir réfléchissant des ouvrages maritimes exposés à l'action de la houle, *Annales de Ponts et Chaussées, 121*, pp. 285–319, 1951.

Miller, I. M., and J. A. Warrick, Measuring sediment transport and bed disturbance with tracers on a mixed beach, *Marine Geology*, *299*, 1–17, 2012.

Miller, I. M., J. A. Warrick, and C. Morgan, Observations of coarse sediment movements on the mixed beach of the Elwha Delta, Washington, *Marine Geology*, *282*, 201–214, 2011.

Mory, M., H. Michallet, D. Bonjean, I. Piedra-Cueva, J. M. Barnoud, P. Foray, S. Abadie, and P. Breul, A field study of momentary liquefaction caused by waves around a coastal structure, *Journal of Waterway, Port, Coastal, and Ocean Engineering*, *133*, 28–38, 2007.

Moss, A., The physical nature of common sandy and pebbly deposits, part I, *American Journal of Science*, *260*, 337–373, 1962.

Murray, A. B., and E. R. Thieler, A new hypothesis and exploratory model for the formation of large-scale inner-shelf sediment sorting and "rippled scour depressions", *Continental Shelf Research*, *24*, 295–315, 2004.

Nielsen, P., *Coastal bottom boundary layers and sediment transport*, vol. 4, World Scientific Publishing Company, 1992.

Nolan, T., R. Kirk, and J. Shulmeister, Beach cusp morphology on sand and mixed sand and gravel beaches, South Island, New Zealand, *Marine Geology*, *157*, 185–198, 1999.

Nordstrom, K. F., and N. L. Jackson, Distribution of surface pebbles with changes in wave energy on a sandy estuarine beach, *Journal of Sedimentary Research*, *63*, 1152–1159, 1993.

Okusa, S., Wave-induced stresses in unsaturated marine sediments, *Geotechnique*, *35*, 517–532, 1985.

Oltman-Shay, J., and R. T. Guza, Infragravity edge wave observations on two California beaches, *Journal of Physical Oceanography*, *17*, 644–663, 1987.

Orford, J. D., and R. Carter, Mechanisms to account for the longshore spacing of overwash throats on a coarse clastic barrier in southeast Ireland, *Marine Geology*, *56*, 207–226, 1984.

Osborne, P. E., Transport of gravel and cobble on a mixed-sediment inner bank shoreline of a large inlet, Grays Harbor, Washington, *Marine Geology*, *224*, 145–156, 2005.

Packwood, A., The influence of beach porosity on wave uprush and backwash, *Coastal Engineering*, *7*, 29–40, 1983.

Pearre, N. S., and J. A. Puleo, Quantifying Seasonal Shoreline Variability at Rehoboth Beach, Delaware, Using Automated Imaging Techniques, *Journal of Coastal Research*, *2009*, 900 – 914, 2009.

Pedrozo-Acuña, A., D. J. Simmonds, A. J. Chadwick, and R. Silva, A numerical–empirical approach for evaluating morphodynamic processes on gravel and mixed sand–gravel beaches, *Marine Geology*, *241*, 1–18, 2007.

Pedrozo-Acuña, A., D. J. Simmonds, and D. E. Reeve, Wave-impact characteristics of plunging breakers acting on gravel beaches, *Marine Geology*, *253*, 26–35, 2008.

Phillips, J. D., Nonlinear dynamical systems in geomorphology: revolution or evolution?, *Geomorphology*, *5*, 219–229, 1992.

Plant, N. G., and R. A. Holman, Intertidal beach profile estimation using video images, *Marine Geology*, *140*, 1–24, 1997.

Plant, N. G., K. T. Holland, and J. A. Puleo, Analysis of the scale of errors in nearshore bathymetric data, *Marine Geology*, *191*, 71–86, 2002.

Poate, T., G. Masselink, R. McCall, P. Russell, and M. Davidson, Storm-driven cusp behaviour on a high energy gravel beach, *Journal of Coastal Research*, *70*, 645–650, 2014.

Pontee, N. I., K. Pye, and S. J. Blott, Morphodynamic behaviour and sedimentary variation of mixed sand and gravel beaches, Suffolk, UK, *Journal of Coastal Research*, pp. 256–276, 2004.

Prodger, S., P. Russell, M. Davidson, J. Miles, and T. Scott, Understanding and predicting the temporal variability of sediment grain size characteristics on high-energy beaches, *Marine Geology*, *376*, 109–117, 2016.

Puleo, J. A., C. Blenkinsopp, D. Conley, G. Masselink, I. L. Turner, P. Russell, D. Buscombe, D. Howe, T. Lanckriet, R. McCall, and T. Poate, Comprehensive field study of swash-zone processes. I: Experimental design with examples of hydrodynamic and sediment transport measurements, *Journal of Waterway, Port, Coastal, and Ocean Engineering*, *140*, 14–28, 2013.

Putnam, J. A., Loss of wave energy due to percolation in a permeable sea bottom, *Transactions American Geophysical Union*, *30*, 349–356, 1949.

Qi, W.-G., and F.-P. Gao, A modified criterion for wave-induced momentary liquefaction of sandy seabed, *Theoretical and Applied Mechanics Letters*, *5*, 20–23, 2015.

Raubenheimer, B., S. Elgar, and R. T. Guza, Estimating wave heights from pressure measured in sand bed, *Journal of Waterway, Port, Coastal, and Ocean Engineering*, *124*, 151–154, 1998.

Richards, C., D. Bourgault, P. S. Galbraith, A. Hay, and D. E. Kelley, Measurements of shoaling internal waves and turbulence in an estuary, *Journal of Geophysical Research: Oceans*, *118*, 273–286, 2013.

Roberts, T. M., P. Wang, and J. A. Puleo, Storm-driven cyclic beach morphodynamics of a mixed sand and gravel beach along the Mid-Atlantic Coast, USA, *Marine Geology*, *346*, 403–421, 2013.

Rubin, D. M., A simple autocorrelation algorithm for determining grain size from digital images of sediment, *Journal of Sedimentary Research*, *74*, 160–165, 2004.

Russell, P., G. Masselink, C. Blenkinsopp, and I. Turner, A comparison of berm accretion in the swash zone on sand and gravel beaches at the timescale of individual waves, *Journal of Coastal Research*, *SI 56*, 1791–1795, 2009.

Sakai, T., K. Hatanaka, and H. Mase, Wave-induced effective stress in seabed and its momentary liquefaction, *Journal of Waterway, Port, Coastal, and Ocean Engineering*, *118*, 202–206, 1992.

Sakai, T., H. Mase, D. T. Cox, and Y. Ueda, Field observation of wave-induced porewater pressures, *Proceedings of the 3rd International Offshore and Polar Engineering Conference*, pp. 667–673, 1993.

Sherman, D. J., J. D. Orford, and R. Carter, Development of cusp-related, gravel size and shape facies at Malin Head, Ireland, *Sedimentology*, *40*, 1139–1152, 1993.

Sleath, J. F. A., Wave-induced pressures in beds of sand, *Journal of the Hydraulics Division, ASCE*, *96*, 367–378, 1970.

Stark, N., and A. E. Hay, Pore water infiltration and drainage on a megatidal beach in relation to tide- and wave-forcing, *Coastal Engineering Proceedings*, *1*, sediment.25, 2014.

Stark, N., and A. E. Hay, Pebble and cobble transport on a steep, mega-tidal, mixed sand and gravel beach, *Marine Geology*, *382*, 210–223, 2016.

Stark, N., A. E. Hay, R. Cheel, and C. B. Lake, The impact of particle shape on the angle of internal friction and the implications for sediment dynamics at a steep, mixed sand–gravel beach, *Earth Surface Dynamics*, *2*, 469–480, 2014.

Sunamura, T., A predictive relationship for the spacing of beach cusps in nature, *Coastal Engineering*, *51*, 697–711, 2004.

Sunamura, T., and H. Aoki, Short communication a field experiment of cusp formation on a coarse clastic beach using a suspended video-camera system, *Earth Surface Processes and Landforms*, *25*, 329–333, 2000.

Taylor, R. B., S. L. Wittman, M. J. Milne, and S. M. Kober, Beach morphology and coastal changes at selected sites, mainland Nova Scotia, *Technical Report*, *85-12*, Geological Survey of Canada, Ottawa, 1985.

Turner, I. L., Simulating the influence of groundwater seepage on sediment transported by the sweep of the swash zone across macro-tidal beaches, *Marine Geology*, *125*, 153–174, 1995.

Turner, I. L., P. E. Russell, and T. Butt, Measurement of wave-by-wave bed-levels in the swash zone, *Coastal Engineering*, *55*, 1237–1242, 2008.

van Gaalen, J. F., S. E. Kruse, G. Coco, L. Collins, and T. Doering, Observations of beach cusp evolution at Melbourne Beach, Florida, USA, *Geomorphology*, *129*, 131–140, 2011.

van Genuchten, M. T., A closed-form equation for predicting the hydraulic conductivity of unsaturated soils, *Soil Science Society of America Journal*, *44*, 892–898, 1980.

Van Oyen, T., H. De Swart, and P. Blondeaux, Bottom topography and roughness variations as triggering mechanisms to the formation of sorted bedforms, *Geophysical Research Letters*, *37*, 2010.

Van Rijn, L. C., Sediment transport, part I: bed load transport, *Journal of Hydraulic Engineering*, *110*, 1431–1456, 1984.

Van Wellen, E., A. J. Chadwick, and T. Mason, A review and assessment of longshore sediment transport equations for coarse-grained beaches, *Coastal Engineering*, *40*, 243–275, 2000.

Vousdoukas, M. I., Erosion/accretion patterns and multiple beach cusp systems on a meso-tidal, steeply-sloping beach, *Geomorphology*, *141*, 34–46, 2012.

Vousdoukas, M. I., P. M. Ferreira, L. P. Almeida, G. Dodet, F. Psaros, U. Andriolo, R. Taborda, A. N. Silva, A. Ruano, and Ó. M. Ferreira, Performance of intertidal topography video monitoring of a meso-tidal reflective beach in South Portugal, *Ocean Dynamics*, *61*, 1521–1540, 2011.

Warrick, J. A., D. M. Rubin, P. Ruggiero, J. N. Harney, A. E. Draut, and D. Buscombe, Cobble cam: Grain-size measurements of sand to boulder from digital photographs and autocorrelation analyses, *Earth Surface Processes and Landforms: The Journal of the British Geomorphological Research Group*, *34*, 1811–1821, 2009.

Werner, B. T., and T. M. Fink, Beach cusps as self-organised patterns, *Science*, *260*, 968–971, 1993.

Wilcock, P. R., and J. C. Crowe, Surface-based transport model for mixed-size sediment, *Journal of Hydraulic Engineering*, *129*, 120–128, 2003.

Wilcock, P. R., and B. W. McArdell, Surface-based fractional transport rates: Mobilization thresholds and partial transport of a sand-gravel sediment, *Water Resources Research*, *29*, 1297–1312, 1993.

Wilcock, P. R., and B. W. McArdell, Partial transport of a sand/gravel sediment, *Water Resources Research*, *33*, 235–245, 1997.

Wilcock, P. R., S. T. Kenworthy, and J. C. Crowe, Experimental study of the transport of mixed sand and gravel, *Water Resources Research*, *37*, 3349–3358, 2001.

Wilson, G. W., A. E. Hay, and A. J. Bowen, Observations of wave shear stress on a steep beach, *Journal of Geophysical Research: Oceans*, *119*, 7827–7839, 2014.

Wright, L., and B. Thom, Coastal depositional landforms: a morphodynamic approach, *Progress in Physical Geography*, *1*, 412–459, 1977.

Wright, L., J. Chappell, B. Thom, M. Bradshaw, and P. Cowell, Morphodynamics of reflective and dissipative beach and inshore systems: Southeastern Australia, *Marine Geology*, *32*, 105–140, 1979.

Yamamoto, T., H. L. Koning, H. Sellmeijer, and E. V. Hijum, On the response of a poro-elastic bed to water waves, *Journal of Fluid Mechanics*, *87*, 193–206, 1978.